

**SIMULATING SCRAMJET BEHAVIOR: UNSTART PREDICTION IN A
SUPERSONIC, TURBULENT INLET-ISOLATOR DUCT FLOW**

by

Ian A. Hall

A Thesis

Submitted to the Faculty of Purdue University

In Partial Fulfillment of the Requirements for the degree of

Master of Science in Aeronautics and Astronautics



School of Aeronautics & Astronautics

West Lafayette, Indiana

May 2019

**THE PURDUE UNIVERSITY GRADUATE SCHOOL
STATEMENT OF COMMITTEE APPROVAL**

Dr. Jonathan Poggie, Chair

School of Aeronautics and Astronautics

Dr. Gregory Blaisdell

School of Aeronautics and Astronautics

Dr. Tom Shih

School of Aeronautics and Astronautics

Approved by:

Dr. Weinong Chen

Head of the Graduate Program

Dedicated to my family and to Hannah

ACKNOWLEDGMENTS

I would like to thank my advisor, Dr. Jonathan Poggie, for his constant support and guidance throughout my time in the graduate program at Purdue. The chance to work with him and be a member of his research group has been a great opportunity for growth and I will carry its lessons with me through the rest of my career. He has been a valuable mentor and advisor, from the time I was initially applying to Purdue up to today, providing support and insight that has made my time at Purdue both fruitful and fulfilling. Thanks are also due to Dr. Gregory Blaisdell and Dr. Tom Shih for being on my thesis committee. Their feedback provided valuable insight and this completed thesis wouldn't be the same without it.

My research colleagues have also provided significant support and I thank Akshay Deshpande, Tugba Piskin, and Geoffrey Andrews for their help and friendship as I worked through my Masters. Special thanks are due to Akshay for always being willing and ready to help and share his knowledge as an SU2 and Tecplot wizard. I would also like to thank Dr. Justin Wagner and Dr. Noel Clemens for allowing me to use several of their figures in this thesis. Their work provided the experimental grounding that I used to validate my computational results and, in my opinion, represents a seminal set of experiments and analysis into scramjet unstart.

This work was supported by the DoD SMART Scholarship program. In addition, computer time for this work was provided by Purdue University. This work was also supported in part by supercomputer hours provided by the AFRL DSRC.

TABLE OF CONTENTS

LIST OF FIGURES	7
ABBREVIATIONS	11
NOMENCLATURE	12
ABSTRACT.....	15
1. INTRODUCTION	16
1.1 Hypersonic Flight.....	16
1.2 Dual-Mode Scramjet.....	18
1.3 Unstart.....	20
1.4 Scope of Research.....	21
2. METHODOLOGY	23
2.1 Experimental Background	23
2.2 Code Configuration.....	26
2.3 Mesh Generation.....	28
2.3.1 2D Flat Plate Grids	29
2.3.2 2D Inlet-Isolator Grids.....	30
2.3.3 3D Inlet-Isolator Grids.....	33
2.3.4 Source Term Grids.....	35
2.4 Computation Scaling Study	36
2.5 Source Term.....	40
3. 2D COMPUTATION	44
3.1 Grid Convergence	44
3.2 Grid Independence Study.....	48
3.3 Boundary Layer Development.....	49
3.4 Fully Started Flow.....	51
3.5 Unstart.....	56
3.6 Unstart Precursors.....	60
4. 3D COMPUTATION	67
4.1 Boundary Layer Development.....	67
4.2 Grid Independence Study.....	68

4.3	Fully Started Flow.....	69
4.4	Unstart.....	73
4.5	Unstart Precursors.....	80
5.	PARAMETRIC STUDY	84
5.1	Thin Boundary Layer	84
5.1.1	2D Thin Boundary Layer Fully Started Flow	85
5.1.2	2D Thin Boundary Layer Unstart	88
5.1.3	2D Thin Boundary Layer Unstart Precursors	93
5.1.4	3D Thin Boundary Layer Fully Started Flow	95
5.1.5	3D Thin Boundary Layer Unstart	99
5.1.6	3D Thin Boundary Layer Unstart Precursors	103
5.2	Aspect Ratio Effects	107
5.2.1	Narrow Channel Fully Started Flow	107
5.2.2	Narrow Channel Unstart	110
5.2.3	Narrow Channel Unstart Precursors	114
6.	CONCLUSIONS	117
6.1	Results Summary	117
6.2	Suggestions for Future Work	119
	REFERENCES	120

LIST OF FIGURES

Fig. 1.1 Schematic, adapted from Anderson et al. [5] of A) Ramjet B) Scramjet	18
Fig. 1.2 Scramjet Schematic	19
Fig. 2.1 Inlet-Isolator Mounted in Wind Tunnel.....	24
Fig. 2.2 Inlet-Isolator Test Section (axes in m)	24
Fig. 2.3 2D Flat Plate Grid Boundary Conditions	30
Fig. 2.4 2D Flat Plate Grids A) Coarse, B) Medium, C) Fine	30
Fig. 2.5 Inlet-Isolator Expanded Mesh (axes in m)	31
Fig. 2.6 2D Inlet-Isolator Grids A) Coarse, B) Medium, C) Fine.....	32
Fig. 2.7 2D Inlet-Isolator Grid Boundary Conditions.....	32
Fig. 2.8 3D Inlet-Isolator Grid	33
Fig. 2.9 3D Inlet-Isolator Test Section Model in Green	34
Fig. 2.10 3D Flat Plate plus Inlet-Isolator Mesh.....	34
Fig. 2.11 3D Flat Plate plus Inlet-Isolator Mesh Boundary Conditions.	35
Fig. 2.12 Source Term Mesh A) 2D, B) 3D.....	36
Fig. 2.13 Flat Plate Mesh A) Speedup, B) Efficiency	37
Fig. 2.14 2D Inlet-Isolator Mesh A) Speedup B) Efficiency	38
Fig. 2.15 3D Inlet-Isolator Mesh A) Speedup, B) Efficiency.....	38
Fig. 2.16 Serial Fraction A) Flat Plate, B) 2D Inlet-Isolator, C) 3D Inlet-Isolator.....	39
Fig. 2.17 2D Source Term Flow Field Countours	42
Fig. 2.18 3D Source Term Flow Field Countours (Z, Y, X Center Planes)	43
Fig. 3.1 Convergence of Flat Plate C_f (Coarse, Medium, and Fine Grids).....	44
Fig. 3.2 Convergence of Flat Plate P (Coarse, Medium, and Fine Grids)	45
Fig. 3.3 Skin Friction Convergence Plots	45
Fig. 3.4 Computational Skin Friction Values vs Von Karman	46
Fig. 3.5 Skin Friction vs Van Driest	48
Fig. 3.6 Converged Flat Plate Solutions A) Coarse, B) Medium, C) Fine	50
Fig. 3.7 Flat Plate Streamwise Velocity Near Wall for 3 Grids, at $x = 2.2$ m	51
Fig. 3.8 2D Pseudo-Schlieren Image (Density Gradient Magnitude) of Fully Started Flow.....	52
Fig. 3.9 Schlieren Image of Fully Started Supersonic Flow, used with permission [19]	52

Fig. 3.10 Normalized Wall Pressure of 2D Fully Started Flow on Channel Floor.....	53
Fig. 3.11 Normalized Wall Pressure of 2D Fully Started Flow on Channel Ceiling.....	53
Fig. 3.12 Normalized 2D Fully Started Flow Pressure A) Coarse, B) Medium, C) Fine.....	54
Fig. 3.13 A) Experimental PIV, used with permission [20], B) 2D Velocity Field	55
Fig. 3.14 Velocity Field of 2D of Full Inlet-Isolator	55
Fig. 3.15 Unstart A) Schlieren Images used with permission [19], B) 2D Pseudo-Schlieren	56
Fig. 3.16 2D Unstart Pressure at $t = [0.25, 0.50, 0.75, \dots, 2.00]$ ms	57
Fig. 3.17 2D Unstart Pressure at $t = [2.25, 2.50, 2.75, 3.00]$ ms	58
Fig. 3.18 Unstart Speed through 2D Inlet-Isolator vs A) Position, B) Time	59
Fig. 3.19 Unstart Shock Arrival Time in 2D Inlet-Isolator.....	60
Fig. 3.20 2D Regions of Subsonic Flow during Unstart at $t = [0.5, 1.0, 1.5, \dots, 3.0]$ ms	60
Fig. 3.21 2D Wall Pressure during Unstart at $t = [0.0, 0.5, 1.0, \dots, 2.5]$ ms	61
Fig. 3.22 2D Unstart Peak Pressure A) Strength, B) Location	63
Fig. 3.23 2D Unstart Precursor Signal on Channel A) Bottom, B) Top.....	64
Fig. 3.24 2D Unstart Precursor Signal (all time) on Channel A) Bottom, B) Top	65
Fig. 4.1 3D Normalized Pressure Comparison A) Coarse, B) Medium, C) Fine	69
Fig. 4.2 Pseudo-Schlieren Image of Fully Started Flow A) 2D, B) 3D.....	70
Fig. 4.3 Pseudo-Schlieren Image of 3D Fully Started Flow Y Centerline	70
Fig. 4.4 Fully Started Flow Pressure A) 2D, B) 3D Z-Centerline, C) 3D Y-Centerline	71
Fig. 4.5 3D Velocity Field for Z Centerline (L) and Y Centerline (R).....	72
Fig. 4.6 Normalized Wall Pressure of 3D Fully Started Flow on Channel A) Floor, B) Ceiling. 73	
Fig. 4.7 Unstart A) Schlieren Images used with permission [19], B) 3D Pseudo-Schlieren	74
Fig. 4.8 3D Unstart Pressure at $t = [0.05, 0.10, 0.15, \dots, 0.5]$ ms	75
Fig. 4.9 Unstart Speed through 3D Inlet-Isolator vs A) Position, B) Time	77
Fig. 4.10 3D Unstart Shock Arrival Time.....	77
Fig. 4.11 3D Regions of Subsonic Flow during Unstart at $t = [0.1, 0.2, 0.3, \dots, 0.5]$ ms	78
Fig. 4.12 3D Corner Vortices.....	79
Fig. 4.13 3D Wall Pressure Traces during Unstart at $t = [0.0, 0.1, 0.2, \dots, 0.5]$ ms	80
Fig. 4.14 3D Unstart Peak Pressure A) Strength, B) Location	82
Fig. 4.15 3D Unstart Precursor Signal on Channel A) Bottom, B) Top.....	83
Fig. 4.16 3D Unstart Precursor Signal (all time) on Channel A) Bottom, B) Top	83

Fig. 5.1 Pseudo-Schlieren Image of 2D Fully Started Flow A) Thick BL, B) Thin BL.....	85
Fig. 5.2 2D Velocity Field A) Thick BL, B) Thin BL.....	86
Fig. 5.3 2D Fully Started Flow Pressure A) Thick BL, B) Thin BL	87
Fig. 5.4 2D Thin BL Fully Started Flow Wall Pressure on Channel A) Floor, B) Ceiling	87
Fig. 5.5 2D Thin BL Unstart at $t = [0.25, 0.5, 0.75, \dots, 3]$ ms	88
Fig. 5.6 2D Thin BL Unstart Speed vs A) Position, B) Time.....	89
Fig. 5.7 2D Thin BL Unstart Shock Arrival Time.....	90
Fig. 5.8 2D Thin BL Subsonic Flow Regions during Unstart at $t = [0.5, 1.0, 1.5, \dots, 3.0]$ ms....	90
Fig. 5.9 2D Thin BL Wall Pressure during Unstart	91
Fig. 5.10 2D Thin BL Wall Peak Pressure A) Strength, B) Location.....	93
Fig. 5.11 2D Thin BL Unstart Precursor Signal on Channel A) Bottom, B) Top	93
Fig. 5.12 2D Thin BL Unstart Precursor Signal (all time) on Channel A) Bottom, B) Top.....	94
Fig. 5.13 Pseudo-Schlieren Image along Z-Centerline A) 3D Thick BL, B) 3D Thin BL.....	95
Fig. 5.14 Pseudo-Schlieren Image Y-Centerline A) 3D Thick BL, B) 3D Thin BL	96
Fig. 5.15 Fully Started Flow Pressure A) 2D Thin BL, B) 3D Thick BL, C) 3D Thin BL	96
Fig. 5.16 Normalized Y-Plane Fully Started Flow Pressure A) 3D Thick BL, B) 3D Thin BL...	97
Fig. 5.17 3D Thin BL Fully Started Flow Wall Pressure on Channel A) Floor, B) Ceiling	98
Fig. 5.18 3D Thin BL Velocity Field for Z Centerline (L) and Y Centerline (R)	99
Fig. 5.19 3D Thin BL Unstart Pressure at $t = [0.05, 0.10, 0.15, \dots, 0.50]$ ms.....	100
Fig. 5.20 3D Thin BL Unstart Speed vs A) Position, B) Time.....	101
Fig. 5.21 3D Thin BL Unstart Shock Arrival Time.....	102
Fig. 5.22 3D Thin BL Unstart Mach Number at $t = [0.1, 0.2, 0.3, \dots, 0.5]$ ms	103
Fig. 5.23 3D Thin BL Wall Pressure Traces during Unstart at $t = [0.0, 0.1, 0.2, \dots, 0.5]$ ms....	104
Fig. 5.24 3D Thin BL Wall Peak Pressure A) Strength, B) Location.....	105
Fig. 5.25 3D Thin BL Unstart Precursor Signal on Channel A) Bottom, B) Top	106
Fig. 5.26 3D Thin BL Unstart Precursor Signal (all time) on Channel A) Bottom, B) Top.....	106
Fig. 5.27 Psuedo-Schliern Image on Z-Centerline A) 3D High AR, B) 3D Low AR	107
Fig. 5.28 Psuedo-Schliern Image on Y-Centerline A) 3D Low AR, B) 3D High AR.....	108
Fig. 5.29 3D Wall Pressure A) High AR, B) Low AR	108
Fig. 5.30 3D Low AR Fully Started Flow Wall Pressure on Channel A) Floor, B) Ceiling	109
Fig. 5.31 3D Low AR Velocity Field for Z Centerline (L) and Y Centerline (R).....	110

Fig. 5.32 3D Low AR Unstart Pressure at $t = [0.05, 0.10, 0.15, \dots, 0.4]$ ms	111
Fig. 5.33 3D Low AR Unstart Speed vs A) Position, B) Time.....	112
Fig. 5.34 3D Low AR Unstart Shock Arrival Time.....	112
Fig. 5.35 3D Low AR Unstart Mach at $t = [0.05, 0.10, 0.15, \dots, 0.4]$ ms.....	113
Fig. 5.36 3D Low AR Wall Pressure Traces during Unstart at $t = [0.0, 0.1, 0.2, 0.3]$ ms.....	114
Fig. 5.37 3D Low AR Unstart Peak Pressure A) Strength, B) Location	115
Fig. 5.38 3D Low AR Unstart Precursor Signal on Channel A) Bottom, B) Top	116
Fig. 5.39 3D Low AR Unstart Precursor Signal (all time) on Channel A) Bottom, B) Top	116

ABBREVIATIONS

AR	Aspect Ratio
BCGSTAB	Biconjugate Gradient Stabilized
BL	Boundary Layer
CFD	Computational Fluid Dynamics
CFL	Courant-Friedrichs-Lewy
FGMRES	Flexible Generalized Minimal Residual
GCI	Grid Convergence Index
GMRES	Generalized Minimal Residual
LU-SGS	Lower-Upper Symmetric-Gauss-Seidel Method
PDE	Partial Differential Equation
PIV	Particle Image Velocimetry
RANS	Reynolds-Averaged Navier-Stokes
SA	Spalart-Allmaras
URANS	Unsteady Reynolds-Averaged Navier-Stokes

NOMENCLATURE

A	Area
a, b, c	Source Term Length Scales
c_{b1}, c_{w1}, c_{b2}	SA Constants
C_f	Skin Friction Coefficient
c_p	Specific Heat
d	Wall Distance
E	Energy
e	Parallel Efficiency
f	Studied Variable in Richardson Extrapolation
F^c	Convective Flux
F_q	Source Term Force
F^v	Viscous Flux
f_w, f_{v2}	SA Control Functions
GCI	Grid Convergence Index
g	Source Term Spatial Distribution
h	Isolator Height
\bar{I}	Identity Matrix
i, j, k	Source Term Shape Constants
K	Source Term Scaling Factor
M	Mach number
\hat{n}	Unit Vector
P	Pressure
p	Number of Processors
Pr	Prandtl Number
Q	Source Term Vector
q	Source Term Scalar
R	Universal Gas Constant
r	Source Term Radius
Re	Reynolds Number

\tilde{S}	Strain Rate Scalar
s	Speedup
T	Temperature
t	Time
U	Vector of Conservative Variables
u, v, w	x, y, z Velocity
V	Velocity vector
x, y, z	Spatial Position
y^+	Non-Dimensional Wall Distance
$\Gamma(x)$	Euler Gamma Function
γ	Specific Heat Ratio
δ	Boundary Layer Thickness
ε	Grid Refinement Ratio
ζ	Order of Convergence
θ	Flap Angle
μ	Dynamic Viscosity
ν_t	Turbulent Kinematic Viscosity
$\tilde{\nu}$	Turbulence Variable for SA Modeling
ρ	Density
σ	Turbulent Prandtl Number
$\bar{\tau}$	Strain Rate Tensor
φ	Serial Fraction
ω	Van Driest Power Law Value

Superscript

ex	Exit
k	Index from 1 to 2

Subscript

–	Mean Quantity
0	Total Quantity

1, 2, 3	Grid Number
∞	Freestream Quantity
c	Centroid
dyn	Dynamic
exact	Grid Independent Value
in	Inlet
p	Parallel
s	Serial
turb	Turbulent
w	Near-Wall Quantity
x	Horizontal Position/Direction
θ	Momentum Thickness Based

ABSTRACT

Author: Hall, Ian, A. MS

Institution: Purdue University

Degree Received: May 2019

Title: Simulating Scramjet Behavior: Unstart Prediction in a Supersonic, Turbulent Inlet-Isolator Duct Flow

Committee Chair: Jonathan Poggie

In the pursuit of developing hypersonic cruise vehicles, unstart is a major roadblock to achieving stable flight. Unstart occurs when a sudden instability in the combustor of a vehicle's propulsion system creates an instantaneous pressure rise that initiates a shock. This shock travels upstream out of the inlet of the vehicle, until it is ejected from the inlet and creates a standing shockwave that chokes the flow entering the vehicle, thereby greatly reducing its propulsive capability. In severe cases, this can lead to the loss of the vehicle. This thesis presents the results of a computational study of the dynamics of unstart near Mach 5 and presents some possible precursor signals that may indicate its presence in flight. Using SU2, an open-source CFD code developed at Stanford University, the Unsteady Reynolds-Averaged Navier-Stokes equations are used to develop a model for flow in a scramjet inlet-isolator geometry, both in the fully started state and during unstart. The results of these calculations were compared against experimental data collected by J. Wagner, at the University of Texas, Austin. In the present computations, unstart was initiated through the use of an artificial body force, which mimicked a moveable flap used in the experiments. Once the results of the code were validated against these experiments, a selection of parametric studies were conducted to determine how the design of the inlet-isolator by Wagner affected the flow, and thus how generalizable the results can be. In addition, precursor signals indicative of unstart were identified for further study and examined in the different parametric studies. It was found that a thick boundary layer is conducive to a stronger precursor signal and a slower unstart. In addition, an aspect ratio closer to 1:1 promotes flow mixing and reduces the unstart speed and strength. Moreover, an aspect ratio in this range reduces the precursor signal strength but, if a thick boundary layer is present, will smear the signal out over a larger area, potentially making it easier to detect.

1. INTRODUCTION

The design of high-speed, reliable propulsion systems has been a major driving force of aerospace research for more than fifty years. The possibility of air-breathing propulsion systems to power vehicles and payloads far past the speed of sound is an expanding area of research both on the national and international scales. For both civilian and military applications, supersonic (Mach 1-5) and hypersonic (Mach 5+) cruise vehicles represent the future of transport. However, sustained hypersonic flight is still held back by a number of significant technological barriers associated with the inherent thermal stresses, high mechanical loads, and complex control requirements of flying at such speeds [1]. This thesis will focus on a technological barrier internal to the air-breathing propulsion system, namely hypersonic unstart. A deeper understanding of hypersonic aerodynamics and propulsion is required on a general scale to combat the problem of unstart. More specifically, expanding the knowledge base surrounding the shockwave boundary layer interactions that happen within the propulsion systems of such vehicles is essential for developing methods to prevent or short-circuit unstart in flight.

This chapter discusses the relevant propulsion technology for hypersonic flight and the inherent difficulties associated with air-breathing propulsion at hypersonic speeds. It continues with a description of the scope of the research for this thesis and a brief summary of the following chapters.

1.1 Hypersonic Flight

To achieve supersonic cruise, the ramjet was developed. A ramjet is a fully bladeless air-breathing propulsion system that uses a compression shock train, rather than a cascade of compressor airfoil arrays, to condition the freestream airflow for combustion. A series of oblique shocks, known as a shock train, acts to slow the incoming air to subsonic speeds before it reaches the combustor, ideally with minimal pressure drop across the series of shocks. These shocks are usually assisted by a mixed-compression inlet, where a ramp preceding the engine inlet initiates the shock train, which continues into the system internals. The air then enters the combustor as if compressed with a typical turbine system, usually around Mach 0.3 to Mach 0.4 [2]. Due to the

lack of a conventional compressor, however, these systems generally do not work below speeds of Mach 2 [3].

Once a vehicle exceeds Mach 5, it enters the hypersonic regime. This transition is marked by a rapid rise in the heating and air turbulence surrounding the vehicle, as well as within the propulsion system itself. As a vehicle approaches this Mach 5 transition, it becomes unfeasible to slow the incoming air to subsonic speeds before it reaches the combustor. To do so would require an unrealistically long shock train between the inlet and the combustor. Additionally, the rise in static temperatures through this shock train would become so high that the amount of cooling required to keep the system from melting would be extremely impractical. Furthermore, even if the propulsion system could be cooled or made from materials that could withstand such unreasonable temperatures and was long enough to slow the inflow to subsonic speeds, the air temperature in the system quickly becomes higher than the adiabatic flame temperature of the fuel prior to entering the combustor [4]. This means that the fuel will break down into its constituent atoms in a decomposition process, rather than burning.

To address these inherent design limitations of the ramjet, the supersonic combusting ramjet, or scramjet, was developed. In a scramjet, the internal airflow is still slowed, but remains supersonic as it enters the combustor. One major design difference between a ramjet and a scramjet is the transition between the inlet and the combustor. In a ramjet, the inlet compresses the incoming air and feeds it directly into the combustor. The inlet usually features some form of mixed compression with a converging-diverging section that forms a normal shock prior to the combustor. In a scramjet, the compression inlet is separated from the combustor by a duct called the isolator, which is typically a constant area section that contains an oblique shock train. This means that the diverging section of the ramjet is no longer present. A comparison of a simplified ramjet and scramjet schematic is shown in Fig. 1.1. These sketches show the system geometry from inlet to outlet along a centerline slices of the system, with the leftmost side being the inlet side and direction of flight. The geometrical differences between the two designs becomes most apparent in the central portion of the system.

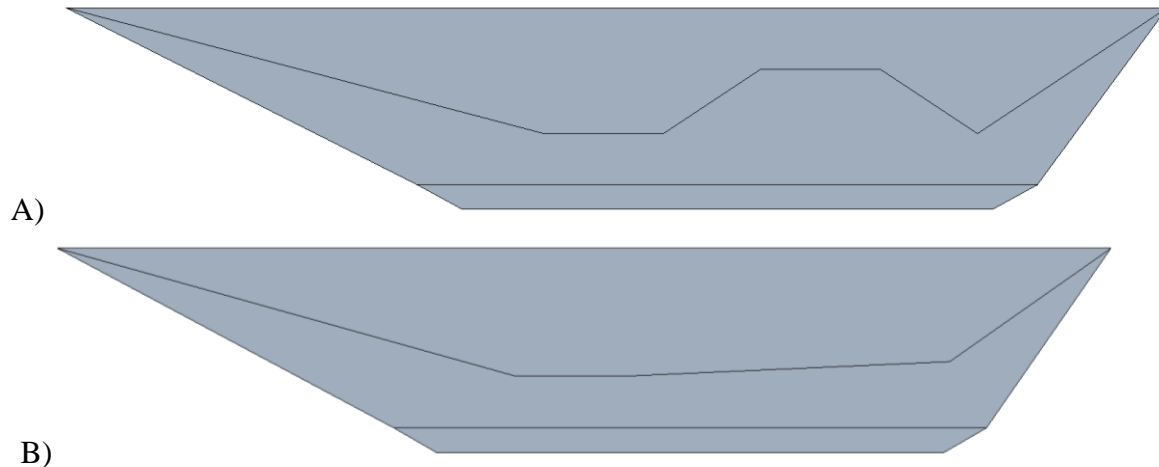


Fig. 1.1 Schematic, adapted from Anderson et al. [5] of A) Ramjet B) Scramjet

The design of the scramjet, while geometrically less complex, also has a major limitation. As previously mentioned, a scramjet does not slow down the incoming airflow to subsonic speeds. This is facilitated by the lack of a converging-diverging section within the nozzle which would induce a normal shock, truncating the oblique shock train and bring the flow into the subsonic regime. Owing to this fact, it cannot operate at speeds less than roughly Mach 4 [2].

1.2 Dual-Mode Scramjet

Full transition from low supersonic to hypersonic speeds requires both ramjet and scramjet propulsion. In order to tackle this design challenge in a cost and weight efficient manner, the dual-mode scramjet design was proposed in 1964 [6]. The dual-mode scramjet is an air-breathing propulsion system that can function in both supersonic and hypersonic flight. It effectively acts as a ramjet for the supersonic portion of flight, slowing air to subsonic speeds before combustion, and transitions to a full scramjet with supersonic combustions at hypersonic speeds. With an invariant geometry, it is theoretically capable of working with internal airflows entering the combustor at subsonic, transonic, and supersonic speeds.

The dual-mode scramjet consists of four major components, namely the inlet, the isolator, the combustor, and the nozzle [7]. These components, shown in Fig. 1.2, act in concert to create thrust for the vehicle. The freestream airflow enters through the inlet, where there is usually a compression ramp present on the vehicle forebody. This ramp serves to initiate the series of oblique shocks that are known as the shock train. At the end of the ramp, the isolator begins. The isolator

is normally a constant area section of duct that isolates the combustor, and any associated instabilities within it, from the inlet. Moreover, it contains the shock train and is where the series of shocks can slow and condition the flow for combustion. Third, the combustor resides at the exit of the isolator. It works much like a conventional air-breathing engine's combustor, but must be able to combust the air in a very short period of time, due to its speed. Additionally, there is usually a component called a flameholder that shields the pilot flames of the combustor from the incoming airflow to prevent them becoming extinguished by the supersonic air that is moving past. Finally, there is the nozzle, which acts to expand and accelerate the flow leaving the propulsion system for maximum thrust.

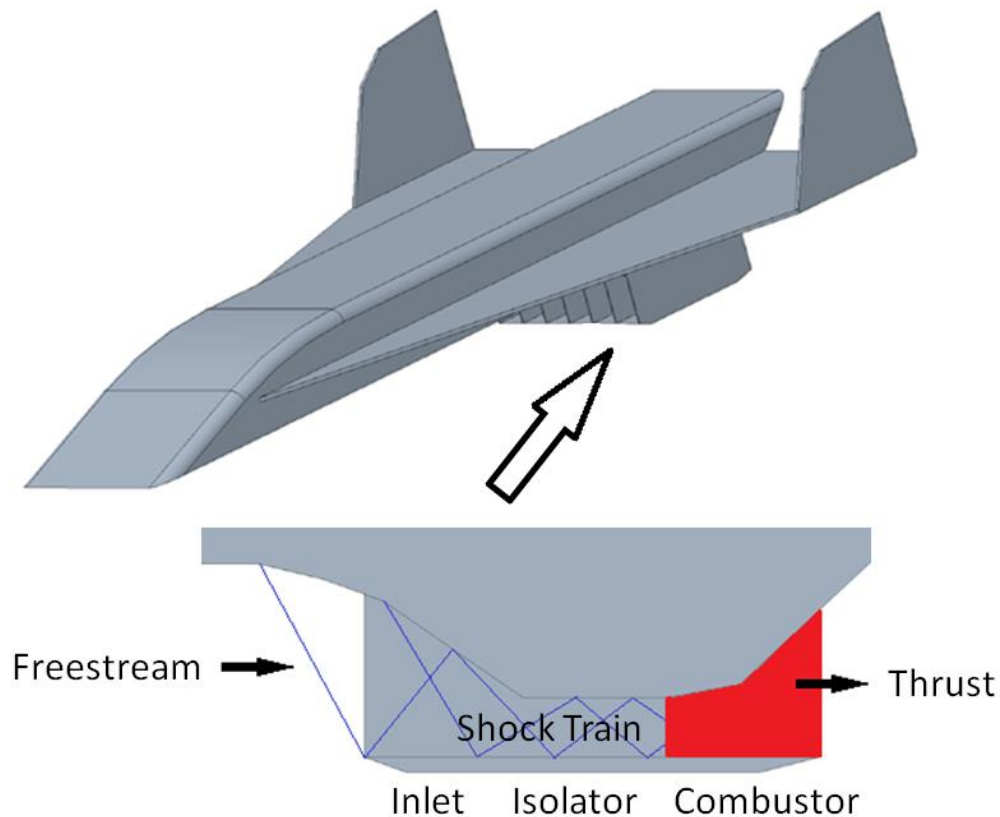


Fig. 1.2 Scramjet Schematic

Of the four major components mentioned, the isolator warrants some special attention. When scramjets were first being designed, the inlet led directly in to the combustor, but it was quickly determined that there was a need for a duct to separate the inlet from pressure fluctuations created by the combustor [8]. The isolator has proven to be effective at separating the combustor

disturbances from the inlet, allowing scramjets to have a wider range of operation. However, this range is still quite small and poorly understood, as unstart still occurs when these disturbances are strong enough to reach the inlet. To enable a more complete solution, the research presented here delves into the flow mechanisms and dynamics within the inlet-isolator system during hypersonic flight.

1.3 Unstart

Increasing a vehicle's speed into the hypersonic regime comes with a number of significant hurdles. In regard to the propulsion system, a major difficulty of sustained hypersonic flight with a dual-mode scramjet is unstart. Unstart is a catastrophic loss of propulsion where the airflow captured within the dual-mode scramjet is pushed upstream from the combustor, through the isolator, and finally expelled out the inlet. A bow shock can form in front of the inlet, choking the path to the combustor. With little to no oxidizer available, the vehicle will experience a sudden loss of thrust that will likely lead to the loss of the vehicle [9].

Unstart becomes a key limiter when the internal airflow moving from the inlet into the combustor enters the supersonic regime, in scram mode. Substantial flow instabilities and the inherent difficulty of combustion at such a low residence time leads to intense turbulence. The internal turbulence and the variability in the combustion conditions can cause sudden unstable pressure rises within the combustor that lead to unstart [6].

Studies have been conducted on engine restart and vehicle recovery following unstart of a hypersonic vehicle [10], but preventing unstart from occurring is still a prominent issue being tackled. To this end, numerous studies, both experimental and computational, have been conducted to develop a deeper understanding of unstart and the instabilities that lead to it. Several mechanisms for causing unstart have been identified, from thermal choking [11], to combustor pressure rise [12], to freestream disturbances [13].

Fike et al. initiated unstart through the injection of a crossflow midway through the isolator [14]. Examining a Mach 4.6 flow, they injected a jet perpendicular to the flow direction at approximately $x/h = 4$ from the inlet. At this point in the flow, the boundary layer was relatively small and had little influence on the unstart characteristics. However, the mass injection method seemed to be a relatively blunt forcing mechanism for unstart, when compared to a moveable flap.

1.4 Scope of Research

Hypersonic unstart in a dual-mode scramjet is an area of active research and a major roadblock to hypersonic cruise vehicles because it is unpredictable and not well understood. Hypersonic vehicles are notoriously difficult and expensive to test. Since the loss of the X-51 test vehicle to unstart [15], scramjet research has mostly been relegated to wind-tunnels and computer codes. Many researchers have looked at ways to bound unstart [16], as well as both passive and active mitigation strategies [17] for stopping unstart. However, unstart detection is still unresolved.

This paper will use the unstart experiments conducted by Wagner et al. [12] [18] [19] [20] for validation of the computational model. In these experiments, unstart was successfully demonstrated in an inlet-isolator model in a Mach 5 flow. The details of the studies will be discussed in Chapter 2. These experiments have been used as a basis for a number of computational studies, including one that examined the ability of RANS simulations to predict unstart [21]. In that study, Jang et al. validated the computational approach but found some error in the speed of unstart. Using that study and the aforementioned experimental data as a starting point, this paper aims to more fully simulate unstart in a computational domain, with a static, structured grid, and search for precursors to unstart under various flow conditions, while gaining a deeper understanding of the dynamics of unstart.

A search for telltale signs of imminent unstart is conducted and this paper will look into the physics of unstart and hunt for an observable precursor event. Since unstart is an event that originates in the combustor and propagates through the isolator and out the inlet, the focus on this paper will be on the first two sections of the propulsion system, the inlet and the isolator. Unstart will be induced at the exit of the isolator (entrance to the combustor) and the internal flow field of the inlet-isolator system will be studied.

The study of unstart has been conducted in a series of computational experiments that build on each other. In Chapter 2, the general flow conditions and the specifics of the inlet-isolator model will be discussed. The series of experiments conducted by Wagner et al. at the University of Texas, Austin [12] [18] [19] [20] is described in detail, as the results of these experiments are used to validate the computational model. An explanation of the computational setup, including code parameters, grid construction, and parallel computing will be developed. Finally, a description and validation of the computational unstart-inducing mechanism will be presented.

In Chapter 3, a 2D computational model is developed and compared to experiment. The desired flow conditions are developed computationally and a grid independence study is presented. A fully started hypersonic flow internal in the inlet-isolator model is shown and discussed in relation to the available experimental data. Directly following, an unsteady simulation is performed and unstart is induced. An examination of the flow characteristics during unstart is presented, and a description of potential unstart precursors concludes the section.

Chapter 4 describes a corresponding set of simulations conducted in three dimensions. This chapter again compares the computational results to experiment, as well as to the 2D results in the previous chapter. A discussion of the three dimensional flow field, both in the started condition and during unstart, is presented. Major differences and important similarities between the two computational models are highlighted, with possible explanations for changes in the flow dynamics postulated. Finally, the unstart precursors found in the two dimensional case are re-examined in three dimensions.

Next, Chapter 5 details a selection of parametric studies of the inlet-isolator model dynamics in two and three dimensions. This chapter uses the grounding of the previous two chapters to develop a more general understanding of the started and unstarted flow characteristics. First, a modification in the inlet flow parameters is applied to the 2D case from Chapter 3, specifically a reduction in the floor boundary layer thickness, and its effects on the structures and dynamics of the steady-state and transient flow states are examined. Next, the 3D mesh is used to study this same difference in boundary layer thickness, to see how the influence of three dimensional effects may or may not change the flow field. Finally, a modified 3D model with half the width of the original inlet-isolator is used to examine the effect of aspect ratio on the flow within the channel in the steady and transient states.

Last, Chapter 6 summarizes the results, with the main points from each chapter offered, including parallels and differences between the results of different computations and experiments. Next, it presents the conclusions of the research and an assessment of the detected precursor signals. Finally, this chapter suggests avenues for future work, using the results from this research as a foundation for further study.

2. METHODOLOGY

The background of experiments that will serve as the validation for the computations is detailed in this section. The general flow conditions and the specifics of the inlet-isolator model will be discussed. In addition, the computational methods used will be presented, including both the relevant analytical equations and the computational parameters needed to develop a reasonable simulation of the flow. The grids used in the study are shown, along with the method of initiating unstart in the flow.

2.1 Experimental Background

Wagner et al. built and tested an inlet-isolator model, mounted in the Mach 5 wind tunnel at the University of Texas, Austin [12] [18] [19] [20]. This model was designed to unstart on command in order to gain a better understanding of the underlying flow physics and turbulent interactions in an unstart event. Wagner demonstrated repeatable unstart using a deployable flap to simulate a sudden pressure rise or flow blockage coming from the combustor. The flap was mounted at the exit of the isolator and, when raised to a critical angle, a high-pressure shock was formed at the location of the flap. This shock would propagate upstream towards the inlet, destroying all flow structures in the started flow, and eventually exit the system through the inlet.

The referenced experiments conducted at the University of Texas, Austin examined a range of variables relating to the inlet-isolator model, including ramp angles of the inlet, different flap rise times, and variations in freestream conditions. For the purposes of the computational studies described in this paper, only one of the tested model configurations will be examined. The test set was chosen from the experiments reported on because it had the most available information regarding the setup and results.

The specifics of the inlet-isolator model geometry are as follows. The experimental inlet-isolator is a rectangular channel with a 6 degree inlet ramp on the roof of the inlet section. The inlet occupies roughly one third of the channel, lengthwise. Thus, of the total channel length of 333 mm, the inlet section with the 6 degree ramp is the first 90.7 mm. The isolator occupies the rest of the model and measures 242.3 mm in length. The height of the channel at the entrance to the inlet is 34.9 mm, with a decreasing height through the inlet due to the roof ramp. The channel

has a rectangular cross-section, measuring 25.4 mm in height in the isolator and 50.8 mm in depth throughout. A rendering of this inlet-isolator test section mounted in the Mach 5 wind tunnel is shown in Fig. 2.1.

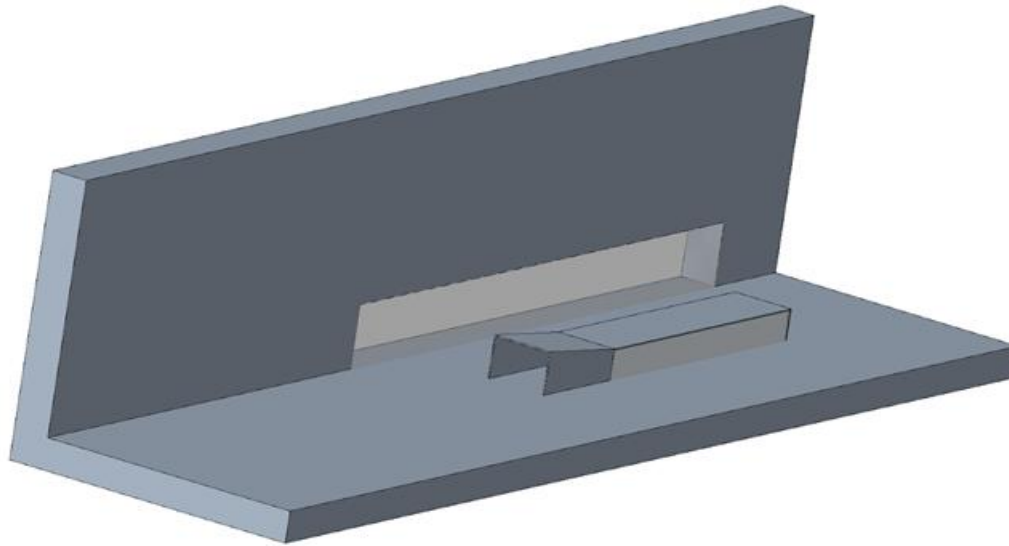


Fig. 2.1 Inlet-Isolator Mounted in Wind Tunnel

A dimensional schematic of the inlet-isolator geometry in 2D is shown in Fig. 2.2. Note that this is the internal contour of the inlet-isolator, i.e. the relevant part for a computational grid. This is the section on which all the flow fields generated will focus.

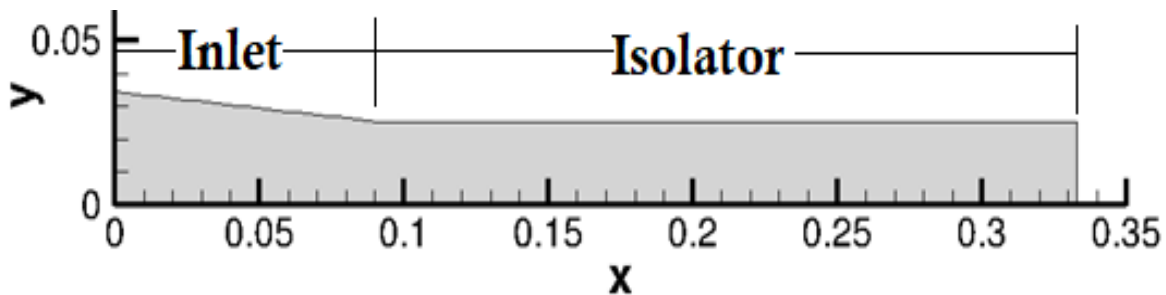


Fig. 2.2 Inlet-Isolator Test Section (axes in m)

Wagner measured the freestream conditions across the series of experiments and lists the following as the relevant values [18]: total temperature $T_0 = 328$ K, total pressure $P_0 = 2.465$ MPa, and incoming Mach number $M = 4.9$. Using the isentropic flow relations,

$$T_{\infty} = \frac{T_0}{\left(1 + \frac{\gamma-1}{2}M^2\right)} \quad (2.1),$$

$$P_{\infty} = \frac{P_0}{\left(1 + \frac{\gamma-1}{2}M^2\right)^{\frac{\gamma}{\gamma-1}}} \quad (2.2),$$

and

$$u_{\infty} = M\sqrt{\gamma RT_{\infty}} \quad (2.3),$$

the static freestream conditions are determined to be $T_{\infty} = 56.53$ K, $P_{\infty} = 5.240$ kPa, and $u_{\infty} = 738.5$ m/s. These values assume a specific heat ratio of $\gamma = 1.4$, and will be used for the computational flows later in this paper. In addition, the calculated values match with what Wagner gives for the calculated freestream conditions [18]: $T_{\infty} = 56$ K, $P_{\infty} = 5.38$ kPa, and $u_{\infty} = 740$ m/s. Furthermore, the Reynolds number is $Re = 1.318 \times 10^7$.

An important note to take into account when comparing to these experiments is the configuration of the inlet-isolator model as it resides in the wind tunnel. For these experiments, the test section was mounted directly to the floor of the University of Texas, Austin wind tunnel. Due to this design choice, a thick boundary layer develops on the floor of the wind tunnel and is ingested by the inlet as part of the hypersonic flow. This boundary layer, measuring over half the height of the test section itself, is present in all the experiments and has a significant effect on the flow dynamics. The boundary layer thickness, measured by the height at which the flow velocity reaches 99% of the freestream velocity, was $\delta = 19.3$ mm. Conversely, the ceiling of the inlet-isolator begins developing its respective boundary layer only from a sharp leading edge of the test section.

As previously mentioned, the model contains a deployable flap at the exit of the isolator. This flap begins flat to the tunnel floor until a fully started flow develops, then raises to a predetermined angle to initiate unstart. A number of different flap angles were tested. While flap angle did not affect the unstart flow structures, a 26 degree flap was found to be the lowest ramp angle to induce unstart in the experimental model [20]. Therefore, a 26 degree flap was chosen for the computations in this paper as well. Flap deployment time was determined to have no noticeable effect on unstart in the experiments conducted by Wagner et al. [19]. To minimize computational cost, 1 ms was chosen for the CFD model, as it was the shortest time tested in experiment.

2.2 Code Configuration

The computational studies presented in this paper were completed using SU2, an open-source CFD program developed at Stanford University [22]. SU2 is a multiphysics code, written mainly in C++, that is optimized for solving partial differential equations (PDEs) on unstructured meshes [23]. When solving a problem in parallel, two executables, namely SU2_CFD and SU2_SOL, must be run in sequence to attain a data file output. For the problems addressed in this paper, the physical model consisted of the compressible, unsteady Reynolds-Averaged Navier-Stokes (URANS) equations. These were determined to be the most accurate for modeling the turbulence through the inlet-isolator model, while maintaining a reasonable computational cost. The PDE used in solving a URANS problem in SU2 is

$$\frac{\partial U}{\partial t} + \nabla \cdot F^c - \nabla \cdot (\mu^{vk} F^{vk}) = Q \quad (2.4).$$

In Eq. (2.4), U is a vector of the conservative variables, F^c is the vector of the convective fluxes, F^{vk} is a vector of the viscous fluxes, and Q is a generic source term. In addition, F^c , F^{vk} , and Q are functions of U . The full vector notations for each of these variables are written out as

$$U = \begin{pmatrix} \rho \\ \rho V \\ \rho E \end{pmatrix} \quad (2.5),$$

$$F^c = \begin{pmatrix} \rho V \\ \rho V V + \bar{I} P \\ \rho E V + P V \end{pmatrix} \quad (2.6),$$

$$\mu^{v1} = \mu_{dyn} + \mu_{turb} \quad (2.7),$$

$$\mu^{v2} = \frac{\mu_{dyn}}{Pr_{dyn}} + \frac{\mu_{turb}}{Pr_{turb}} \quad (2.8),$$

$$F^{vk} = \begin{pmatrix} 0 & 0 \\ \bar{\tau} & 0 \\ \bar{\tau} \cdot v & c_p \nabla T \end{pmatrix} \quad (2.9),$$

and

$$Q = \begin{pmatrix} q_\rho \\ q_{\rho V} \\ q_{\rho E} \end{pmatrix} \quad (2.10).$$

In the above equations, ρ is density, V is velocity, E is energy, P is pressure, and T is temperature. Additionally, \bar{I} stands for the identity matrix, $\bar{\tau}$ indicates the strain rate tensor, and c_p is the specific heat. Eqs. (2.7) and (2.8) give the mathematical definitions for these two terms.

There are two terms used for viscosity in these equations, μ^{v1} and μ^{v2} . These are each a combination of laminar dynamic viscosity and turbulent eddy viscosity, and stand for the total viscosity and effective thermal conductivity, respectively. Pr is the Prandtl number of the dynamic and turbulent variety.

In Eq. (2.9), the strain rate tensor can be written out more completely as

$$\bar{\tau} = \nabla V + \nabla V^T - \frac{2}{3}\bar{I}(\nabla \cdot V) \quad (2.11).$$

Thus, the PDE in Eq. (2.4) can be broken into three main governing equations,

$$\frac{\partial \rho}{\partial t} + \nabla \cdot (\rho V) = q_\rho \quad (2.12),$$

$$\frac{\partial(\rho V)}{\partial t} + \nabla \cdot (\rho V V + \bar{I} P) - \nabla \cdot (\mu^{v1} \bar{\tau}) = q_{\rho v} \quad (2.13),$$

and

$$\frac{\partial(\rho E)}{\partial t} + \nabla \cdot (\rho E V + P V) - \nabla \cdot (\mu^{v1} \bar{\tau} \cdot v + \mu^{v2} c_p \nabla T) = q_{\rho E} \quad (2.14).$$

In addition to these basic governing equations, SU2 features a number of options concerning numerical models, turbulence modeling, and convergence. For the study presented in this paper, the Weighted-Least-Squares numerical method for spatial gradients was chosen over the Green Gauss method. It is used to calculate the gradients of the flow variables at each individual grid nodes, after which the gradients at the cell faces are found by averaging [23].

Adiabatic walls were chosen for the bounds of the inlet-isolator channel domain, which reduced the computational cost due to the simplified calculations. The rationale was that the total time to unstart is on the order of 10 ms, so any temperature based wall effects would be negligible.

The Spalart-Allmaras (SA) turbulence model was chosen as it is known to be particularly suited for wall-bounded flows, thus making it ideal for the inlet-isolator channel [24]. This turbulence model has an additional advantage in computational cost over other similar models because it solves for the flow field using only a single equation. The single turbulence equation used in this model is

$$\frac{D\tilde{\nu}}{Dt} = \frac{1}{\sigma} \frac{\partial}{\partial x_j} \left[(\nu_t + \tilde{\nu}) \frac{\partial \tilde{\nu}}{\partial x_k} \right] + c_{b1}(1 - f_{v2})\tilde{S}\tilde{\nu} - c_{w1}f_w \left(\frac{\tilde{\nu}}{d} \right)^2 + \frac{c_{b2}}{\sigma} \frac{\partial \tilde{\nu}}{\partial x_k} \frac{\partial \tilde{\nu}}{\partial x_k} \quad (2.15),$$

where the dependent variable is the turbulent kinematic viscosity, ν_t .

In this equation, the term $\tilde{\nu}$ is the turbulence variable and is a key part of the equation. It is a scaled eddy viscosity such that it can be applied through the entire boundary layer, from viscous sublayer, to buffer layer, to log layer. Similarly, \tilde{S} is a modified version of the scalar form of the

strain rate tensor, such that it can be used through the entire boundary layer. The variable d is the distance to the closest wall, and σ is a turbulent Prandtl number. Finally, f_w and f_{v2} are control functions, while c_{b1} , c_{w1} , and c_{b2} are constants. These constants are calibrated empirically, using a combination of experimental and numerical results to achieve an approximation of the correct turbulence behavior. Likewise, the functions are normalized based on the constants, meaning their construction is semi-empirical as well.

These equations were solved using a Flexible Generalized Minimal Residual (FGMRES) linear solver. This solver, natively built into SU2, was found to be more stable than the Biconjugate Gradient Stabilized (BCGSTAB) solver in the course of this study. In addition, the FGMRES solver adds significant stability to the GMRES solver by enabling a variety of different preconditioners to be applied to the PDE to make the solver more robust [25].

The flow uses a first order Roe scheme and an Euler implicit time discretization setup. Initially, a second order Roe scheme was used in an effort to better resolve the shocks within the system. However, the scheme proved unstable in the highly dynamic environment of unstart once it was initiated. In addition, with the experimental validation of the first order Roe scheme, it was deemed to have high enough accuracy for the current investigations.

A scalar upwind convective numerical model, using a second order Venkatakrishnan limiter with a Lower-Upper Symmetric-Gauss-Seidel Method (LU-SGS) preconditioner is implemented in the code to speed convergence of the solution set. This combined method was found to be the most stable configuration for the studied flow and has been shown to be effective for hypersonic flows in the past [26] [27]. The flows were run with an adaptive CFL number, with a minimum of 0.1 and a maximum of 100, to stabilize the calculations and speed up where possible.

Once a steady state flow field was generated, creating a fully started flow configuration, unstart was initiated. As a time-dependent flow, the unstart flow fields were calculated using a dual time stepping method, with a time step of $t = 0.1 \mu s$, based on the minimum Δy^+ value. Each physical time step contained 50 internal iterations, and the flow was run for the requisite physical time for unstart to fully propagate upstream through the inlet-isolator channel and reach the inlet of the test section.

2.3 Mesh Generation

All of the computational grids used in this study were created using the commercial mesh generation software Pointwise [28]. A large number of meshes were generated in the course of this

study, and the final grids utilized for the results presented here are detailed in this section. The first set of three grids (coarse, medium, and fine) were used to develop the inlet conditions that would be seen by the inlet-isolator model. The second set of three grids model the inlet-isolator in 2D, with increasing resolution to match the coarse, medium, and fine meshes of the first three. The next grid is a 3D inlet-isolator model at the finest resolution. Due to the difficulty of imposing a boundary layer on the 3D grid, another two 3D grids of the inlet-isolator model were developed to develop the boundary layer in situ. Next, a 3D grid of the inlet-isolator system with a reduced aspect ratio was created for a parametric study. Lastly, a 2D and a 3D grid were created for validation of the source term that would be used to initiate unstart.

2.3.1 2D Flat Plate Grids

The first set of grids was generated to develop the thick boundary layer to be imposed at the entrance of the inlet-isolator domain. In principle, the boundary layer could have been a single grid with the inlet isolator, but separating the two greatly reduced the computational cost of the calculations. These grids were designed for a flat plate boundary layer calculation. A sample grid can be seen in Fig. 2.3, below. The grid features clustering of the mesh points along the floor, to ensure sufficient resolution in the boundary layer. A reference length of 1 m was used when creating the grids used in this thesis, and the flat plate grids are 2 m in height and 5 m in length. This is an order of magnitude larger than the size of the inlet-isolator, and this large scale is necessary in order to ensure that the boundary layer is fully developed. The wind tunnel boundary layers reach an analogous state via more complex processes in the nozzle. In addition, there is a slip transition point at $x = 0.5$ m. This means that the bottom wall boundary condition is set as a slip wall, highlighted in yellow, from $x = 0.0$ m to $x = 0.5$ m, and then becomes a no-slip wall, highlighted in orange, from $x = 0.5$ m to $x = 5.0$ m. This transition point starts the boundary layer development and represents the beginning of a flat plate in the flow. The flow is from left to right, with the left-hand boundary, highlighted in light green, set as a Mach 4.9 inlet. The top and right-hand boundaries, highlighted in blue, are supersonic outlets.

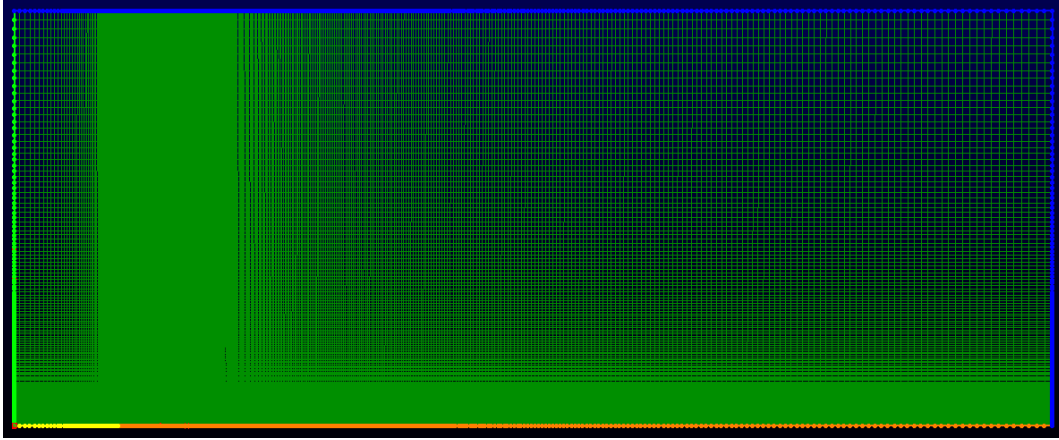


Fig. 2.3 2D Flat Plate Grid Boundary Conditions

The coarse grid was designed to have a Δy^+ value of 0.1 at the wall, in the floor boundary layer, based on the freestream conditions. The medium and fine grids are scaled from the coarse grid, using a scaling factor of roughly two for the total number of points (i.e. a factor of $\sqrt{2} = 1.4$ in each coordinate direction). The three grids, shown in Fig. 2.4, are used to compare the flow field and ensure grid independence of the solution. The coarse, medium, and fine grids used to develop a flat plate solution were 197,376 mesh points (196,352 cells), 443,520 mesh points (441,984 cells) and 789,504 mesh points (787,455 cells), respectively.

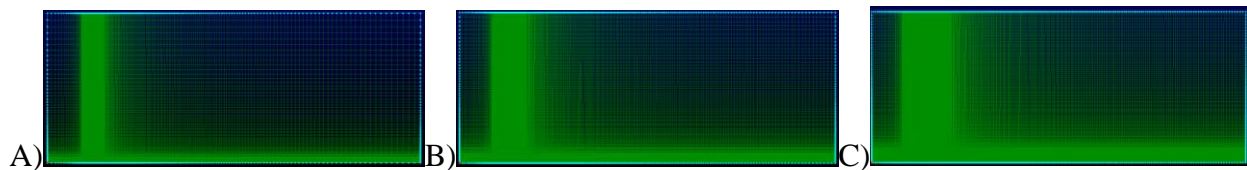


Fig. 2.4 2D Flat Plate Grids A) Coarse, B) Medium, C) Fine

2.3.2 2D Inlet-Isolator Grids

The next set of three grids were the 2D inlet-isolator meshes. These three grids use the same scaling as their respective flat plate grids, in order to ensure that the boundary layer can be imposed accurately at the inlet. The three meshes encompass the entire inlet-isolator domain. In addition, the mesh is extended left of the inlet entrance and right of the isolator exit to ensure that the time-dependent solution of the unstart flow remains unaffected by the mesh boundary to allow for an

accurate flow solution. The experimentally relevant part of the mesh, encompassing the inlet-isolator test section, is shown between the two red lines in Fig. 2.5. Again, there is grid clustering within the inlet-isolator test section to fully resolve the flow field within.

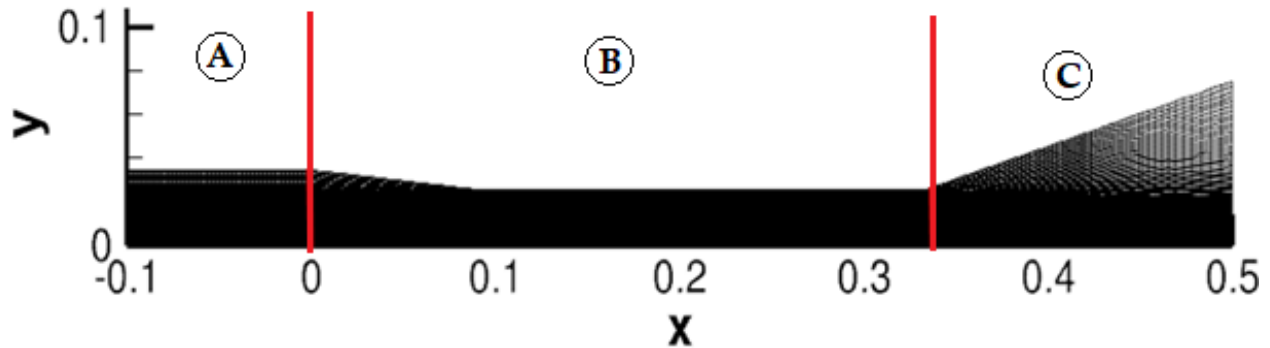


Fig. 2.5 Inlet-Isolator Expanded Mesh (axes in m)

The 2D inlet-isolator meshes can be divided into 3 main sections, A, B, and C, as seen above in Fig. 2.5. Section A stretches from $x = -0.1$ m to $x = 0$ m and is the expanded left-hand portion of the mesh that precedes the inlet-isolator itself. In this section, the Mach 4.9 flow developed on the flat plate meshes is imposed at the left-hand boundary. The upper and lower walls of this section are defined as a slip wall, allowing the top boundary layer to begin at the entrance to the inlet-isolator in section B and preventing the extracted floor boundary layer from experiencing further growth before it reaches the inlet.

The next portion of the mesh, section B, extends from $x = 0$ m to $x = 0.333$ m and represents the inlet-isolator model. The top and bottom boundaries are no-slip walls and the mesh has its finest resolution in this portion of the grid. This is the portion of the grid where the important flow dynamics take place, and flow field plots in the subsequent chapters of this thesis will only show results from this region.

The final part of the mesh, section C, continues from $x = 0.333$ m to $x = 0.5$ m and contains the flow that is exiting the test section. It features slip walls on the upper and lower boundaries. Since the flow should exit section B supersonically, the flow in section C should not affect section B, and this configuration avoids unphysical interference of the outlet boundary condition and the subsonic sections of the flow close to the walls. Finally, the right-hand boundary of the mesh is set as a supersonic exit.

As previously mentioned, three 2D inlet-isolator meshes were used in this study. The coarse, medium, and fine meshes measure 56,072 mesh points (54,891 cells), 123,228 mesh points (121,484 cells), and 248,912 mesh points (213,510 cells), respectively. These three meshes, shown in Fig. 2.6, are used to determine grid independence of the solution.

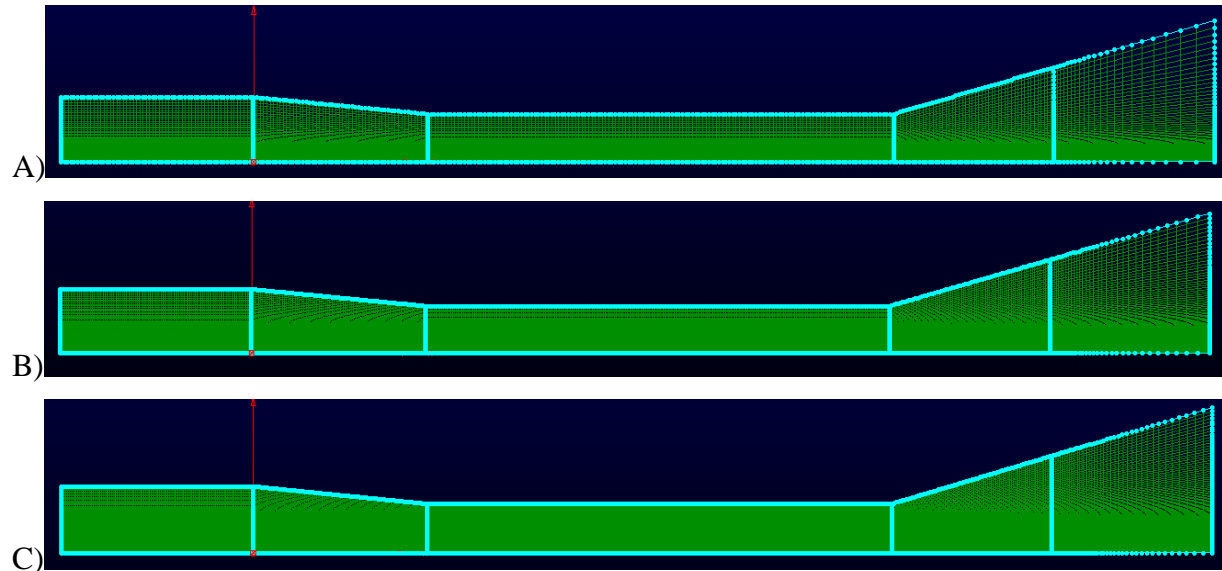


Fig. 2.6 2D Inlet-Isolator Grids A) Coarse, B) Medium, C) Fine

The boundary conditions for the 2D inlet-isolator meshes are shown in Fig. 2.7. Again, the Mach 4.9 inlet is at the left, highlighted in blue, and the supersonic outlet is the rightmost boundary, highlighted in yellow. The orange boundaries mark the no-slip wall regions. The green highlighted regions represent slip walls. The left no-slip wall allows for a boundary layer to begin developing on the ceiling of the channel at the sharp leading edge of the inlet-isolator model. The boundaries right of the isolator exit are designed to eliminate any outside interference on the flow field in the channel.



Fig. 2.7 2D Inlet-Isolator Grid Boundary Conditions

2.3.3 3D Inlet-Isolator Grids

The next set of meshes used in this study are the 3D inlet-isolator mesh models. The grid spacing in this mesh corresponds to the fine spacing variant of the previous 2D mesh. As in the 2D mesh, extra regions are included in the domain before and after the inlet-isolator itself to minimize boundary condition interference. The 3D mesh, shown in Fig. 2.8, is used for studying any three dimensional effects such as corner vortices that might change the flow behavior during the unstart process. The extent to which these three dimensional effects affect the inlet-isolator being studied will be examined, both in the fully started flow and during unstart. This grid consists of 13,083,768 mesh points (12,810,600 cells).

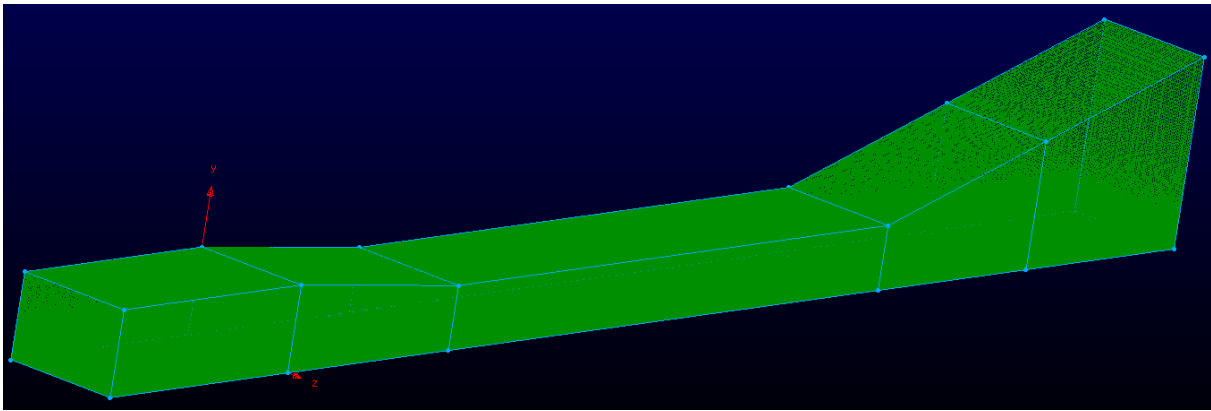


Fig. 2.8 3D Inlet-Isolator Grid

In Fig. 2.9, the experimentally relevant portion of the grid, representing the inlet-isolator model, is shown in green, with the extra mesh surrounding it in white. While this grid worked well for analyzing the flow in the absence of a large boundary layer, implementing the thick boundary layer on the 3D channel proved quite problematic. Imposing the desired flow field parameters across the inlet would always lead to the development of non-physical points. These non-physical points, representing negative densities would rapidly increase in number, until the calculation would diverge. Thus, this mesh could only be used for inflow condition that did not have an imposed boundary layer, shown in the parametric studies section in Chapter 5. Thus, another 3D inlet-isolator mesh was required in order to simulate the full experimentally accurate inflow conditions that were used in experiment and in the initial 2D computations that will be shown in Chapter 3.

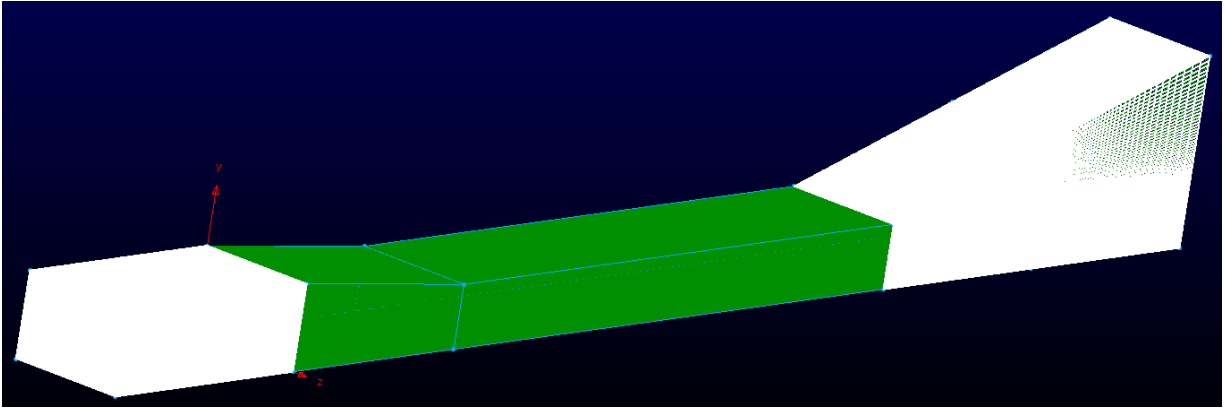


Fig. 2.9 3D Inlet-Isolator Test Section Model in Green

To avoid this problem, a grid was created that would develop the boundary layer in place. This mesh, seen in Fig. 2.10, includes the flat plate with the inlet-isolator. The actual inlet-isolator portion of the mesh is identical to the one shown in Fig. 2.9. In addition, the mesh spacing of the flat plate portion was matched to the inlet, with slip walls and a boundary layer trip. In addition, there is a sponge layer near the top edge of the mesh in the flat plate section to reduce any computational reflections.

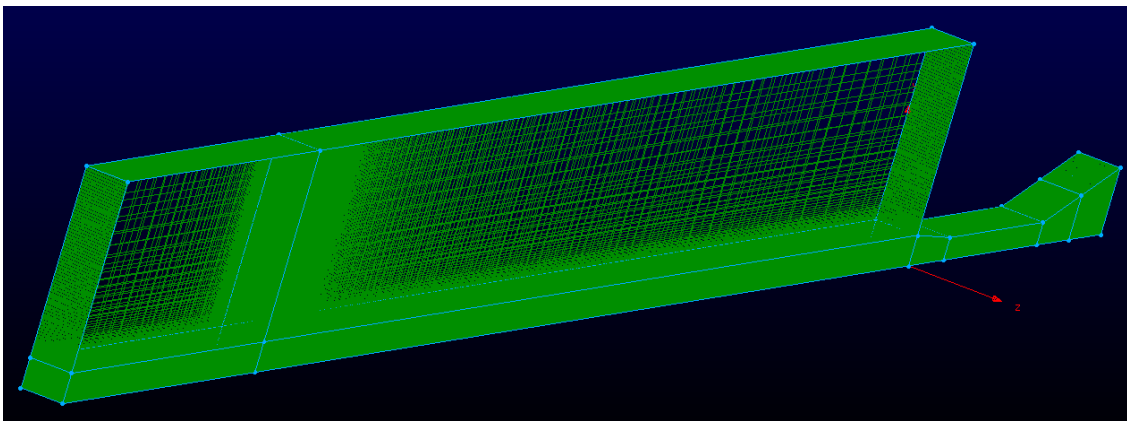


Fig. 2.10 3D Flat Plate plus Inlet-Isolator Mesh

This new 3D mesh consisted of 31,148,979 mesh points (30,511,080 cells). In order to ensure grid independence, a medium and coarse version of this grid were created, which matched the grid spacing of the medium and coarse grids for the 2D mesh. This 3D medium mesh was 13,804,417 mesh points (13,426,8430 cells) and the coarse mesh was 8,031,992 mesh points (7,836,120 cells). The boundary conditions on these two meshes are shown in Fig. 2.11. The lefthand side is again

the inlet, in blue. The top of the flat plate section, as well as the right hand boundaries of both sections are supersonic outlets, marked in yellow. The entire inlet-isolator is made of no-slip walls, in orange, as is the portion of the flat plate section that physically represents a flat plate. The first 0.5 m of the flat plate section of the mesh has a slip wall, which allows development to the correct height before the flow enters the inlet-isolator, or is exhausted above it. The inlet-isolator is still 333 mm long, minus the expanding exit portion. Not including the 0.5 m long slip region, the flat plate measures 2.2 m long, which was determined to be the required length to develop the correct boundary layer height at the tested freestream flow conditions.

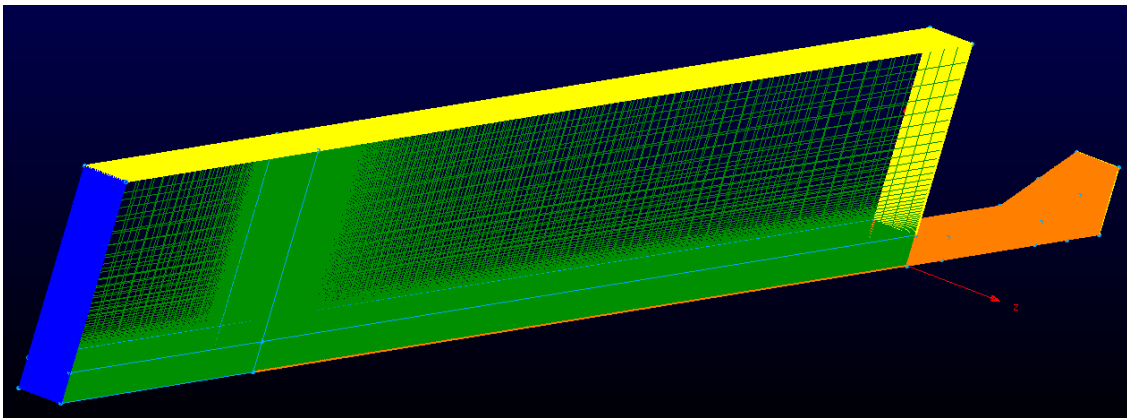


Fig. 2.11 3D Flat Plate plus Inlet-Isolator Mesh Boundary Conditions.

The final 3D inlet-isolator mesh was used for the purposes of a parametric study on the effect of aspect ratio on the flow field dynamics. This mesh used the same grid spacing and boundary conditions as the flat plate plus inlet-isolator mesh, as shown in Fig. 2.11. However, the width was cut in half such that it matched the height of the isolator. This means that the channel had a width of 25.4 mm, rather than 50.8 mm. This 3D low aspect ratio mesh consisted of 15,829,809 mesh points (15,255,540 cells).

2.3.4 Source Term Grids

The final two meshes used in the course of the research presented here were created for testing of the source term implementation. The source term was used to simulate the flap in the experiments and was the mechanism that initiated unstart in the study. A 2D and a 3D mesh were created and were composed of 30,000 mesh points (29,601 cells) and 12,000,000 mesh points (11,840,699 cells), respectively. The grids, shown in Fig. 2.12, were 1 m x 3 m and 2 m x 3 m x 2

m, with an evenly spaced mesh distribution. The domains consists of an inlet at the leftmost boundary, an outlet at the rightmost boundary, and slip walls linking the inlet and outlet. The meshes were designed such that the source term could be isolated in the middle of the grid studied without having to consider the effect of reflections or other extraneous effects on the flow.

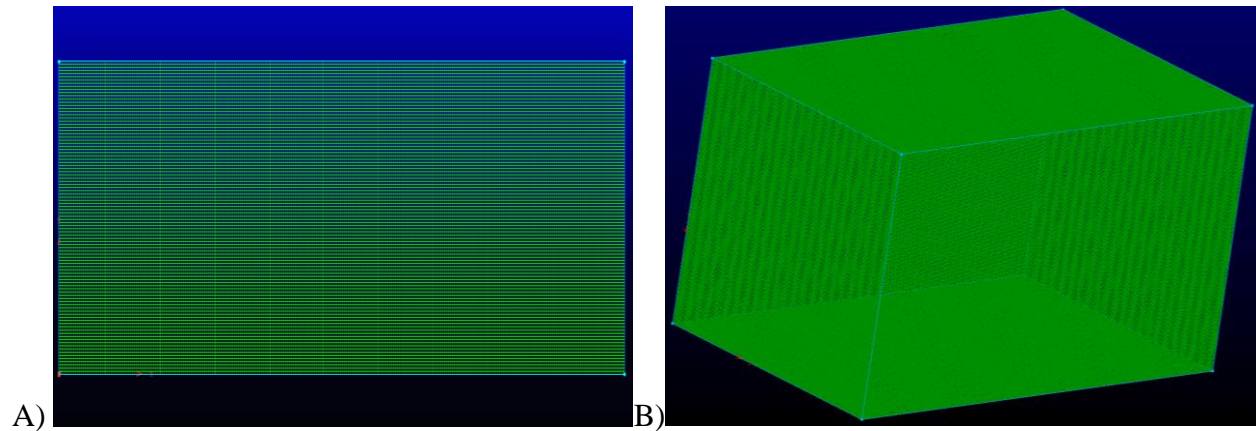


Fig. 2.12 Source Term Mesh A) 2D, B) 3D

2.4 Computation Scaling Study

The simulations were run primarily on Purdue University's Halstead high performance computing community cluster. The cluster gives access to 512 of compute nodes which each are powered by two 10-core Intel Xeon-E5 processors and each of these 20-core nodes has 128 GB of RAM [29]. In addition to Halstead, Purdue University's Brown community cluster was used as well. The Brown cluster is powered by 551 compute nodes that each is composed of two 12-core Intel Xeon Gold "Sky Lake" processors. Each of these nodes have 24 cores in addition to 96 GB of RAM [30]. The Intel 17.0.1.132 compiler with the Intel MPI Library was used to build the SU2 code.

A test of scaling the code when running in parallel was performed in order to optimize the computational resources used for the different flow calculations. The primary grids used in this study were run through a series of performance tests to determine the optimal parallelization for each different calculation. The tests were set to run for ten iterations, and the tests started with a single core. Each subsequent test doubled the number of cores used, up to 256 cores.

The performance of the code across the different meshes was measured using three metrics. The metrics are speedup, s , parallel efficiency, e , and serial fraction, ϕ . These values, defined by

$$s = \frac{t_s}{t_p} \quad (2.16),$$

$$e = \frac{s}{p} \quad (2.17),$$

and

$$\varphi = \frac{\frac{1}{s} - \frac{1}{p}}{1 - \frac{1}{p}} \quad (2.18),$$

are a key way to determine if computing resources are being used with the most efficacy [31]. In these equations, t_s is defined as the time it takes for the program to run in serial, found by running the code on a single core. The variable t_p is defined as the time it takes for the program to run in parallel, which changes as the number of cores increases. The term p is the number of processors, or cores, in use.

Fig. 2.13 shows the speedup and parallel efficiency curves for the three 2D flat plate meshes. It can be seen all three meshes speed up reasonably well until around 64 cores. At this point, the coarse mesh plateaus, while the medium and fine meshes continuing speeding up, albeit marginally, to 128 cores. Further increasing the number of cores becomes less effective at that point, as the reduction in computation time becomes progressively smaller with additional cores. The coarse mesh is the fastest of the three calculations, but sees the least benefit from additional cores. Looking at the parallel efficiency, it becomes clear that there is a correlation between number of nodes and parallel performance of the grids. Once the parallel efficiency drops below 50%, almost no speed is gained for significantly larger cost, so the computational runs were limited to the number of cores that achieve this margin.

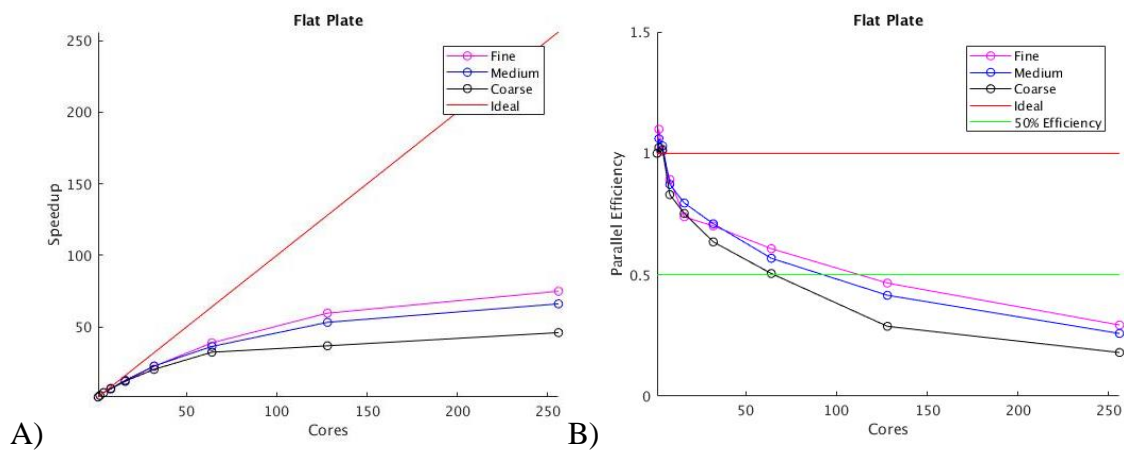


Fig. 2.13 Flat Plate Mesh A) Speedup, B) Efficiency

The 2D inlet isolators grids are overall smaller meshes, although they are much more dense on average than the flat plate grids. The speedup and parallel efficiency for these three grids are shown in Fig. 2.14. Again, the coarse grid converges fastest, but now only speeds up well up to 32 cores. The medium and fine grids' speedup begins flagging at around the 64 cores mark, shown by a leveling off in the speedup curve and a drop below the 50% line in parallel efficiency.

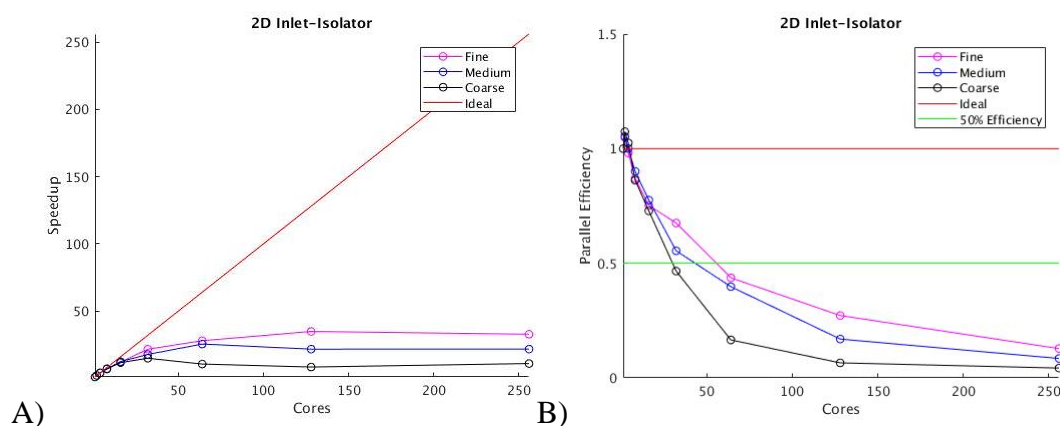


Fig. 2.14 2D Inlet-Isolator Mesh A) Speedup B) Efficiency

Finally, the 3D inlet-isolator mesh was tested in a scaling study for speedup across multiple cores. Note that due to the size of the mesh, this grid was tested up to 1000 cores, rather than stopping at 256 cores like the others. Fig. 2.15 shows the results, where the time per iteration is seen decrease to fairly well across multiple cores until 512 cores. Further increasing the parallelization after this point brings little gain, and actually marginally slows down at 1000 cores.

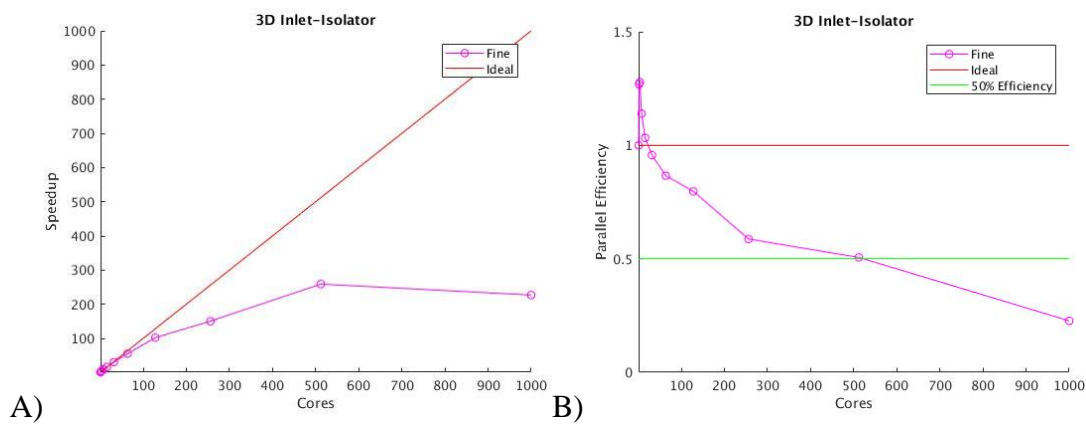


Fig. 2.15 3D Inlet-Isolator Mesh A) Speedup, B) Efficiency

The serial fractions across the three different mesh categories are shown below in Fig. 2.16. This is an assessment of how well the calculations are partitioned across multiple cores. For most of the meshes tested, the serial fraction is effectively constant, with the smallest grid (coarse 2D inlet-isolator) showing a large rise in serial factor, indicating a suboptimal parallelization. This is likely due to the fact that the small grid cannot be effectively distributed across the different cores efficiently. As with all these tests, the startup time was not included in this analysis, only the time per iteration once the system of equations was distributed across the various cores being used in each calculation.

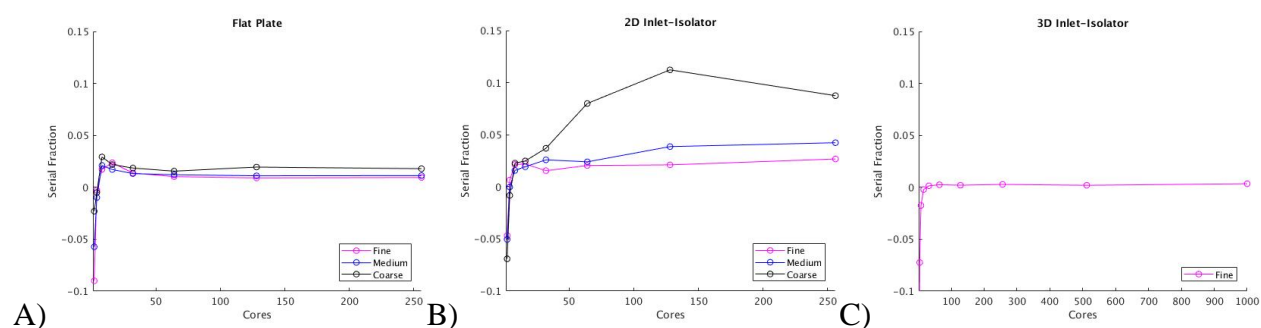


Fig. 2.16 Serial Fraction A) Flat Plate, B) 2D Inlet-Isolator, C) 3D Inlet-Isolator

There exists a minimum number of points per core for the three different mesh categories, assuming a minimum parallel efficiency of 50%. Interpolating allows an approximate intercept to be determined for each grid. For the 3D inlet-isolator grid, 50% parallel efficiency is at 522 cores. At 13,083,768 points, this means the optimal number of points per core is approximately 25,000 pts/core (approximately 30^3 pts/core). For the 2D inlet-isolator grids, 50% parallel efficiency is at 30, 43, and 55 cores for the coarse, medium, and fine grids. At 56,072, 123,228, and 248,912 points, this means the optimal number of points per core is approximately 1900, 2900, and 4500 pts/core. For the 2D flat plate grids, 50% parallel efficiency is at 65, 93, and 112 cores for the coarse, medium, and fine grids. At 197,376, 443,520, and 789,504 points, this means the optimal number of points per core is approximately 3000, 4500, and 7000 pts/core. As a rule of thumb, a minimum number of points per core to be used for similar 2D calculations on the tested clusters would be approximately 5000. For 3D calculations, a recommendation of a minimum of 20,000 points per core would be appropriate. The relatively poor parallel efficiency of the code could be due to the way MPI is set up on the clusters used for these calculations. In addition, it could be due to the

open-source nature of the SU2 program, which could make it less streamlined and parallelizable then would be ideal.

2.5 Source Term

The flap at the exit of the isolator was implemented virtually, using a source term to simulate an artificial body force. This method of disturbing the flow to induce unstart eliminated the need for a moving mesh, reducing the computational cost of the simulations dramatically. Atkinson et al. demonstrated the use of source terms to disturb flow, and the method used in this study is based on their work [32]. The source term was implemented as an ellipsoidal distribution in space. This spatial definition was defined as

$$g(x, y, z) = \frac{1}{K} e^{\left[-\left| \frac{x-x_c}{a} \right|^i - \left| \frac{y-y_c}{b} \right|^j - \left| \frac{z-z_c}{c} \right|^k \right]} \quad (2.19).$$

This equation is then scaled by

$$\int_{-\infty}^{\infty} \int_{-\infty}^{\infty} \int_{-\infty}^{\infty} g(x, y, z) dx dy dz = 1 \quad (2.20)$$

and

$$K = 8abc\Gamma\left(1 + \frac{1}{i}\right)\Gamma\left(1 + \frac{1}{j}\right)\Gamma\left(1 + \frac{1}{k}\right) \quad (2.21),$$

where $\Gamma(x)$ is the Euler gamma function [32].

In Eq. (2.19), the (x_c, y_c, z_c) are the coordinates of the source term's centroid. The exponents (i, j, k) were chosen to be $(2, 2, 2)$ for this study. Additionally, the denominators in Eq. (2.19), namely (a, b, c) , represent the chosen length scales along each respective axis. For this study, the length scales were $(2r, 0.5r, 2r)$, where $r = 10$ mm. Furthermore, this elliptical distribution was rotated by the flap angle, θ . The angle θ begins at 0 degrees and gradually changes to 26 degrees throughout the first 1 ms of the unstart flow simulation. This angle aligns with the streamwise axis of the source term distribution. Therefore, the final 2D and 3D source terms can be written as

$$g(x, y) = \frac{1}{\pi r^2} e^{\left[-\left(\frac{(x-x_c) \cos \theta + (y-y_c) \sin \theta}{2r} \right)^2 - \left(\frac{(x-x_c) \sin \theta - (y-y_c) \cos \theta}{\frac{1}{2}r} \right)^2 \right]} \quad (2.22)$$

and

$$g(x, y, z) = \frac{1}{(\sqrt{\pi}r)^3} e^{\left[-\left(\frac{(x-x_c) \cos \theta + (y-y_c) \sin \theta}{2r} \right)^2 - \left(\frac{(x-x_c) \sin \theta - (y-y_c) \cos \theta}{\frac{1}{2}r} \right)^2 - \left(\frac{z-z_c}{2r} \right)^2 \right]} \quad (2.23).$$

The use of an ellipsoidal spatial distribution of a source term to control a hypersonic flow was first developed to simulate plasma actuators [33] [34]. The scheme presented here, rotating the source term distribution in space, represents an extension of the source term method. It demonstrates its usefulness to simulate unstart and to represent a changing distribution that is more dynamic than a simple decay or expansion in time. As will be shown in the next sections of this paper, this method is foundational to effectively creating unstart in a CFD environment with minimal computational cost.

In order to verify that the source term was implemented properly, a computation with a source term driven force was completed. This calculation was done in both 2D and 3D, using the grids described in Section 2.3.4, with the angle θ chosen to be 0. The same freestream conditions were used for this computation as in all the other computations and the flow field was run to a steady-state convergence, with the source term implementing a force in the positive x, or downstream direction. The total force was measured at the inlet and outlet and a force balance was calculated using the momentum integral equation, shown by

$$F_q = \oint \rho V(V \cdot \hat{n})dA + \oint (P - P_a)\hat{n}dA \quad (2.24).$$

For testing in 2D and 3D, this equation can be simplified into the forms given by

$$F_{qx} = \left[\int_0^1 \rho u_x^2 dy + \int_0^1 P dy \right]_{in}^{ex} \quad (2.25)$$

and

$$F_{qx} = \left[\int_0^1 \int_0^1 \rho u_x^2 dydz + \int_0^1 \int_0^1 P dydz \right]_{in}^{ex} \quad (2.26).$$

The variable F_q is the force of the implemented source term and, in this test case, it was chosen to be 10 kN. In addition, *in* and *ex* indicate the inlet and exit planes at $x = 0$ and $x = 3$, respectively. The force balance yields a percent error of 1.0179% in 2D and 0.9947% in 3D. The temperature, pressure, Mach number, and density contours for the 2D test case are shown in Fig. 2.17. Note that density is the first conservative variable, so the legend is labeled “Conservative_1”, instead of “Density”. As previously mentioned, the source term calculations used the freestream conditions from experiment that will be used throughout this thesis, so there was a uniform Mach 4.9 inflow with a freestream temperature and pressure of $T_\infty = 56$ K and $P_\infty = 5.38$ kPa, respectively.

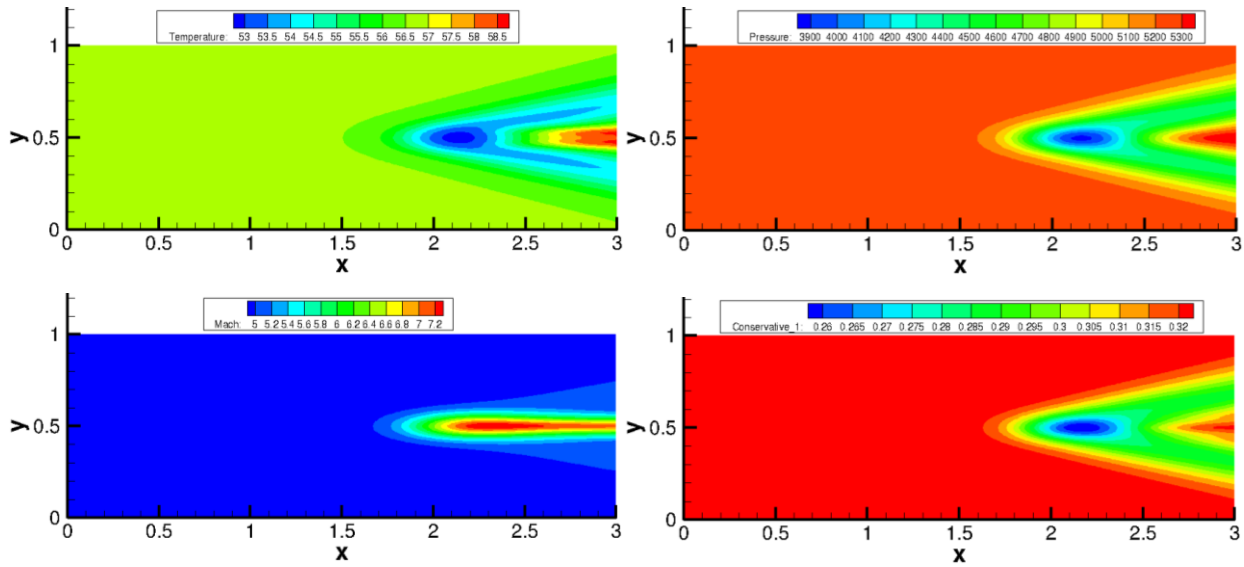


Fig. 2.17 2D Source Term Flow Field Countours

For the 3D test cases, the resultant corresponding flow contours are shown in Fig. 2.18. For these 3D flow fields, the slices shown are in the xy plane along the z centerline, in the xz plane along the y centerline, and at the outlet in the zy plane, located at $x = 3$. Taking the three slices of the source term test results, the oblate ellipsoidal geometry can be seen. As in 2D, the source term was situated in the channel center, in terms of y and z , and in the last third of the mesh, in x . This was done to ensure that the source term force balance remained unaffected by extraneous reflections from the mesh boundaries. It is important to reiterate that for all these tests, 2D and 3D, the direction of the source term force was in the direction of the flow, downstream, so it acted to increase Mach number and lower density, pressure, and temperature, at its location. In the inlet-isolator computations later in this investigation, the source term will be oriented differently, to simulate the flap in experiment. In addition, the strength of the source term will be difference in the inlet-isolator computations, to most accurately reflect the pressure disturbance from the flap in the experiments.

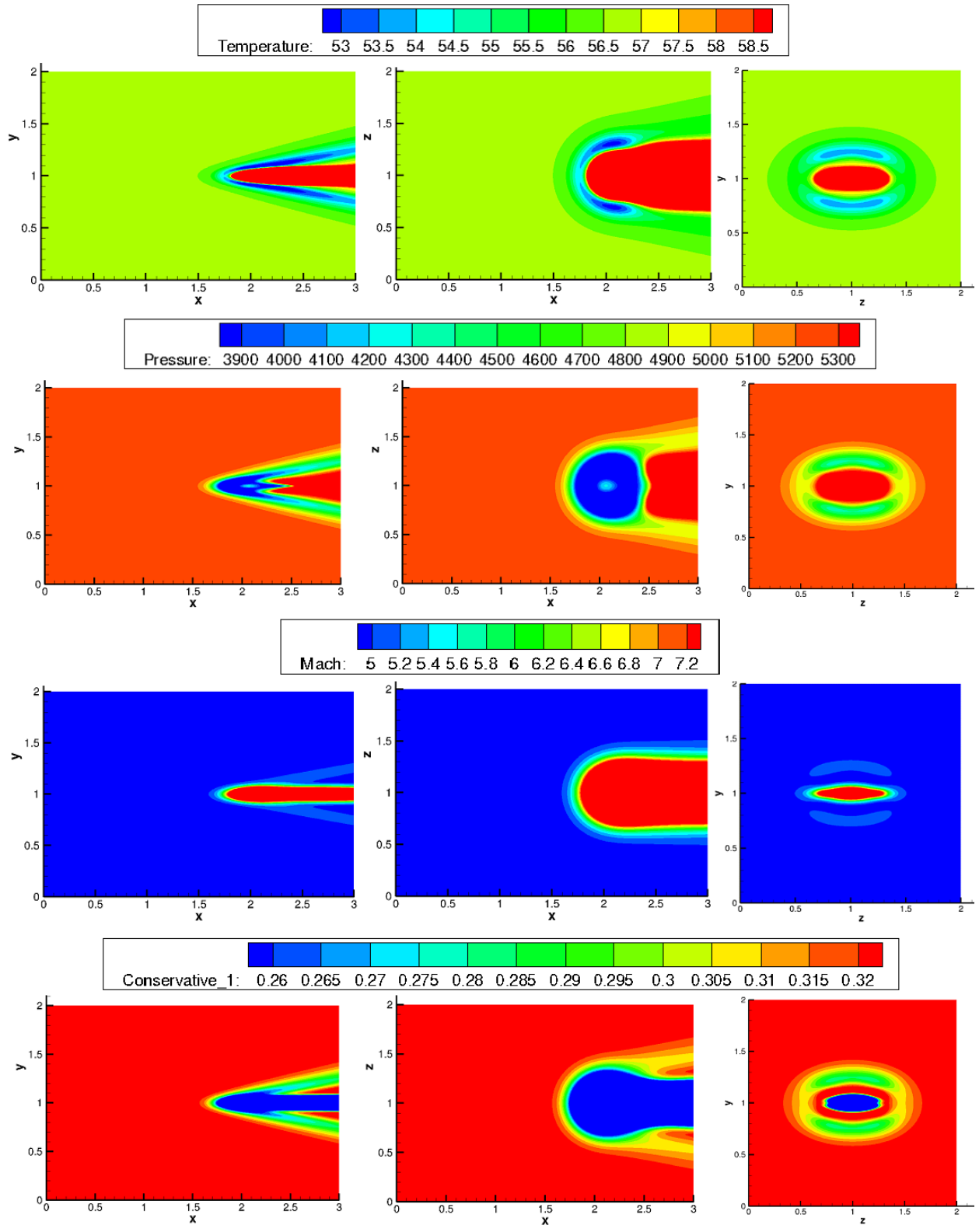


Fig. 2.18 3D Source Term Flow Field Countours (Z, Y, X Center Planes)

3. 2D COMPUTATION

The first step in exploring the dynamics of scramjet unstart is the development of a validated computational model. This chapter details the development of just such a model, initially limited to two dimensions. Computational results are compared across different meshes and to experiment for both the fully started flow configuration and through unstart. Convergence is verified and distinct flow features are identified. The dynamics of unstart are studied and a possible precursor signal to unstart is investigated.

3.1 Grid Convergence

The convergence to steady state of each flat plate boundary layer was determined based on the skin friction coefficient, C_f and wall pressure, P_w . First, the hypersonic flat plate boundary layer simulation was run on each mesh using the aforementioned flow conditions of a Mach 4.9 inlet with a freestream pressure of $P_\infty = 5.38$ kPa, and a freestream temperature of $T_\infty = 56$ K. The computations across the different meshes were run for a variable number of iterations based on how long it took the two aforementioned variables to converge. Each run for the coarse, medium, and fine meshes were was about 65,000, 550,000, and 1,000,000 iterations, respectively. Shown in Figs. 3.1 and 3.2, each of the three meshes took a progressively longer amount of time to converge, based on the size of the mesh, as expected.

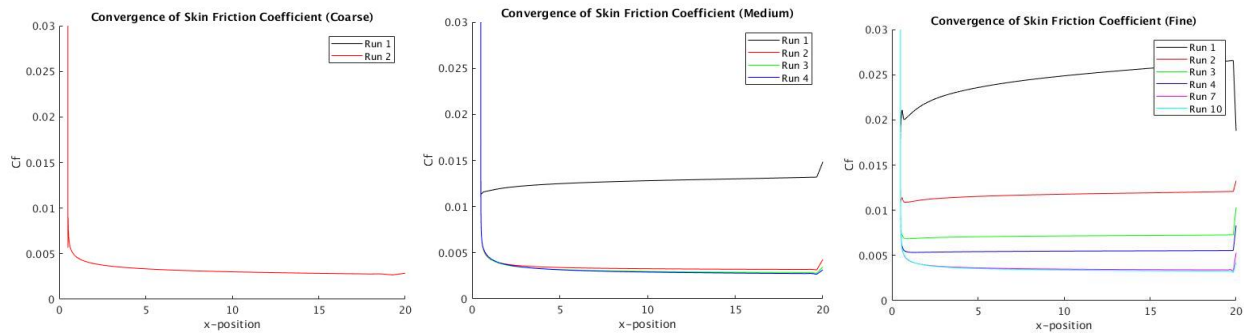


Fig. 3.1 Convergence of Flat Plate C_f (Coarse, Medium, and Fine Grids)

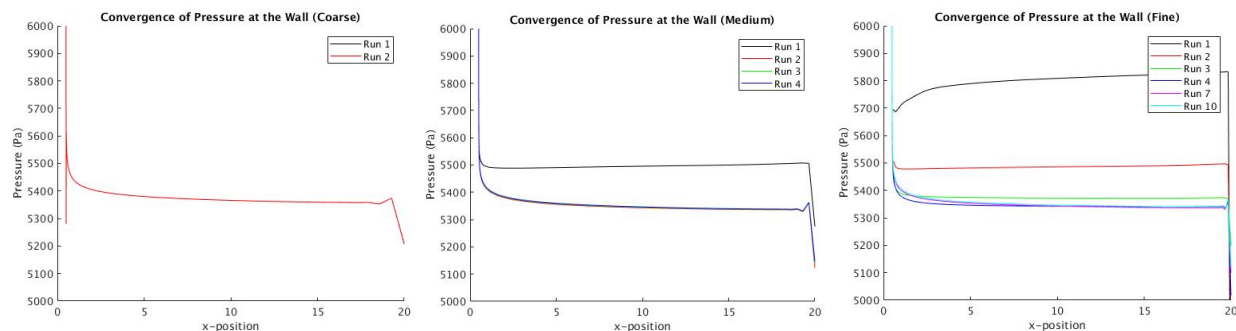


Fig. 3.2 Convergence of Flat Plate P (Coarse, Medium, and Fine Grids)

Fig. 3.1 shows this progressive convergence in terms of the skin friction coefficient across the different meshes, while Fig. 3.2 does the same in regard to pressure along the wall. To reiterate, the surface in question where these values are being measured is the flat plate, no-slip boundary on the meshes. The different meshes can be seen to converge, with the smaller meshes converging faster than their larger counterparts. In addition, the skin friction coefficient appears to converge a little slower than the wall pressure.

The total number of iterations to reach steady state was approximately 130,000 for the coarse mesh, 2,200,000 for the medium mesh, and 11,000,000 for the fine mesh. Once each mesh was determined to be individually converged, the solutions of each were compared to determine mesh independence of the solution. As can be seen in Fig. 3.3, there is a slight variation between the meshes, but all three meshes line up with each other reasonably well.

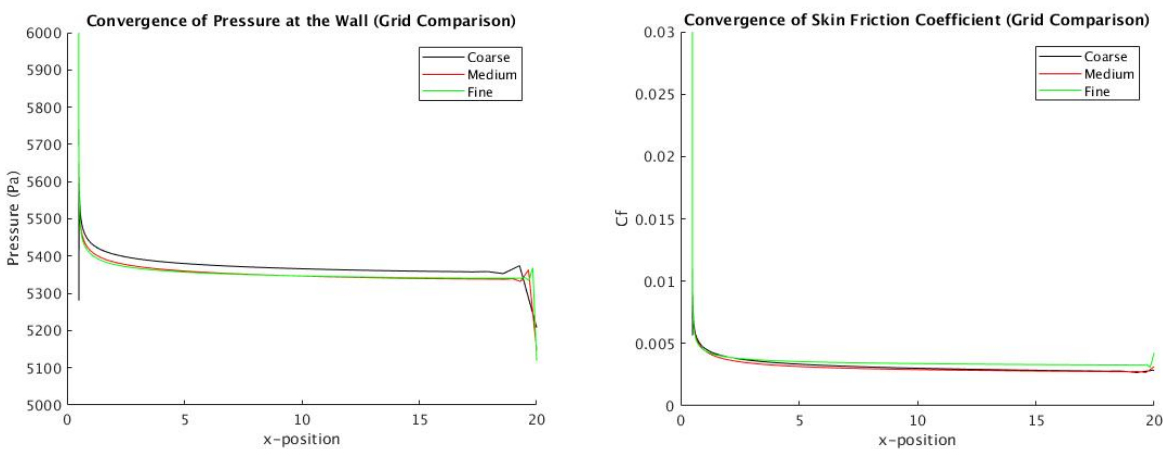


Fig. 3.3 Skin Friction Convergence Plots

To verify the overall accuracy of the solutions, the computational skin friction coefficients of the three meshes were compared with empirical correlations and theory. The computed values were first compared to the values predicted by the incompressible von Karman skin friction formula [35]. While this equation cannot predict the compressible values, it is a relatively simple approximation that should still be within an order of magnitude of the actual values, if not closer, providing an additional way to confirm whether the values found are realistic. This empirical formula, shown by

$$C_f = \frac{0.455}{\log_{10}(Re_\theta)^{2.58}} \quad (3.1),$$

works for Reynolds number values in the range from 10^6 to 10^9 , so should provide a reasonably close estimate for the Reynolds number range of found in this study (around 10^7). The analytical values were calculated using momentum thickness Reynolds number from the computations.

Fig. 3.4 shows a comparison of the skin friction coefficients from each of the three grids versus the values predicted by the Von Karman correlation. Starting at the slip transition point on the flat plate at $x = 0.5$ m, the values quickly converge and the computational values fairly closely with theory, although these incompressible values over predict the computational values. However, the skin friction coefficient is expected to be reduced when compressibility effects are taken into account with the next theoretical correlation.

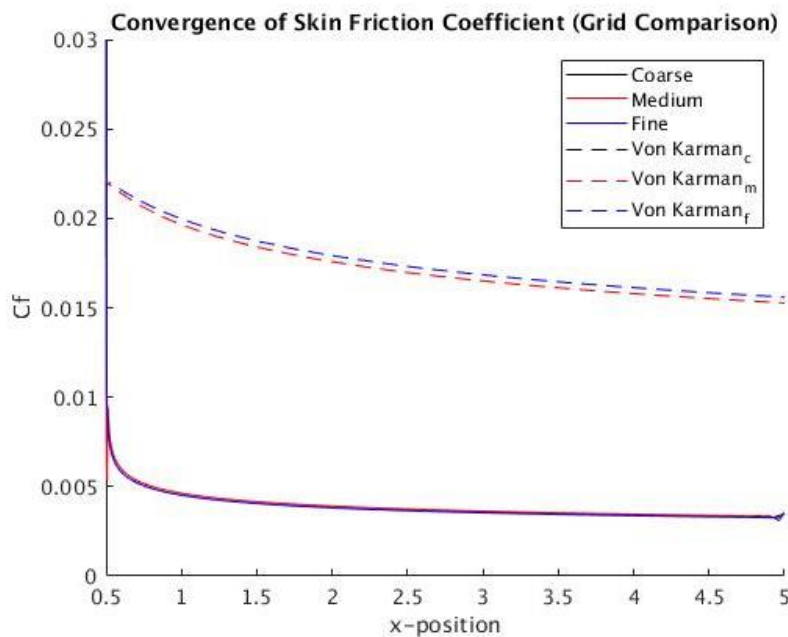


Fig. 3.4 Computational Skin Friction Values vs Von Karman

Next, the values were compared to the compressible Van Driest formulation [36]. The method to calculate the mean skin friction coefficient is given by

$$\frac{0.242}{A\sqrt{\overline{C_f}\frac{T_w}{T_\infty}}}(\sin^{-1}\alpha + \sin^{-1}\beta) = \log_{10}(Re_\theta\overline{C_f}) - \frac{1+2\omega}{2}\log_{10}\left(\frac{T_w}{T_\infty}\right) \quad (3.2).$$

In addition, the terms in the Van Driest formulation are defined by

$$\alpha = \frac{2A^2 - B}{\sqrt{B^2 + 4A^2}} \quad (3.3),$$

$$\beta = \frac{B}{\sqrt{B^2 + 4A^2}} \quad (3.4),$$

$$A^2 = \frac{\frac{\gamma-1}{2}M_\infty^2}{\frac{T_w}{T_\infty}} \quad (3.5),$$

and

$$B = \frac{1 + \frac{\gamma-1}{2}M_\infty^2}{\frac{T_w}{T_\infty}} - 1 \quad (3.6).$$

Finally,

$$C_f = \frac{\frac{0.558}{A}(\sin^{-1}\alpha + \sin^{-1}\beta)\overline{C_f}}{\frac{0.558}{A}(\sin^{-1}\alpha + \sin^{-1}\beta) + 2\sqrt{\overline{C_f}\frac{T_w}{T_\infty}}} \quad (3.7)$$

is used to calculate the local skin friction coefficient. In these equations, T_w and T_∞ are the temperature at the wall and in the freestream, respectively. Eq. (3.2) can be solved iteratively using Newton's method, using the wall temperature values from the computation. The value used for ω is 0.76, as found by Van Driest [36].

Solving for the Van Driest skin friction coefficient shows a closer match to the values given by the computations, although theory still over predicts the computational values a bit. Fig. 3.5 plots a comparison of the Van Driest predicted skin friction coefficients with the computational solutions from the three different grids. As expected, the compressible theory predicts lower values of skin friction along the flat plate than the comparable incompressible theory results. From the two plots, the computations were determined to be both fully converged and validated. While both Von Karman and Van Driest over predict the values in the computations, they both match very closely with the computed values and the compressible theory matches much better. The theoretical values match sufficiently well to give confidence moving forward.

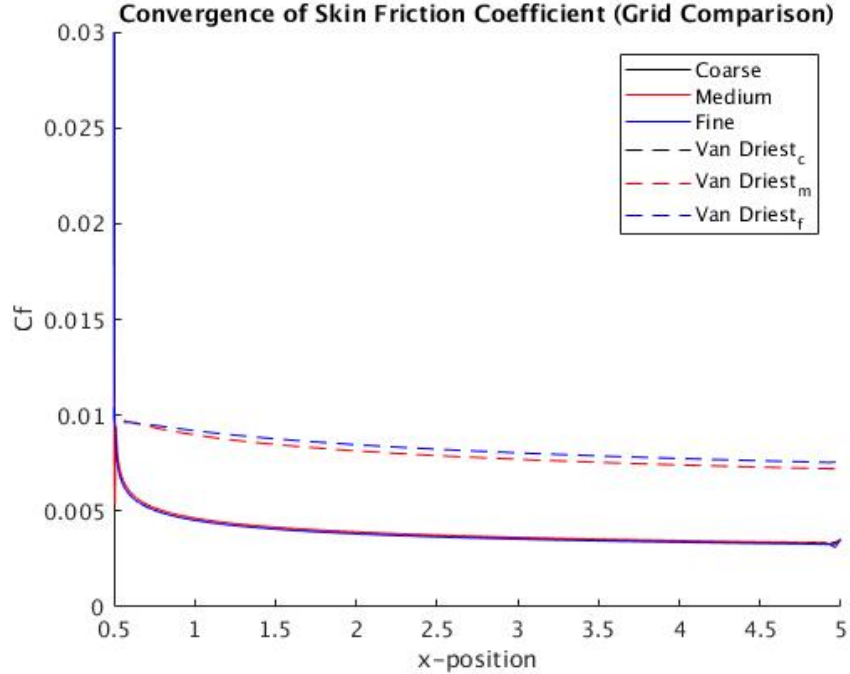


Fig. 3.5 Skin Friction vs Van Driest

3.2 Grid Independence Study

The flow fields from the coarse, medium, and fine meshes were compared to verify whether the solution was grid independent. The grid refinement study was completed in accordance with the methods described by Roache [37] [38]. First, a Richardson extrapolation was used, as defined by

$$f_{exact} = f_1 + \frac{(f_1 - f_2)}{(\varepsilon^\zeta - 1)} \quad (3.8)$$

The variable f represents the quantity being studied, in this case either skin friction or wall pressure. The subscripts 1, 2, and 3 represent the different grids, from most fine to most coarse. Variables ε and ζ are the grid refinement ratio and order of convergence, respectively. This study used a grid refinement value about 1.4, and a ζ value as calculated by

$$\zeta = \frac{\ln\left(\frac{f_3 - f_2}{f_2 - f_1}\right)}{\ln(\varepsilon)} \quad (3.9).$$

Note that this method of calculating ζ applies only because the grid refinement ratio between the coarse, medium, and fine grids is the same.

To determine the accuracy of the predicted value, the grid convergence index must be calculated. This value can be calculated for different grids, as shown by

$$GCI_{12} = 1.25 \left| \frac{f_2 - f_1}{1 - \varepsilon^\zeta} \right| \quad (3.10)$$

and

$$GCI_{23} = 1.25 \left| \frac{\varepsilon^\zeta (f_2 - f_1)}{1 - \varepsilon^\zeta} \right| \quad (3.11),$$

and represents an error estimate for the grid comparison. Finally,

$$1 \cong \varepsilon^\zeta \frac{GCI_{23}}{GCI_{12}} \quad (3.12)$$

is used to verify that the calculated values are within the asymptotic range of convergence, which is a check for the accuracy of the error estimate.

The predicted Richardson extrapolation value for the skin friction coefficient, is $C_{f\text{-exact}} = 0.0032648$ with an expected error of 0.066572%, based on the two finest grids. The error estimate falls within the asymptotic range of convergence, with an asymptotic values near one and equaling 0.96379, so it should be accurate. In addition, the Richardson extrapolated pressure was calculated at the target location of the boundary layer. This station is where the boundary layer thickness is 19.3 mm. At this location, $P_{\text{exact}} = 5412.8$ Pa, with an expected error of 0.32290%. Similarly, this solution is also within the asymptotic range of convergence with an asymptotic value near one, at 0.99781. The order of convergence for these calculations came out to about $\zeta = 1.7$.

3.3 Boundary Layer Development

Matching the thick boundary layer was a first step towards the goal of recreating the observed experimental phenomena in a computational environment. The coarse, medium, and fine flat plate grids described in Section 2.3.1 were used to develop this boundary layer. The freestream conditions are also detailed in Section 2.1. The three fully converged flat plate solutions are shown in Fig. 3.6, with the left hand image showing the streamwise mass flux (ρu) and the right hand image showing the pressure contour. The difference in pressure in each mesh is easier to discern qualitatively, but slight variations in the solution sets for each mesh are present. From the flow contours, the clearest difference between the plots can be seen in the slight change in the angle of the oblique shock, initiated from the leading edge of the flat plate, modeled by the slip to no-slip transition point along the bottom boundary of the mesh.

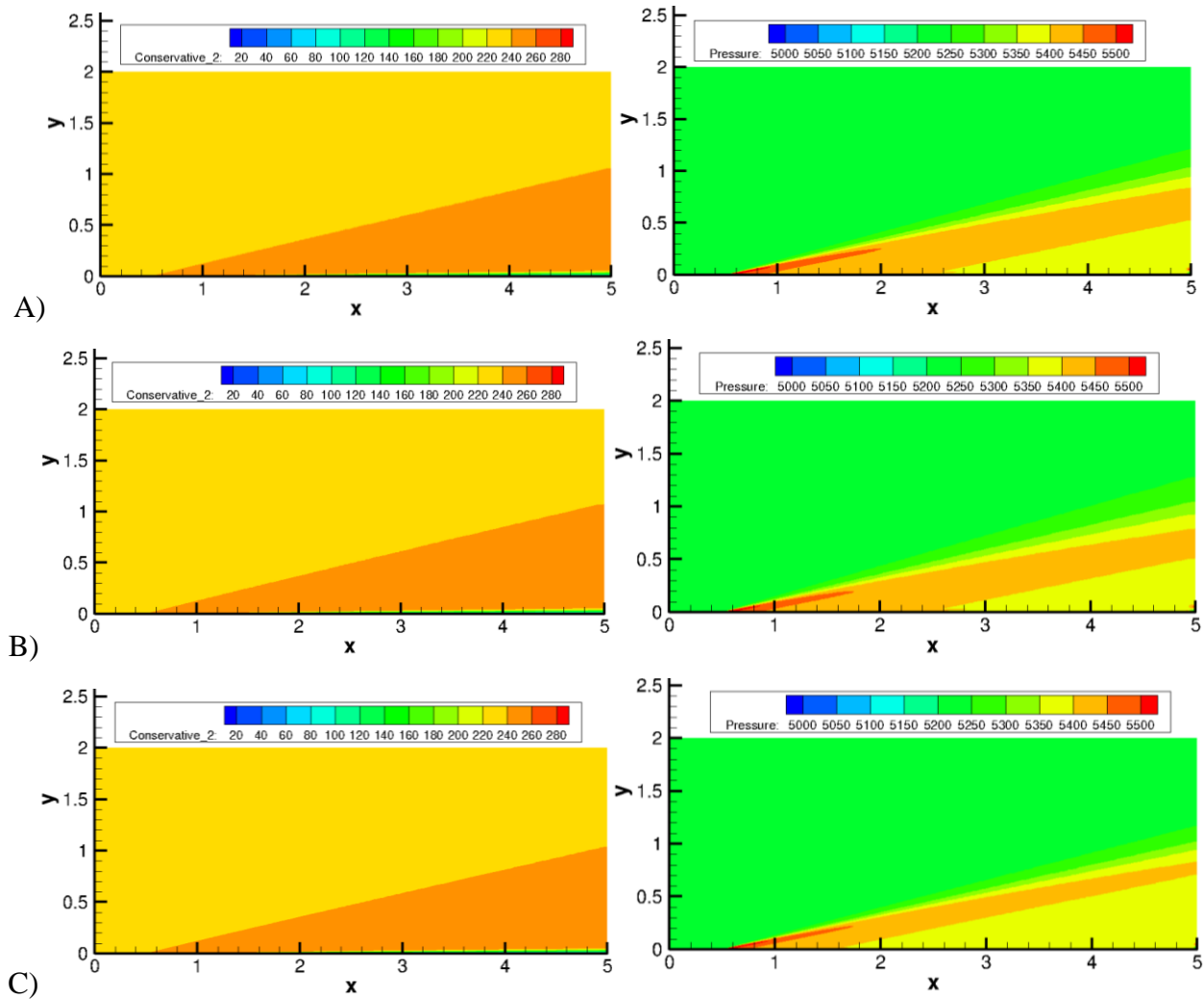


Fig. 3.6 Converged Flat Plate Solutions A) Coarse, B) Medium, C) Fine

The boundary layer thickness, δ , used in this study is defined as the height, or y-coordinate, where $u(y) = 0.99u_\infty$. Targeting a boundary layer thickness of 19.3 mm, the above flow fields can be used in to pick out the location of the desired boundary layer thickness. Fig. 3.7 shows the u velocity as a function of height above the flat plate for the three grids, at the x location where u at a height of $y = 19.3\text{mm}$ is $0.99u_\infty$. With the given definition of the boundary layer thickness, this streamwise velocity can be used as an analog for the boundary layer thickness. The x location where the desired boundary layer occurs is at $x = 2.2$ m, when the flow has traveled along approximately 1.7 m of the flat plate.

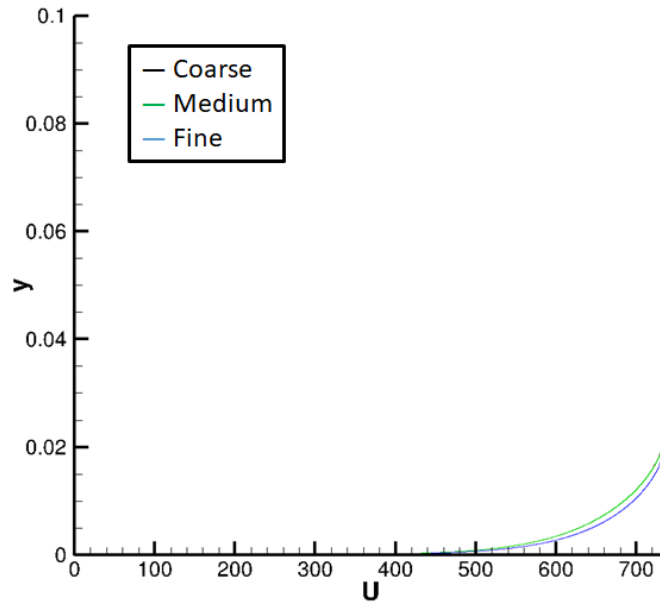


Fig. 3.7 Flat Plate Streamwise Velocity Near Wall for 3 Grids, at $x = 2.2$ m

3.4 Fully Started Flow

The three boundary layers developed in the previous section were imposed at the inlet of the 2D inlet-isolator meshes described in Section 2.3.2. The coarse, medium, and fine grids were run until they reached a converged steady state solution. For the geometry and freestream conditions studied here, the steady state solution was an internal shock system showing a fully started hypersonic flow. The floor boundary layer has been completely ingested by the inlet-isolator along with the Mach 4.9 freestream flow and a standing shock train develops.

The computational results were post-processed to create a pseudo-Schlieren image, shown in Fig. 3.8, where the x and y coordinates are normalized by the height of the isolator. In it, four oblique shocks can be seen, along with the boundary layer, and are labeled 0, 1, 2, and 3. It should be noted that the boundary layer thickens at each impingement point where the shock reflects off the wall and creates an expansion fan. The thick floor boundary layer can be seen entering the inlet, with a much thinner ceiling boundary layer developing through the test section. The shockwave boundary layer interaction at these points will be particularly important in the unstart process.

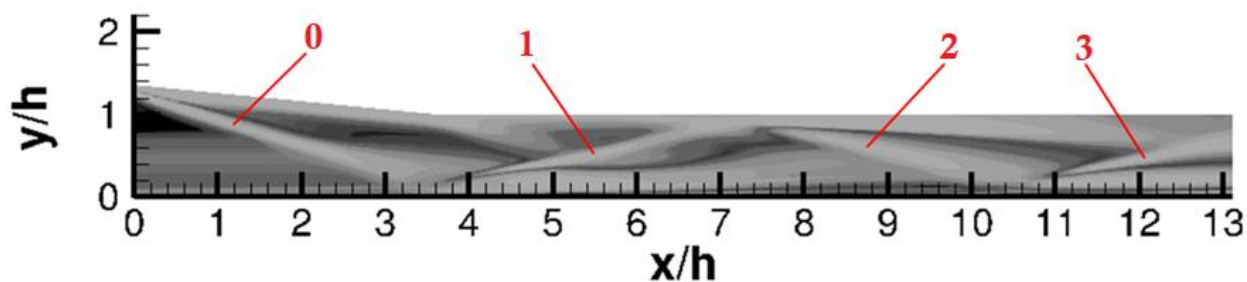


Fig. 3.8 2D Pseudo-Schlieren Image (Density Gradient Magnitude) of Fully Started Flow

The oblique shock angles and impingement points for each of the four shocks contained within the inlet-isolator mesh match what was found in experiment [19]. The experimental fully started flow documented by Wagner is reproduced in Fig. 3.9. In this experiment, only 3 of the four shocks (labeled 1, 2, and 3) can be seen in the view window, but the first (or “zeroth”) shock can be inferred from the location of shock 1.

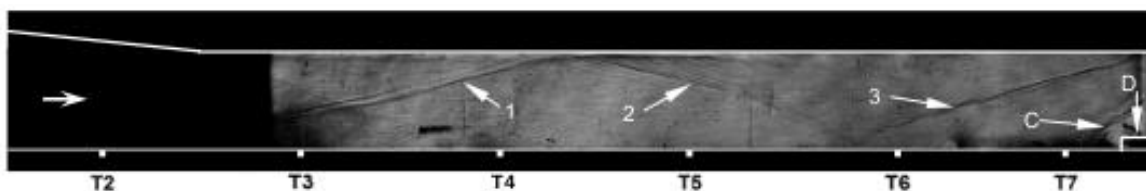


Fig. 3.9 Schlieren Image of Fully Started Supersonic Flow, used with permission [19]

Wagner measured the pressure in the channel along the bottom wall at the six locations labeled T2-T7 (T1 measured the freestream pressure). The fully started flow wall pressure was also extracted from the computational results and is compared to the experimental values. Fig. 3.10 presents a comparison of the wall pressure from the three computational runs, alongside the experimental values. The pressure has been normalized by the freestream pressure and it can be seen that the pressure trends within the inlet-isolator match closely between the experiments and computations. In addition, there is little variation between the three tested meshes of different resolutions, indicating stability of the solution, and the finest mesh predicts the most accurate result.

The pressure along the bottom wall sees a jump of approximately 3.5 times the freestream pressure when the flow passes through a shock impingement point on the bottom wall. The

pressure along the channel floor drops after each jump and falls back to roughly the freestream pressure until another shock impingement point causes the pressure to spike again.

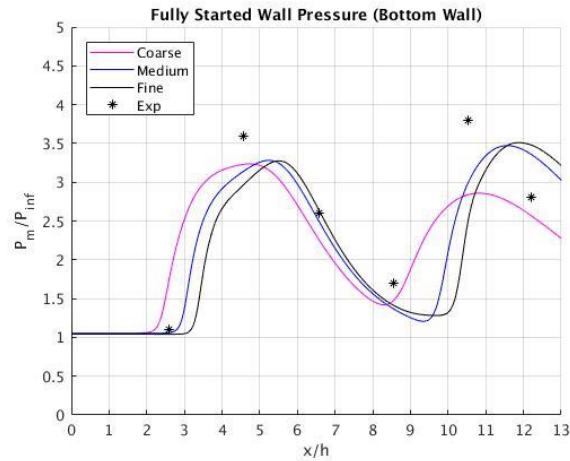


Fig. 3.10 Normalized Wall Pressure of 2D Fully Started Flow on Channel Floor

A similar trend can be seen in the computational results on the channel ceiling, shown in Fig. 3.11. The experiments had no pressure transducers along the top wall, but the results from the computations match expectations and appear to converge with grid refinement like their counterparts on the channel floor. The changes in pressure appear to follow roughly the same trends and be of the same order of magnitude on both the top and bottom walls of the channel. It can be seen that the coarse mesh predicts the location of the peak pressure slightly off, but the two finest meshes agree well with each other.

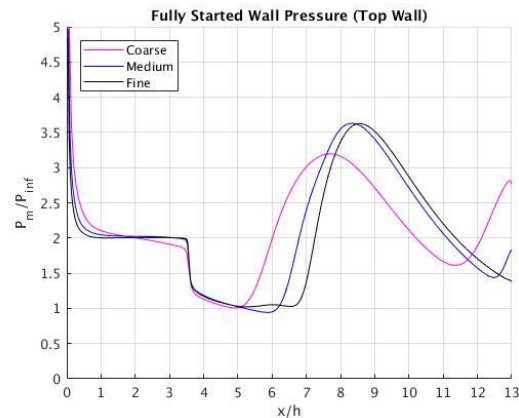


Fig. 3.11 Normalized Wall Pressure of 2D Fully Started Flow on Channel Ceiling

Examining the channel pressure in more detail, it can be seen that there are regions of high and low pressure in the vicinity of the oblique shocks. Fig. 3.12 shows the pressure flow fields for the 3 different grids. The pressure in the whole channel jumps to roughly two times the freestream pressure as soon as it passes through the first (zeroth) shock. On the rebound, at around $x/h = 3$, there are high and low pressure regions created by the shock on the bottom and top walls, respectively. The low pressure region at the top surface is still upstream of the shock whereas the high pressure region is directly downstream of the shock. This high-low pressure variation around each shock continues down the channel, and is what would be expected from the oblique shock train.

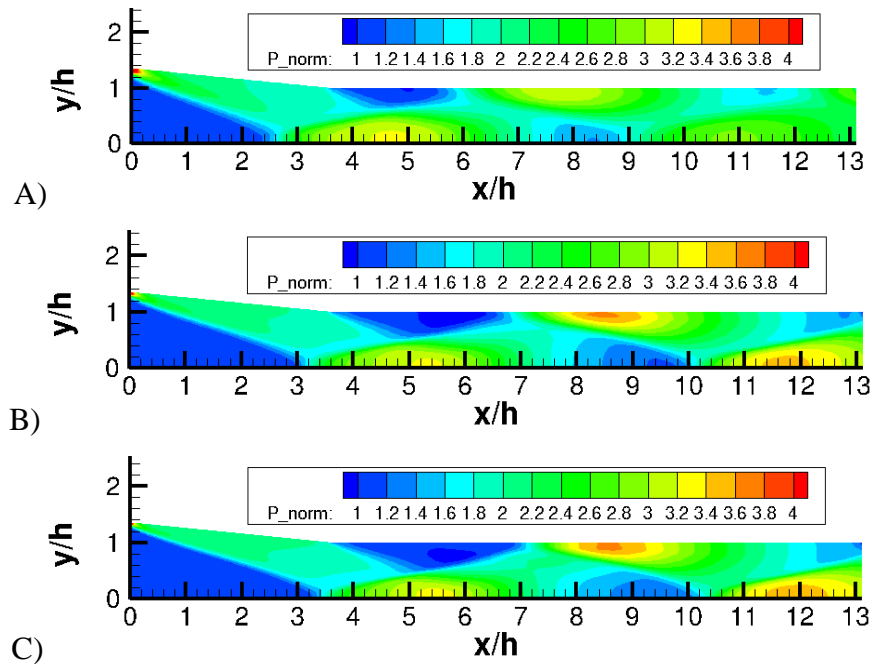


Fig. 3.12 Normalized 2D Fully Started Flow Pressure A) Coarse, B) Medium, C) Fine

Further validation of the computational accuracy is found in the Particle Image Velocimetry (PIV) measurements made by Wagner [20]. A contour of v (y -velocity), u (x -velocity), and M (Mach number) was created from the fully started flow. A side-by-side comparison of these PIV images with computational results is shown in Fig. 3.13. The computational results are from the fine grid and match well with experiment. The extremely thick boundary layer present on the floor of the channel can be seen here, evidenced by the large, low-speed region in the u and M plots.

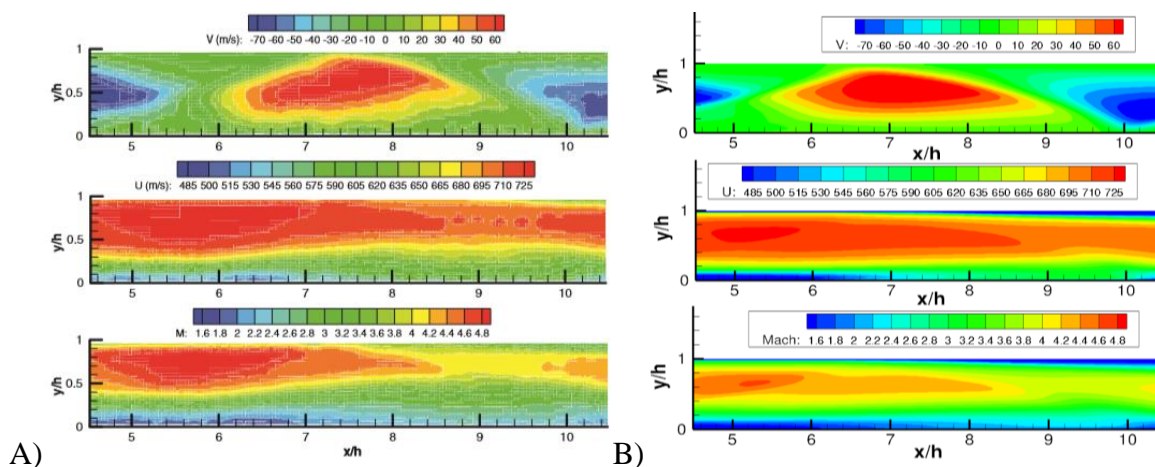


Fig. 3.13 A) Experimental PIV, used with permission [20], B) 2D Velocity Field

A major benefit of the computational results is the ability to see the entire flow, rather than be limited by a view window. Zooming out on the fine grid to see the full inlet-isolator channel, the larger flow structures become more apparent. Fig. 3.14 shows the u , v , and M for the entire channel. The flow remains supersonic throughout the entire channel, except for within the boundary layers on the top and bottom, which are subsonic. However, the core flow slows down considerably as it progresses downstream through the four oblique shocks in the shock train, going from around Mach 5 to approximately Mach 3.

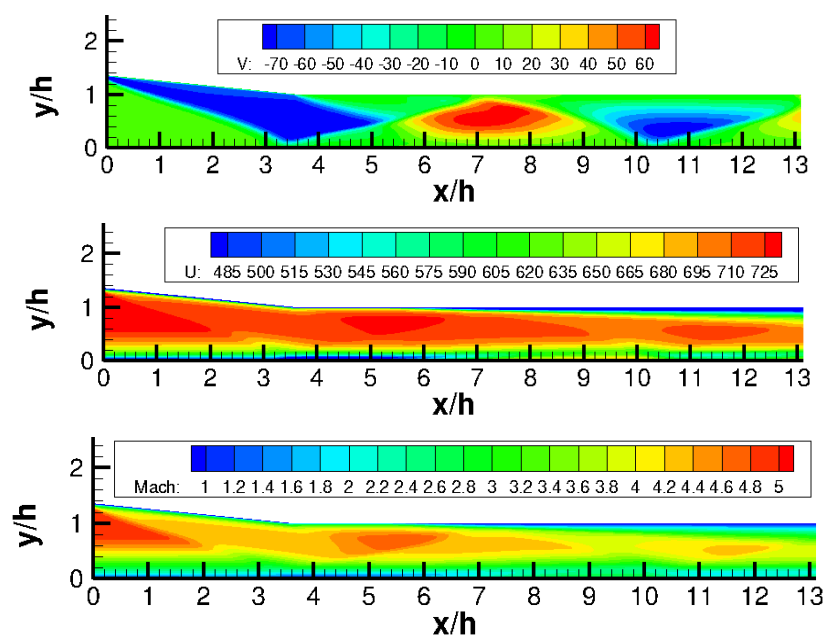


Fig. 3.14 Velocity Field of 2D of Full Inlet-Isolator

3.5 Unstart

With the fully started flow computational results matching experiment, and with grid independence confirmed, the next step was to investigate unstart. For this work, only the finest mesh was used. Starting from the steady state of the fully started flow solution, the elliptical source term was initiated, simulating raising the flap in experiment. This causes a disruption that, in turn, triggers a shock which travels upstream from the location of the flap at the isolator exit. The source term was located at the same position as the flap used in the University of Texas, Austin experiments. Within the computations, this meant it was centered at $x = 328$ mm and $y = 10$ mm.

A number of different force strengths were tried for the source term to initiate unstart. By studying the flow for different magnitudes of the force, it was determined that 1 kN was the ideal magnitude to initiate unstart in the 2D case. For values much larger than that, unstart would occur too quickly and provide an unrealistic simulation of the ramp. Alternatively, a smaller magnitude would not disrupt the flow enough and the system would not unstart. This tuning of the source term was done to ensure that the source term matched the flap's disruption as accurately as possible.

Pseudo-Schlieren imaging was used to analyze the computational flow and compare to experiment. Fig. 3.15 shows a side-by-side experimental to computational comparison of the propagation of unstart. The axes are normalized by the height of the isolator. A blue dotted line highlights the area of the computational images that can be seen in the field of view of the experiment. This is the region that can be used to assess the validity of the computations, but the entire flow field behavior within the inlet-isolator warrants study and discussion, so is included.

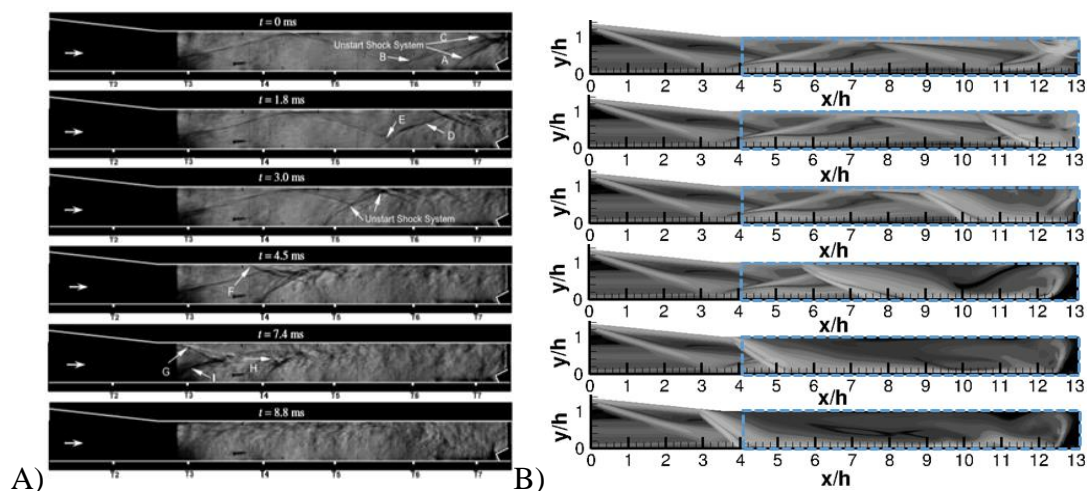


Fig. 3.15 Unstart A) Schlieren Images used with permission [19], B) 2D Pseudo-Schlieren

As can be seen in Fig. 3.15, the unstart flow field simulated in the computational domain matches closely with that of the experiment. As unstart progresses upstream towards the inlet, the standing shock train from the fully started flow remains in place until disturbed by the stronger shock from unstart. Over several milliseconds, this shock train is disrupted by the angled unstart shock. The angle of this shock appears to be dependent on the angle of flap deployment, with the shock running roughly perpendicular to the flap.

Looking at the computational results in more depth, the pressure change within the channel helps elucidate the flow behavior. The time sequence depicting unstart is shown in Fig. 3.16, normalized by the freestream pressure. As the virtual flap is raised, the unstart process begins. In the region of the flap, at the isolator exit, a pressure rise can be seen and the flow becomes choked. This pressure rise is on the order of eight to ten times higher than the freestream pressure, much larger than the pressure variations that exist within the started region of the flow, which measure one to three times the freestream pressure.

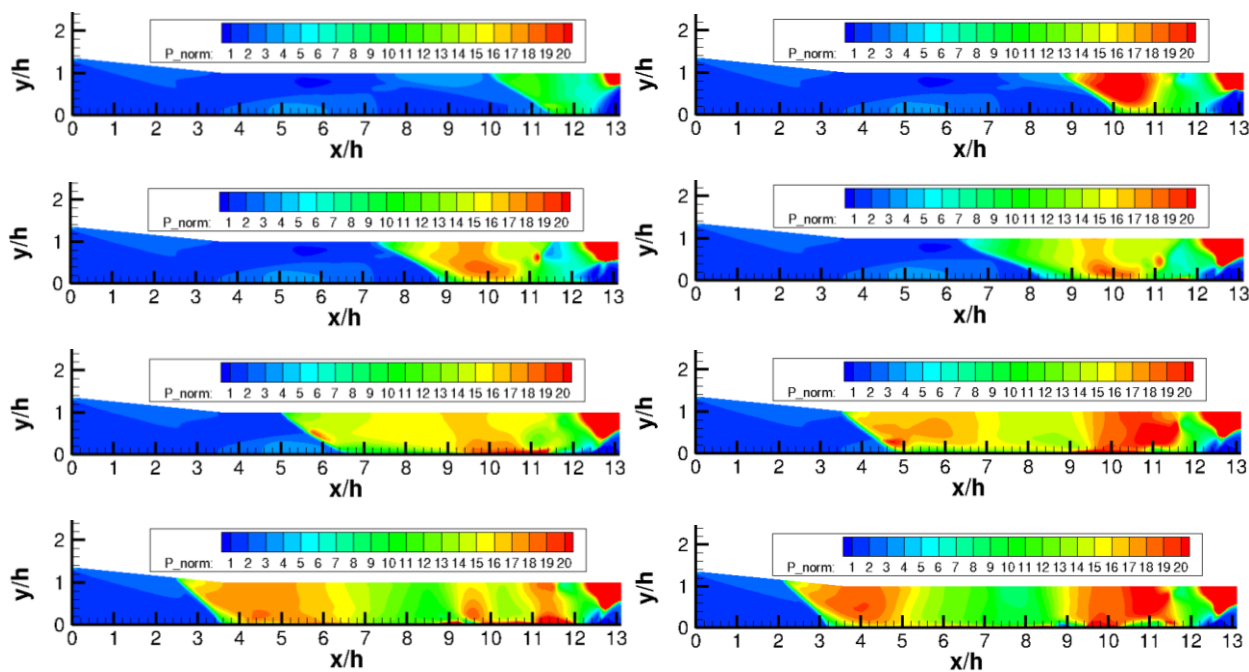


Fig. 3.16 2D Unstart Pressure at $t = [0.25, 0.50, 0.75, \dots, 2.00]$ ms

As the unstart region propagates upstream, the high pressure bubble interacts with the portions of the flow that have higher than freestream pressure. These areas have a thicker boundary layer and the interactions between the boundary layer and the unstart shock produce large jumps

in the pressure in their vicinity. These pressure spikes of up to 30 times the freestream pressure are highly transient and continue downstream, opposite the direction of unstart. As they flow downstream, the pressure falls back down around eight to ten times the freestream pressure. This creates a pulsing phenomenon with pressures.

The shock from unstart travels at a constant rate within the constant-area isolator. However, once it reaches the inlet, after traveling upstream through the isolator, the flow changes. Unstart slows as the cross-sectional area of the model opens up due to the inlet ramp. This is also the location of the thickest boundary layer along the floor. Up until this point, the high pressure unstart region traveled at a high angle, furthest upstream near the channel ceiling. However, with the ceiling now angled and the flow staying the same, the shockwave begins to curve. This can be seen in Fig. 3.17, which shows the final steps of the unstart pressure variations. As this curved shock front forms, a large spike in the pressure, downstream of the shock, can be seen. Unlike the previous pressure pulses, this pressure rise is sustained and propagates through the entire unstart region until the whole channel is at the elevated pressure.

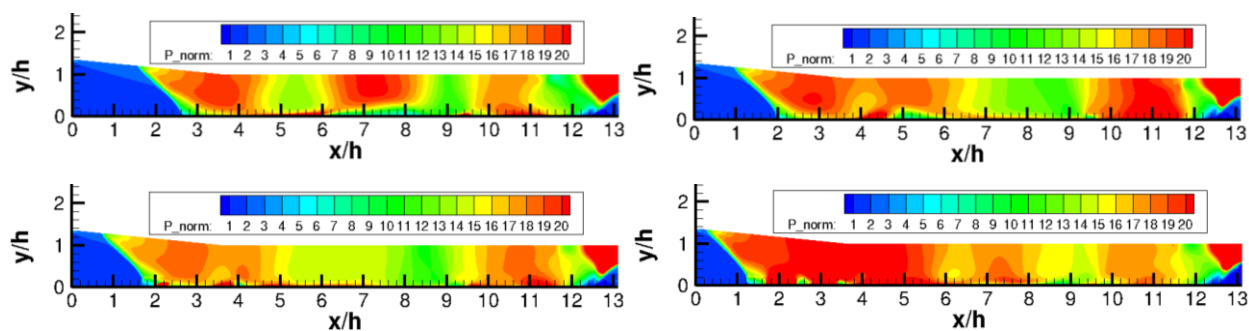


Fig. 3.17 2D Unstart Pressure at $t = [2.25, 2.50, 2.75, 3.00]$ ms

An important addendum is that unstart is occurring at a speed in the computational domain that is approximately twice that observed in experiments. However, all relevant phenomena exhibit the same characteristics. In the experiment, the unstart speed was the measured time it took for the leading edge of the unstart shock to travel between two pressure transducers. For the computations, the leading edge of the unstart shock on the top and bottom walls of the channel was determined based on the local wall pressure. Regions of normalized pressure greater than or equal to five were considered to be downstream of the unstart shock. Normalized by the freestream velocity, unstart in the physical experiments had a mean velocity of 0.0625, measured by pressure transducers along

the bottom wall [18]. In this 2D computation, the mean unstart speed, normalized by the freestream velocity, was 0.1252 along the top wall and 0.1292 along the bottom wall. Fig. 3.18 shows the normalized unstart speed at different points in the channel, as compared to the available experimental data. Looking at the unstart velocity gives a clearer view of its dynamic nature. Fig. 3.18 also plots the same computational unstart velocity against time rather than position within the channel. The speed is relatively constant for most of the unstart process, until around the time when the unstart shock reaches the inlet ramp. Here, the unstart along the ceiling slows dramatically before speeding up again to the mean velocity.

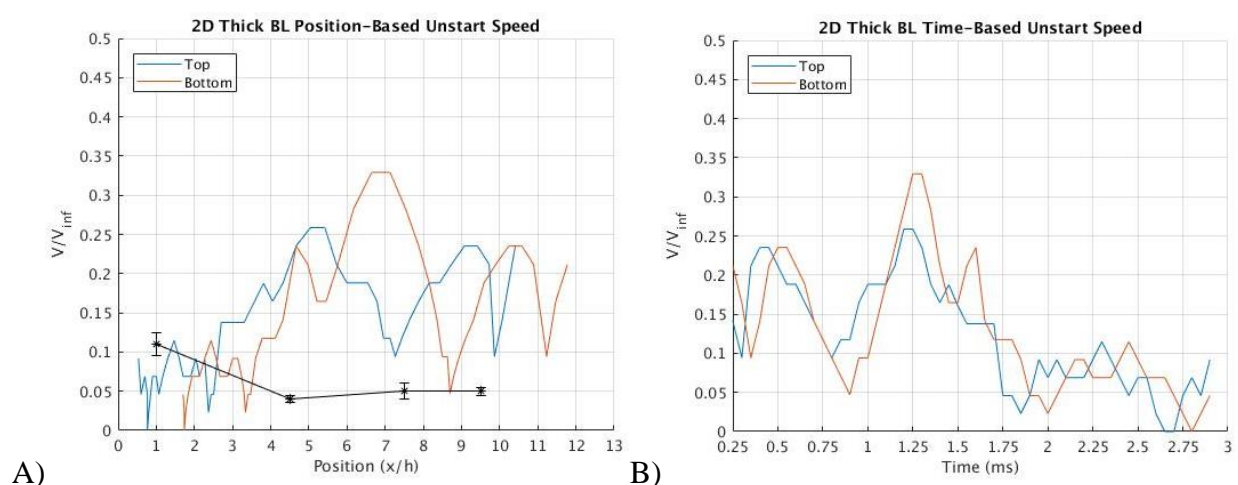


Fig. 3.18 Unstart Speed through 2D Inlet-Isolator vs A) Position, B) Time

Looking at the unstart shock arrival time, shown in Fig. 3.19, gives a clearer trend of how unstart progresses upstream from the isolator exit to the start of the inlet. Although there is significant variation from timestep to timestep, the overall trend of unstart progression is fairly stable. In this 2D case, the leading edge of the unstart shock begins on the channel floor and ceiling almost simultaneously. The two lines in the figure below are almost parallel, meaning that the shape of the shock stays relatively constant. The curvature seen towards the end of unstart, near the inlet entrance, can be seen by the distance between the two lines decreasing near $t = 2.5$ ms. In addition, there is a slight divergence between the two lines near $x/h = 1$, where the unstart shock leading edge along the bottom walls lags behind that along the top wall. Soon after, however, the bottom wall catches back up and the angle of the shock leading edge returns to its initial angle.

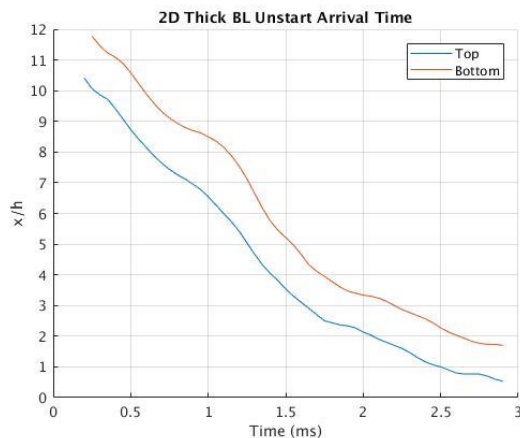


Fig. 3.19 Unstart Shock Arrival Time in 2D Inlet-Isolator

Examining the Mach number within the channel reveals a similar process to that seen with pressure. Fig. 3.20 shows the change in subsonic Mach number of the flow during the unstart process. Similar to the pulses of pressure, pulses of Mach number regions can be seen as unstart reaches each shock impingement point. These pulses are marked by bubbles of supersonic Mach number developing and dissipating as they travel downstream, opposite the unstart direction.

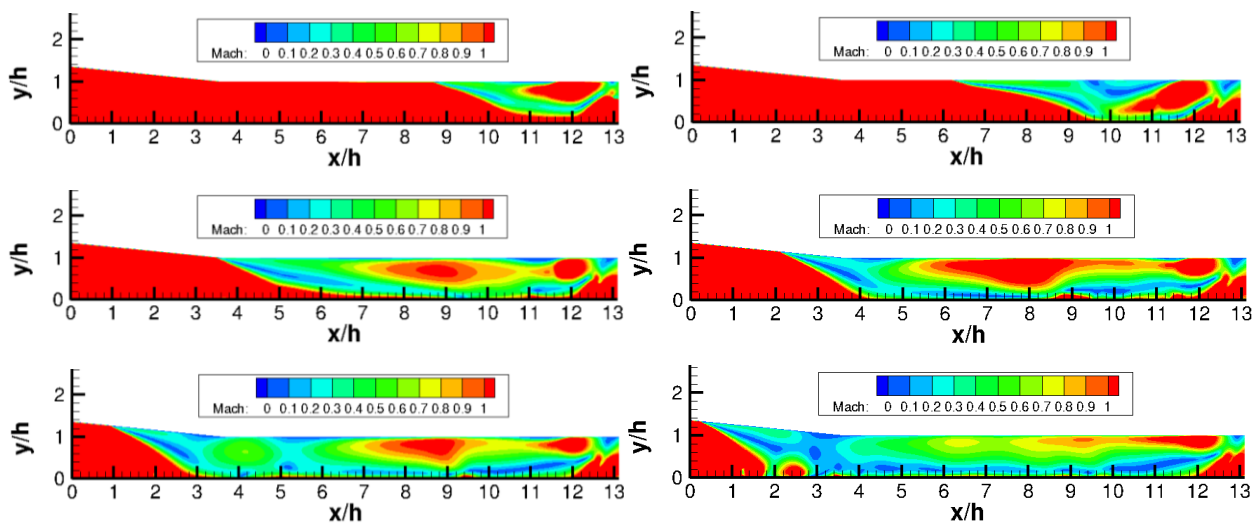


Fig. 3.20 2D Regions of Subsonic Flow during Unstart at $t = [0.5, 1.0, 1.5, \dots, 3.0]$ ms

3.6 Unstart Precursors

Qualitatively, it appears that the flow within the inlet-isolator section remains steady until the unstart region reaches it. This makes sense, given that the flow is supersonic and features a

number of oblique shocks, so information should not be able to travel upstream. However, a more in-depth study was conducted to see if any potential downstream information regarding unstart was present in the boundary layer. Because the boundary layers are subsonic near the wall, a region exists that can potentially pass information upstream. In particular, wall pressure was evaluated along the top and bottom walls of the channel.

If the pressure within the boundary layer, or wall pressure, sees a change prior to the unstart shock front reaching it, it could be indicative of an unstart precursor. To this end, the normalized pressures within the inlet-isolator channel are plotted in Fig. 3.21. Underneath each pressure plot is a trace of the wall pressure, along the top and bottom walls of the channel, at the same time step. During unstart, it can be seen that the wall pressure observed on channel ceiling is relatively stable compared to that of the floor. In fact, once the unstart shock passes a particular coordinate, the pressure stabilizes to roughly 20 times the freestream pressure. This matches with values seen by Wagner et al. [19]. Alternatively, the channel floor experiences a significantly larger pressure, varying from 50 to 90 times the freestream pressure. It appears that the thick floor boundary layer is tied to a much stronger local unstart pressure.

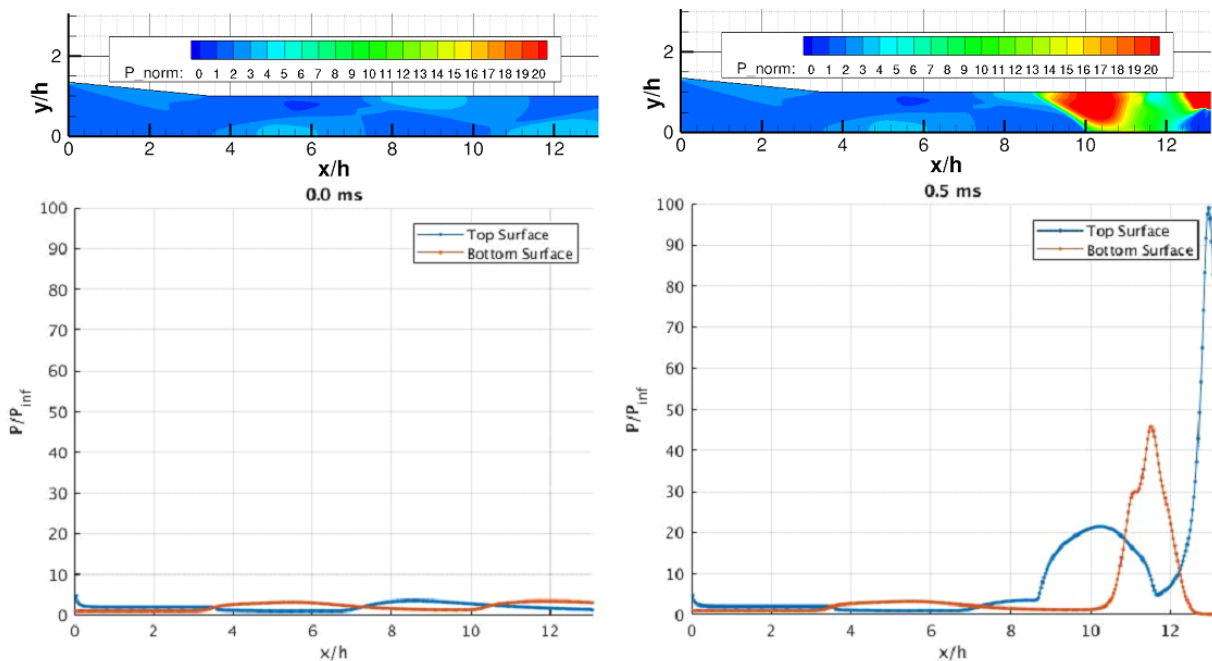
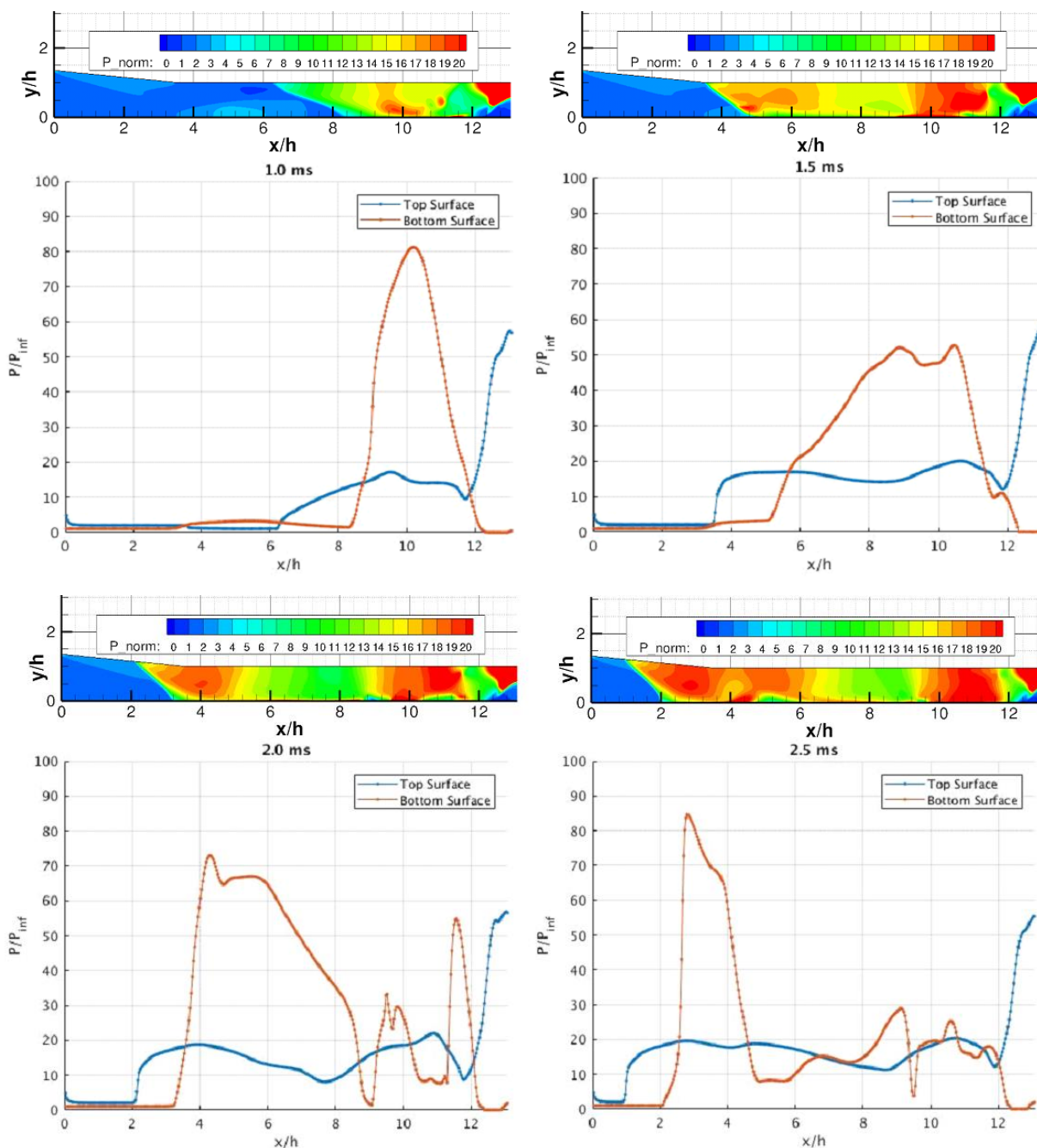


Fig. 3.21 2D Wall Pressure during Unstart at $t = [0.0, 0.5, 1.0, \dots, 2.5]$ ms

Fig 3.21 continued



Tracking the peak pressure as unstart progresses helps give an idea of how the top and bottom walls of the channel differ during unstart. Fig. 3.22 shows how the peak pressure value changes over time during unstart, as well as where the peak pressure is located in the channel. Note that the data were binned to exclude peak pressures in the region around the source term location. As seen previously, the pressure along the top wall of the channel is relatively constant and much

smaller than that along the bottom wall. However, over time as unstart develops, the same pulsing can be seen, as evidenced by the large changes in peak pressure location along the top wall.

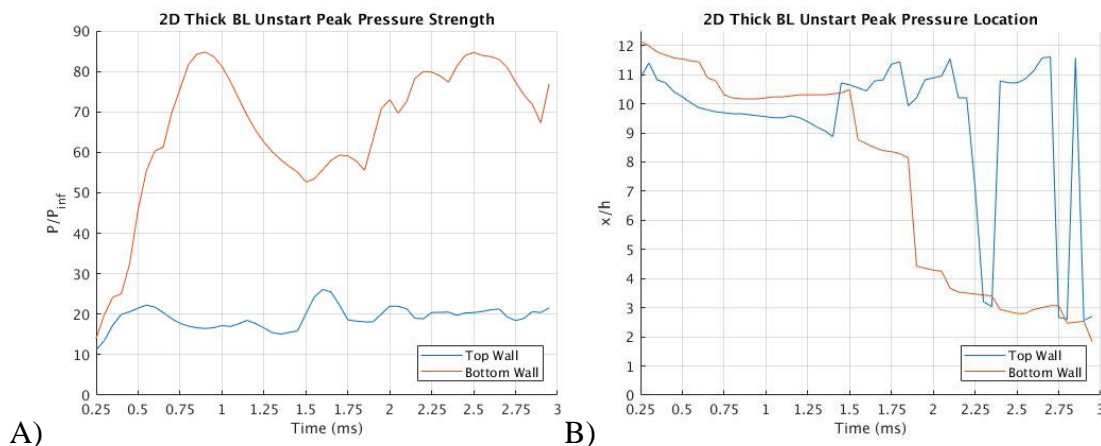


Fig. 3.22 2D Unstart Peak Pressure A) Strength, B) Location

Looking solely at the above figures, there appears to be no unstart precursor present. However, examining the data more closely yields some interesting results. The wall pressure difference, in particular, lends a higher resolution representation of what is actually occurring in the boundary layer during unstart. This difference is measuring how the pressure at all points along the top and bottom wall varies from its steady, fully-started value during unstart. If information is truly unable to pass upstream, this should simply be a flat line at $\Delta P = 0$, until unstart reaches that point. Once unstart reaches that point, it should have a huge, rapid increase.

Fig. 3.23 shows how the wall pressure changes during unstart and small pressure fluctuations can actually be seen prior to unstart reaching any particular point. The figures plot the normalized pressure difference between the fully started flow pressure and the pressure during unstart. The pressure along the top and bottom walls are plotted at several different time steps throughout the unstart process. The location of the leading edge of the unstart shock can be seen where the value asymptotes. The unstart precursors can be identified by the pressure spikes that grow in time as the unstart shock progresses upstream.

Dynamic changes in the wall pressure are present along both the top and the bottom walls of the inlet-isolator as unstart is progressing. These pressure fluctuations are of relatively minor strength, but become more pronounced as unstart travels nearer. The largest of these fluctuations measures only up to 20% of the normalized pressure. However, 20% of the freestream pressure of

5240 Pa is 1048 Pa. A jump in pressure of 1 kPa should be very detectable with pressure transducers that are calibrated to the freestream pressure, if they can collect the data quickly enough and are located at the right places in the channel. The location of the small pressure spikes appears significant and it is important to note that the pressure spikes preceding unstart occur at discreet locations within the channel, so will only be detectable in specific areas along the wall.

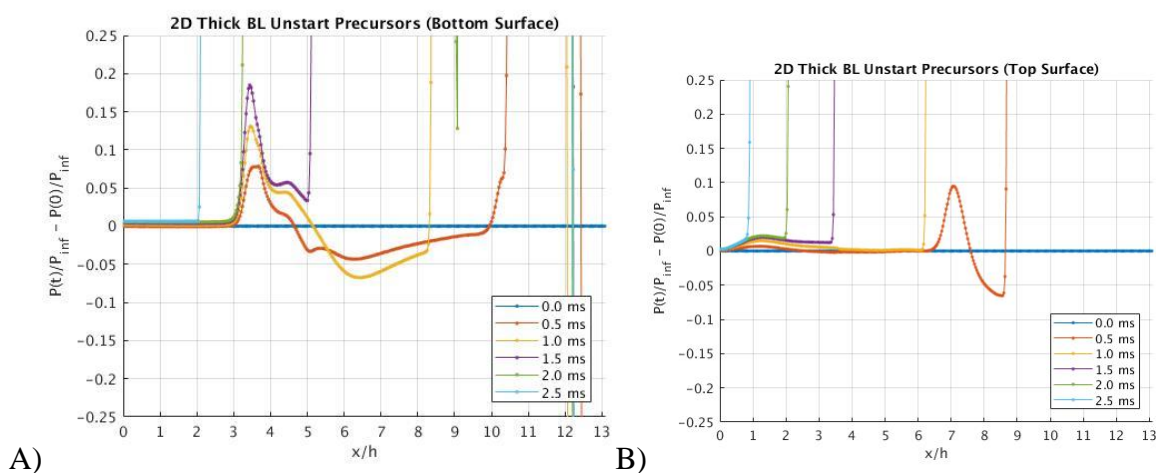


Fig. 3.23 2D Unstart Precursor Signal on Channel A) Bottom, B) Top

Interestingly, the pressure changes on the channel floor are several times larger than those on the channel ceiling. This difference suggests that the strength of the unstart precursor pressure spike is closely tied to the local boundary layer thickness. Additionally, when every time step is plotted, the peak values and locations for this potential unstart precursor become even more obvious, as shown in Fig. 3.24. Each line in the figures below represent a specific time step, and the strength of the precursors can be seen growing with time. The identified unstart precursors are enclosed in boxes for clarity.

The wall pressure changes in the boundary layer are roughly Gaussian distributions and exist upstream of the unstart shock system. As previously noted, they are located at key points in the channel. In particular they are located at the nexus of shock wave boundary layer interactions within the channel. They are positioned at approximately $x/h = 3.4$, $x/h = 7.1$, and $x/h = 10.3$. The first of these locations, at $x/h = 3.4$ occurs where that first oblique shock reflects off the channel floor. The second occurs where the second oblique shock reflects off the channel ceiling. And

finally, the last occurs where the third oblique shock reflects off the channel floor. These are all areas of thick boundary layer and strong interaction with the standing shock train.

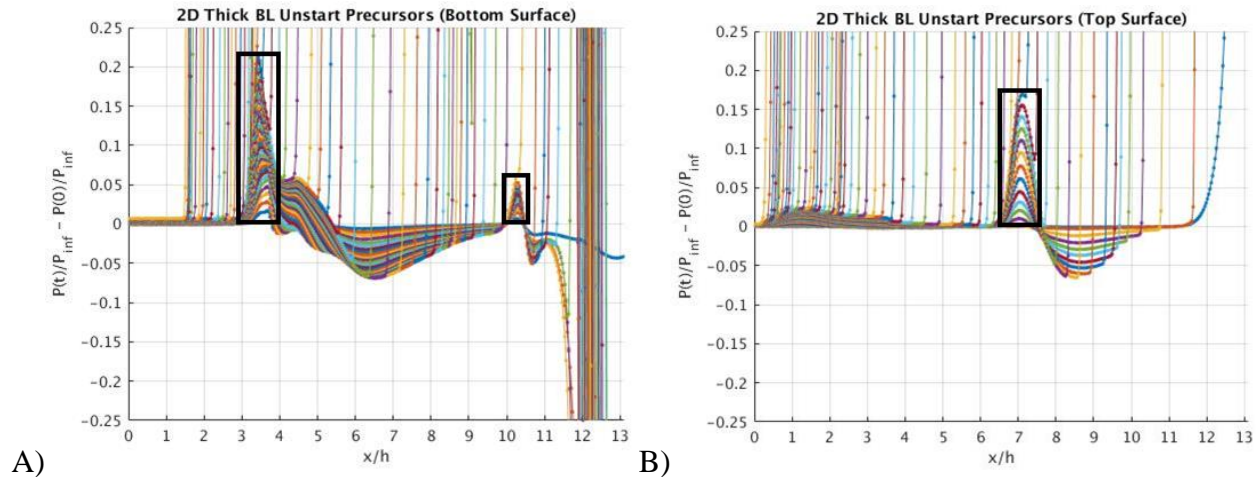


Fig. 3.24 2D Unstart Precursor Signal (all time) on Channel A) Bottom, B) Top

There is a weak signal at $x/h = 1.3$, where the first oblique shock intersects with the thick floor boundary layer, but it is the smallest of all the signals. It is postulated that this occurs because this station is on the channel ceiling in the portion of the test section where the roof has begun to angle up in the inlet ramp. This angling could make it harder for a signal to travel along the wall, as it would have to “turn a corner”, even though it is only a six degree adjustment. Apart from this initial small signal, the strongest precursor signal is the one located farthest from the isolator exit. It exists in the channel for the longest time before unstart reaches it, giving it the longest time to grow. Furthermore, it is the location of the thickest boundary layer in the channel.

These unstart precursor signals are of particular interest because they motivate a procedure that improves on unstart detection methods of the past, which are still not ideal. Donbar et al. [39] studied different methods of detecting predicting unstart and the best method they found was using pressure summation to determine the location of the leading edge of the oblique shock train. Finding a fluctuation in the boundary layer could create a pressure pulse indicating unstart well before the shock train leading edge has moved significantly, crucially decreasing the detection time for an unstart event.

Varadarajan and Roe [40] postulate that information can travel along a shockwave, assuming that shockwave has interacted with a particularly turbulent region, such as a vortex. Given that the

unstart precursors seen here are occurring at shock impingement points, it could be related to the mechanism they laid out. Without a three dimensional view and a deeper understanding of the dynamics, it is difficult to tell whether information is traveling through the boundary layer or along a shock wave. However, this theory seems reasonable, given that the precursors appear to reside where the shock wave impinges on the walls.

The next chapter will explore the same phenomena but in 3D, to determine how corner flows and other three dimensional effects change the behavior and what artifacts remain in the unstart flow. It will then be possible to delve further in the precursors and determine the effect of vortices and shockwave boundary layer interactions on them.

4. 3D COMPUTATION

Corner flows and other three-dimensional effects can have a significant impact on flow behavior and shock structure within a dual-mode scramjet inlet-isolator. It was found in the previous section that points within the test section where oblique shocks are reflecting off the walls and interacting dynamically with the boundary layer play an important role in the fully started flow and unstart flow structures. Marconi discussed the importance on corner flow on supersonic and hypersonic inlet performance [41]. In particular, he discussed the significance of “triple points” where two shocks interact with a surface. This can play a significant role in the unstart process, so the 2D simulations that were run previously, which established a computational baseline, were repeated using a 3D mesh to gain additional accuracy of the results and determine the significance of three dimensional effects of the steady and transient flow states.

4.1 Boundary Layer Development

Developing the required thick boundary layer for the 3D mesh proved quite problematic. In the end, imposing a thick boundary layer across the inlet of the mesh, as in 2D, proved to cause the computations to blow up and begin creating an ever-increasing number non-physical points, specifically negative density regions. After trying a variety of different computational schemes, mesh resolutions, and boundary layers, a solution was devised that, while not ideal in terms of computational cost, achieved the desired result. A larger mesh, shown previously in Section 2.33 was created. This mesh included a flat plate in front of the inlet-isolator, such that the desired boundary layer height developed naturally in the same computation as the inlet-isolator internal flow. While this increased the mesh size considerably, a number of cost-saving mechanisms were used, particularly a symmetry plane and a sponge layer on the flat plate.

The flat plate, representing the floor of the wind-tunnel was effectively an infinite plate, when compared to the inlet-isolator channel, so no sidewall effects from the wind-tunnel were taken into account. Thus, the flat plate portion of the flow field looks identical to the one shown in the previous chapter and does not need to be presented again. Instead, we can go straight to the fully started flow within the inlet-isolator.

4.2 Grid Independence Study

Although the 3D inlet-isolator mesh was based on the finest grid developed for the 2D case, it was important to ensure grid independence in 3D as well. Again, three grids, a fine mesh, a medium mesh, and a coarse mesh, were used to determine if the 3D solutions were grid independent. These grids were scaled in the same way as their 2D analogs, such that the same grid spacing was present in the 2D and 3D grids. The same Richardson extrapolation method was used as before. Two variables, skin friction coefficient and pressure, were investigated in order to examine the grid independence. For the 3D grid, they were investigated along the z centerline, in the xy plane of the channel. The value at the inlet was tested in the fully started mode of the flow, along the channel floor.

The extrapolated value from the Richardson analysis for the skin friction coefficient directly at the inlet was $C_{f\text{-exact}} = 0.00284726$. The error estimate was within the asymptotic range of convergence, with a value at 0.77131. In addition, the Richardson wall pressure at the inlet was $P_{\text{exact}} = 5383.6$ Pa. This solution was also within the asymptotic range of convergence with a value of 0.95858. For these calculations, the order of convergence was found to be $\zeta = 1.4$. Furthermore, these values match closely with the values found in the 2D calculations, giving further confidence to their validity.

Figure 4.1 shows a comparison in the normalized pressure in the channel along the z and y centerlines of the inlet-isolator, in the xy and xz planes. From these plots, the same flow structures can be seen in all three grids. As grid refinement increases, the main difference between the different flow fields is in the relative variance from the normalized freestream pressure in different regions of the channel. However, the difference in these regions of high and low pressure between the different grids is relatively minor. Particularly between the medium and fine grids, the values are almost identical, giving confidence that the solution sets presented in this thesis chapter, using the fine grid, will be effectively invariant to further grid refinement. With these results in hand, the following sections of this chapter will look exclusively at only the finest grid to develop a full analysis of the fully started flow, followed by the unstart dynamics.

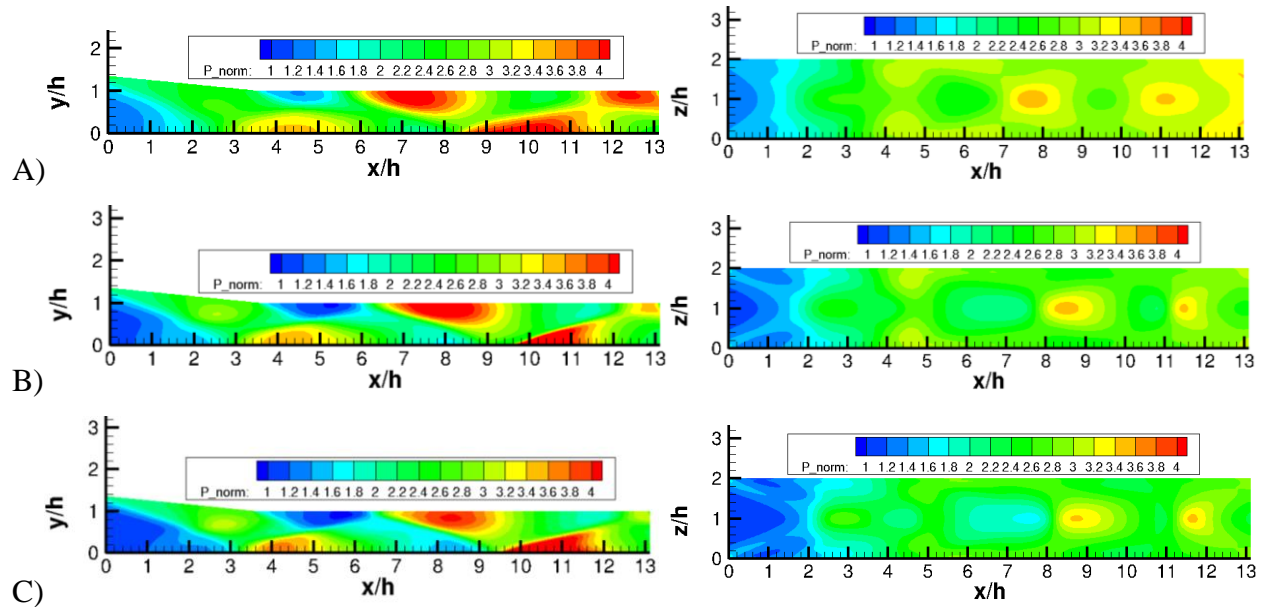


Fig. 4.1 3D Normalized Pressure Comparison A) Coarse, B) Medium, C) Fine

4.3 Fully Started Flow

The fully started flow within the channel looks much like the 2D flow seen in the previous chapter. Fig. 4.2 shows pseudo-Schlieren image on the flow field in 3D, from the perspective of the z centerline and compares it to the fully started flow field in 2D. The same four oblique shocks of the shock train can be seen, but they have become somewhat more dissipated and smeared. This is the first indication that the three-dimensional effects are changing the flow field, but at this point, the differences remain relatively insignificant. In addition to the dispersion of the flow near the shocks, the shock impingement points have also shifted slightly upstream, towards the inlet, relative to the 2D flow. The three wall impingement points of the four shocks have moved from $x/h = [3.4, 7.1, 10.3]$ to $x/h = [3.2, 6.6, 9.2]$.

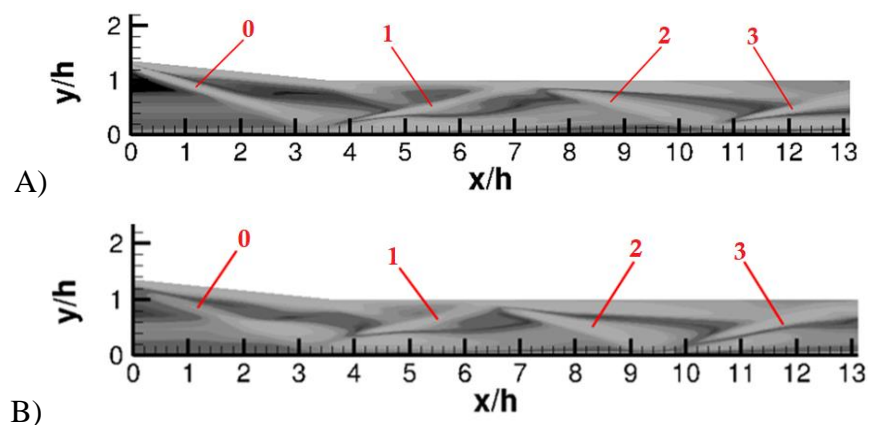


Fig. 4.2 Pseudo-Schlieren Image of Fully Started Flow A) 2D, B) 3D

Next, the Y-centerline is examined and a clear contribution of the sidewalls on the flow field can be seen, as shown in Fig. 4.3. Just at the initial vertical oblique shock is tripped by the inlet ramp, two lateral oblique shocks are triggered by the flow encountering the sidewalls of the inlet channel. The transverse shocks modify the flow by adding additional turbulence and shockwave boundary layer interactions, in addition to the perpendicular shock-shock intersections within the test section.

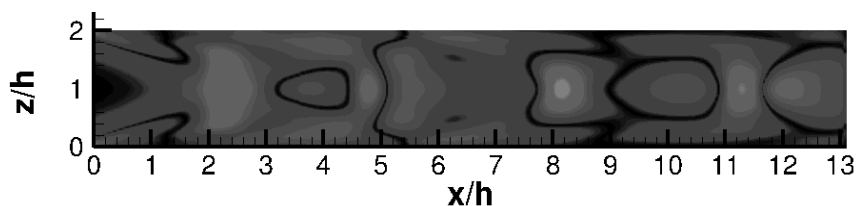


Fig. 4.3 Pseudo-Schlieren Image of 3D Fully Started Flow Y Centerline

To develop a deeper understanding on how the 3D geometry changes the flow field, the normalized pressure is investigated. It is compared to what was found in the 2D computations on the fine grid in Fig. 4.4. In this figure, the differences between the 2D and 3D flows becomes clearer. While the same general flow features exist in both solution sets, the 3D flow has consistently high pressure, through the channel. The oblique shock train creates higher pressure disturbances along the top and bottom walls. In addition, the approximate size of these pressure jumps across the shocks grows as well. Moreover, certain portions of the flow field are more smeared out, specifically near the channel floor before $x/h = 3$ and in the channel center around

$x/h = 7$. These are locations where, as seen above in Fig. 4.3, the oblique shocks from the sidewalls intersect.

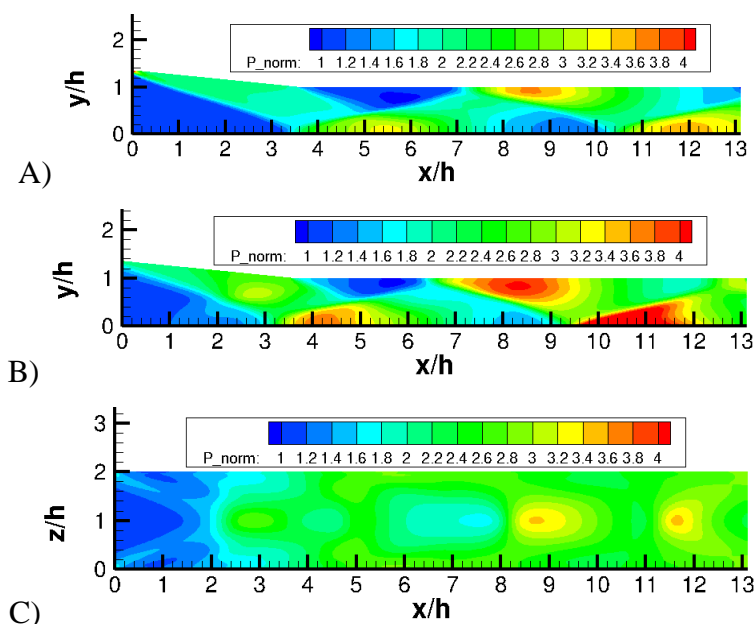


Fig. 4.4 Fully Started Flow Pressure A) 2D, B) 3D Z-Centerline, C) 3D Y-Centerline

Given the limited data available from the experiments, the two main quantitative comparisons that can be made to validate the results are the PIV images and the pressure traces along the channel floor. To this end, Fig. 4.5 shows the computed velocity field from the 3D flow fields. They match well with the 2D and experimental values, although these 3D flow fields have a slightly larger region of high speed flow in the channel center. They are very close to the PIV images from experiment upstream, near the inlet section, but match slightly worse than the 2D results, especially further downstream. This could be due to the strength of the sidewall shocks. The sharp leading edge of the channel sidewalls on the computations may be sharper than in experiment, causing an increased shock strength that promotes mixing and changes the flow features from the 2D baseline as the flow moves towards the channel exit. Additionally, these flow contours are taken along the channel centerline, whereas the PIV data is through the width of the channel. Looking at the y centerline flow contours, the sidewalls appear to have a significant effect on the flow and their contribution should shift the computational results more in line with what is expected based on the PIV images. Furthermore, although the velocity field for the 3D channel

features some regions of slightly larger Mach number than in the PIV data, the wall pressure along the centerline of the channel matches much more closely with experiment.

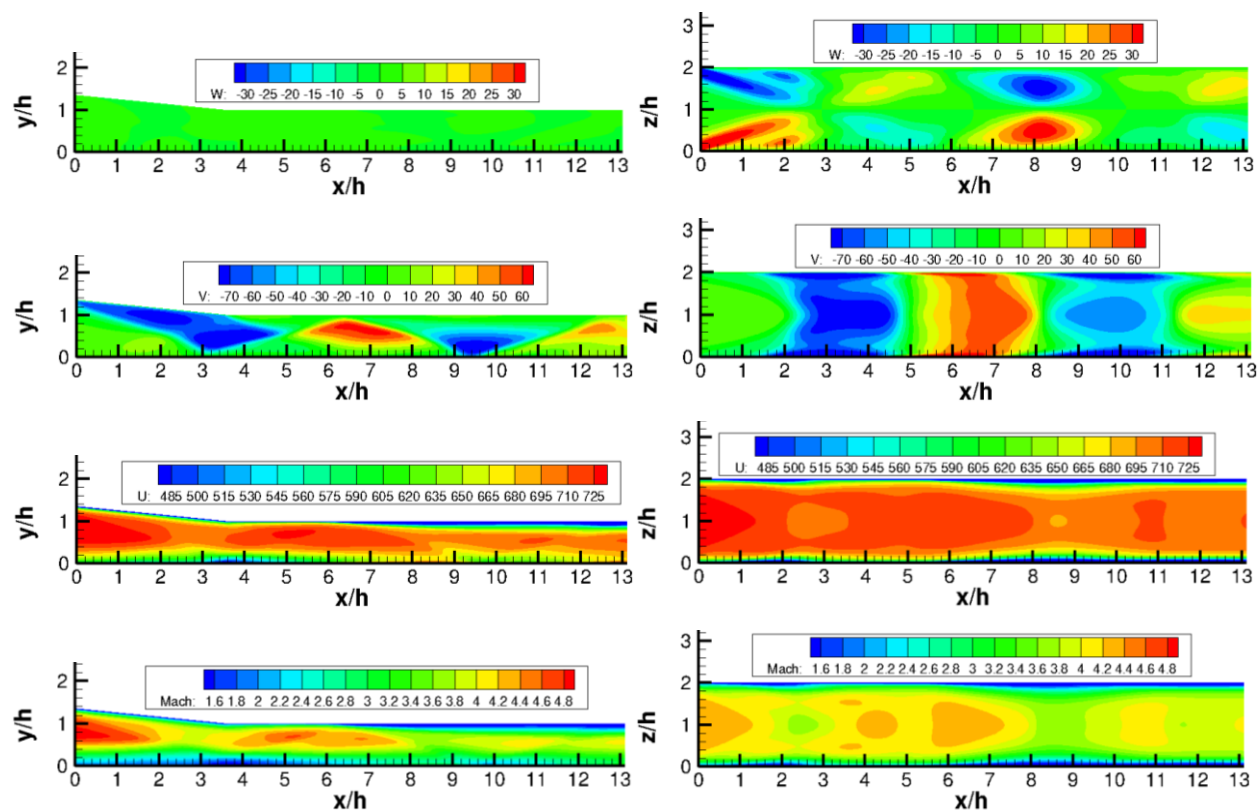


Fig. 4.5 3D Velocity Field for Z Centerline (L) and Y Centerline (R)

Next, Fig. 4.6 compares the floor wall pressure from the 3D computations, along the channel z centerline, with the values found in the 2D computations and with those found in experiment. The 3D values match much closer with the experimental values, both in the location of the pressure peaks and in the strength of those peaks. The figure below also compares the channel ceiling wall pressure along the same centerline with the 2D computations. The same general trend is seen in the ceiling pressures as was seen on the floor pressures, with the wall pressure peaks shifting upstream and getting stronger. In addition, there is a small pressure rise near the inlet at around $x/h = 3$, that is likely due to the transverse oblique shocks, as mentioned previously.

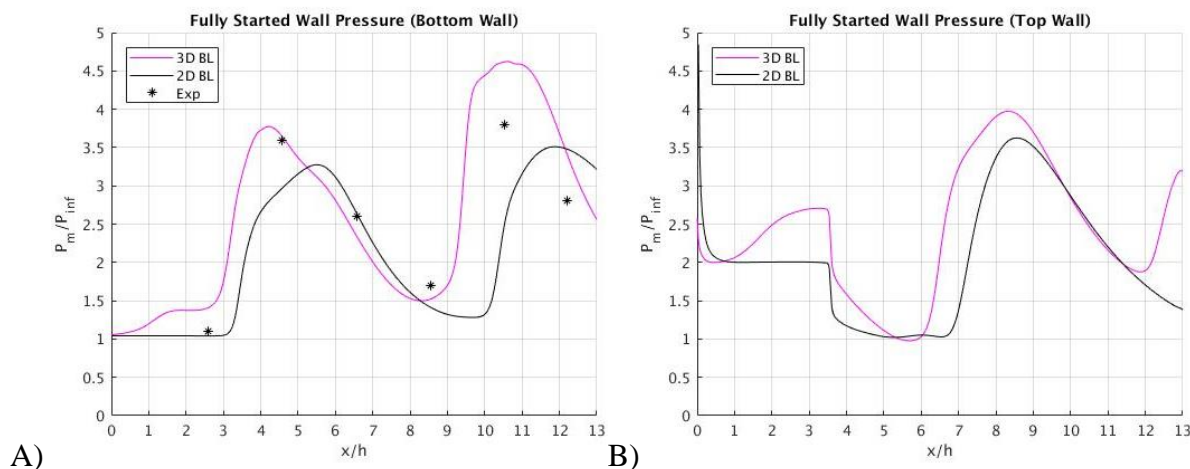


Fig. 4.6 Normalized Wall Pressure of 3D Fully Started Flow on Channel A) Floor, B) Ceiling

4.4 Unstart

Simulating unstart in 3D was accomplished as in the 2D case, with a few key differences. As for the 2D case, the steady state flow was used for the initial condition and the source term was implemented. The 3D source term was an oblate ellipsoid instead of an ellipse, as it was implemented in 3D. It was located in the same location as before, centered at $x = 328$ mm, $y = 10$ mm, and $z = 25.4$ mm. This corresponds to the isolator exit (x), just above the floor (y), and in the channel center (z). Several different force strengths were investigated to initiate unstart. Although the same force could be used as in the 2D case, this proved too strong in 3D as it led to non-physical points in the solution. Investigating unstart across a range of forces, 500 N was determined to be the minimum force required to initiate unstart in 3D. Given that the flap in the experiments was tuned to the minimum angle to initiate unstart, this value for the force was deemed acceptable for the simulation. It would be able to trip the unstart reaction without overdriving it into something unrealistic.

Moreover, Sato and Kaji [42] found a link between combustor pressure rise disruption strength and speed of unstart, but noted that the actual unstart shock strength was mostly unchanged across different levels of pressure rise. While the speed of unstart in these 3D calculations will likely be different than experiment and the 2D case, all the relevant phenomena should still be applicable and have reasonable/comparable values for study.

The 3D computational results were processed to create a density gradient magnitude plot, and the resulting pseudo-Schlieren images at selected time steps during unstart are compared to

the experimental value from the University of Texas, Austin in Fig. 4.7. The displayed computational results are taken from the z centerline slice in the xy plane. The experimental data represents as average over the optical path, or z -direction. As in the 2D case and the experimental results, the leading edge of the unstart shock is angled in favor of the channel ceiling. Furthermore, the shock is strong enough to completely disrupt the incoming flow and overpower the standing shock train, while leaving the portion of the shock train preceding unstart unchanged. As before, the region boxed in blue represents the area visible in the view window from the experiments.

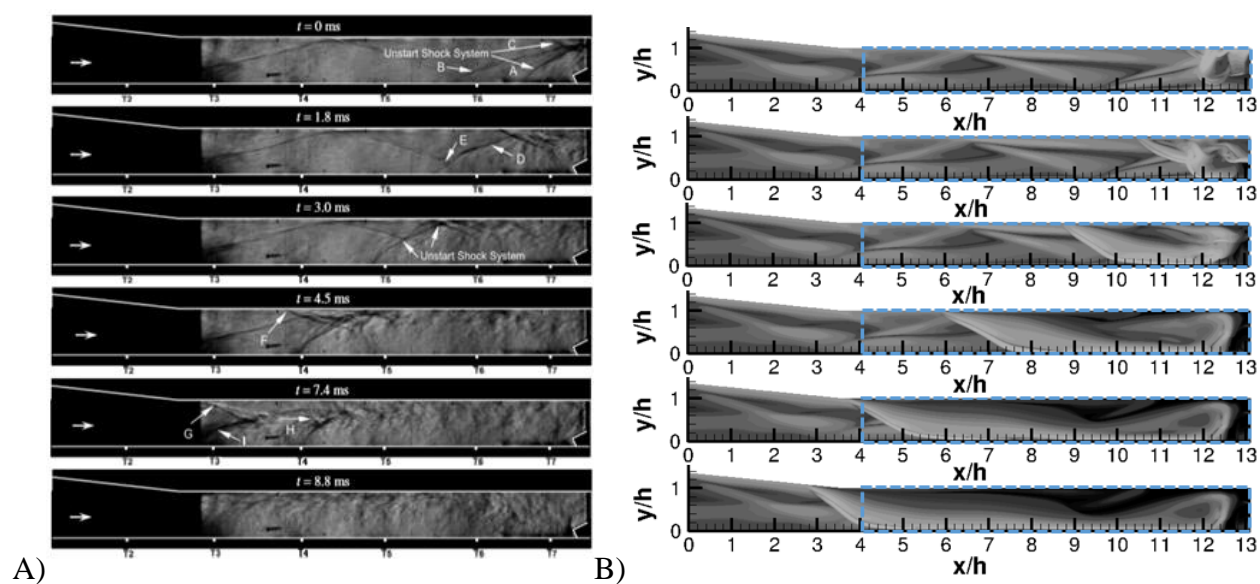


Fig. 4.7 Unstart A) Schlieren Images used with permission [19], B) 3D Pseudo-Schlieren

The normalized pressure during unstart, shown in Fig. 4.8, starts to show some more significant differences between the 2D and 3D computations. The normalized pressure within the unstart region in 3D is approximately three to four times higher than that seen in 2D. The same pulsing phenomena of the pressure increasing and decreasing in strength as it passes the different shocks in the channel can still be identified, but the effect is much stronger. In addition, with 3D it becomes clear that the z centerline of the channel is actually not the true leading edge of the shock. Instead, the unstart shock along the sidewalls is the leading edge. However the vertical centerline of the channel still sees the largest pressure rise during unstart. The xz shape of the shock is highly dynamic, with the leading edge of the shock along the walls growing further from

the centerline shock initially. This is followed by the sidewalls shocks rebounding and actually falling behind the centerline shock momentarily, before gaining on it again, in a pulsing motion.

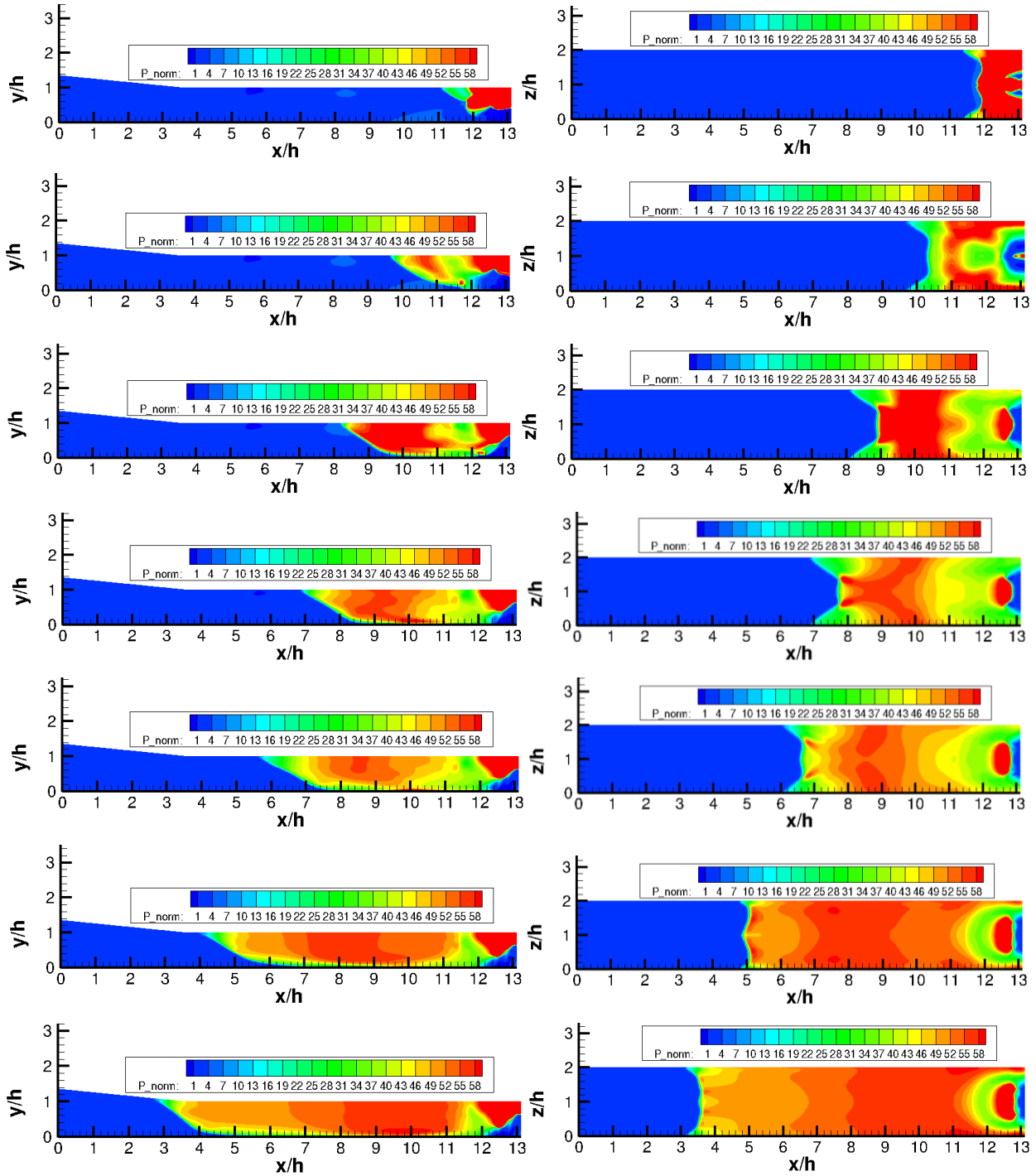
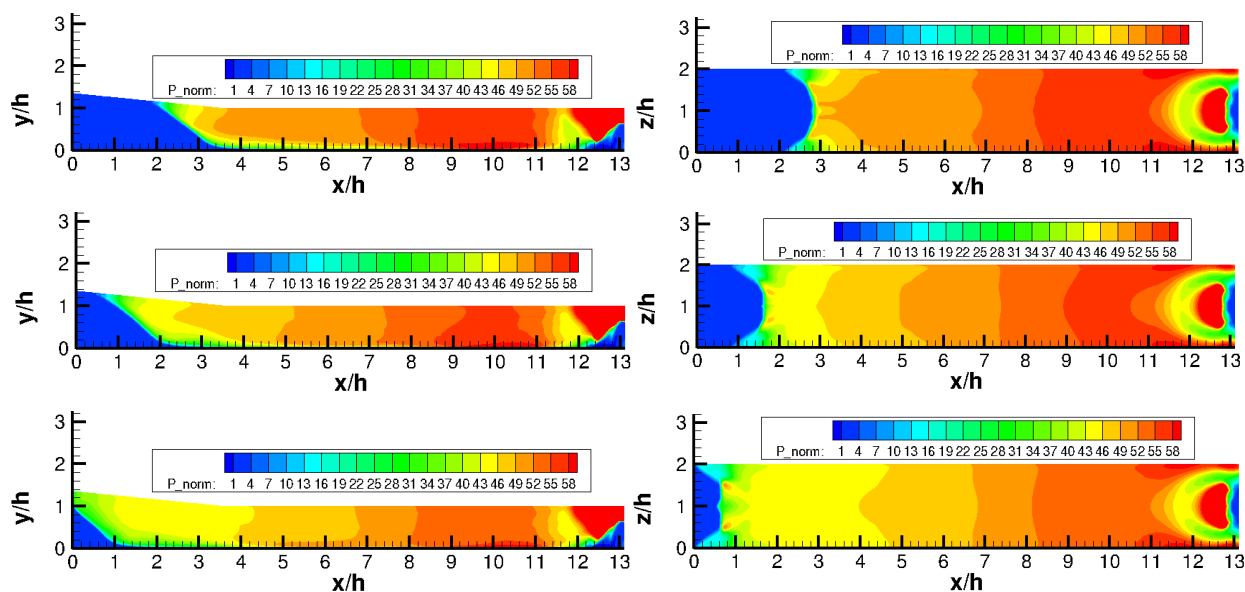


Fig. 4.8 3D Unstart Pressure at $t = [0.05, 0.10, 0.15, \dots, 0.5]$ ms

Fig. 4.8 continued



The unstart speed in 3D is even faster than in 2D, which was already roughly twice the speed of the experimentally measured unstart. Fig. 4.9 shows a plot of the unstart speed, as measured by the location of the leading edge of the shock in the z centerline slice through the channel. Although this is not the true leading edge, as described above, it is the position measured in experiment, so is the most relevant location to analyze. In addition, tracking its path still provides a solid value of the speed as the relative location of the unstart shock between the channel center and sidewalls only sees minimal change throughout the whole unstart process. As before, the shock location was measured by where the normalized pressure in the channel is at least five times the freestream pressure. The mean unstart speed, normalized by the freestream velocity, along the top and bottom walls of the channel was observed to be 0.9257 and 0.7798, respectively in the 3D computations. Comparing to the experimental value of 0.0625, the speed is approximately 12 times the value found in experiment. Like Jang [21], the computations presented here were unable to match the speed of unstart. However, the other data related to unstart matches well with experiment and the computations can still allow us to match relative comparisons between different conditions, as will be demonstrated in Chapter 5.

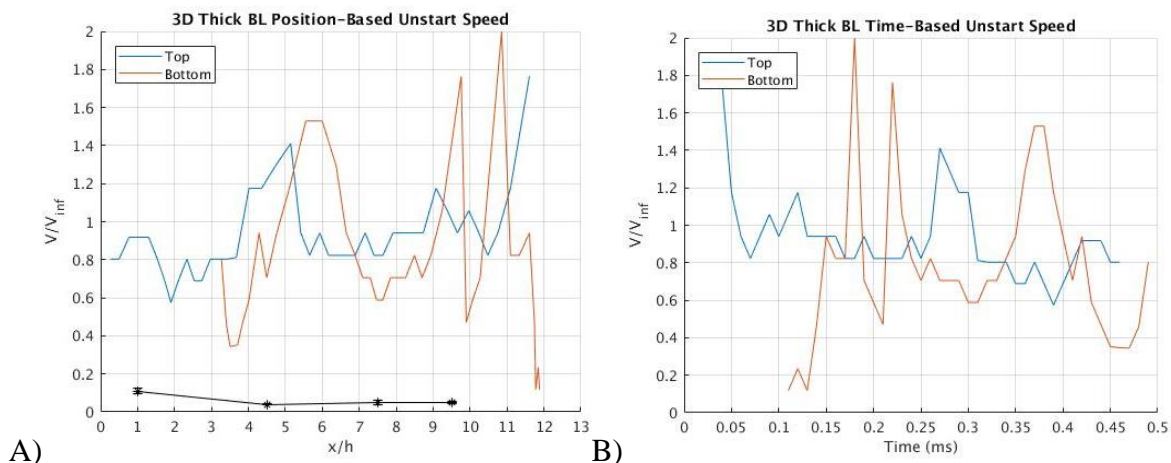


Fig. 4.9 Unstart Speed through 3D Inlet-Isolator vs A) Position, B) Time

As with the 2D computations, plotting the shock arrival time during unstart, as seen in Fig. 4.10, can enhance the understanding of this transient process. In the 3D case, the shock on the channel floor is delayed, relative to the channel ceiling. This indicates that the angle of the shock is much smaller, or more oblique. Additionally, the shock position along the two walls grows closer in the x -direction towards the end of unstart around $t = 0.35$ ms, as seen in 2D. However, they lines actually start to diverge soon after as the shock reaches the channel entrance.

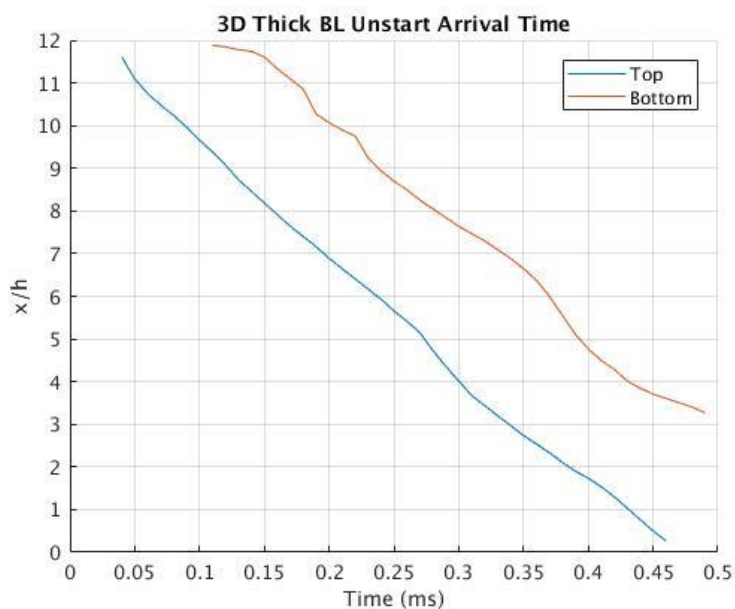


Fig. 4.10 3D Unstart Shock Arrival Time

Tracking the Mach number within the inlet-isolator during unstart also establishes some key differences in the 2D and 3D cases. Fig. 4.11 shows that, as unstart progresses and more of the channel becomes subsonic, bubbles of supersonic flow develop within the subsonic region and travel downstream, away from the unstart leading edge. This is the same phenomena as seen in 2D but the supersonic region within unstart is much smaller in 3D and confined to the area adjacent to the source term. Instead of a large bubble of supersonic flow extending near the top wall upstream through the channel, a large almost-stagnant region of the flow develops. The vortex created by the ramp and the vortex created by the unstart shock running up against the oblique shock train churn the flow to create this. In addition, the channel floor stays much more insulated from the effects of unstart as the shock moves upstream, explaining the low wall pressures observed in experiment compared to the higher values seen in the flow field.

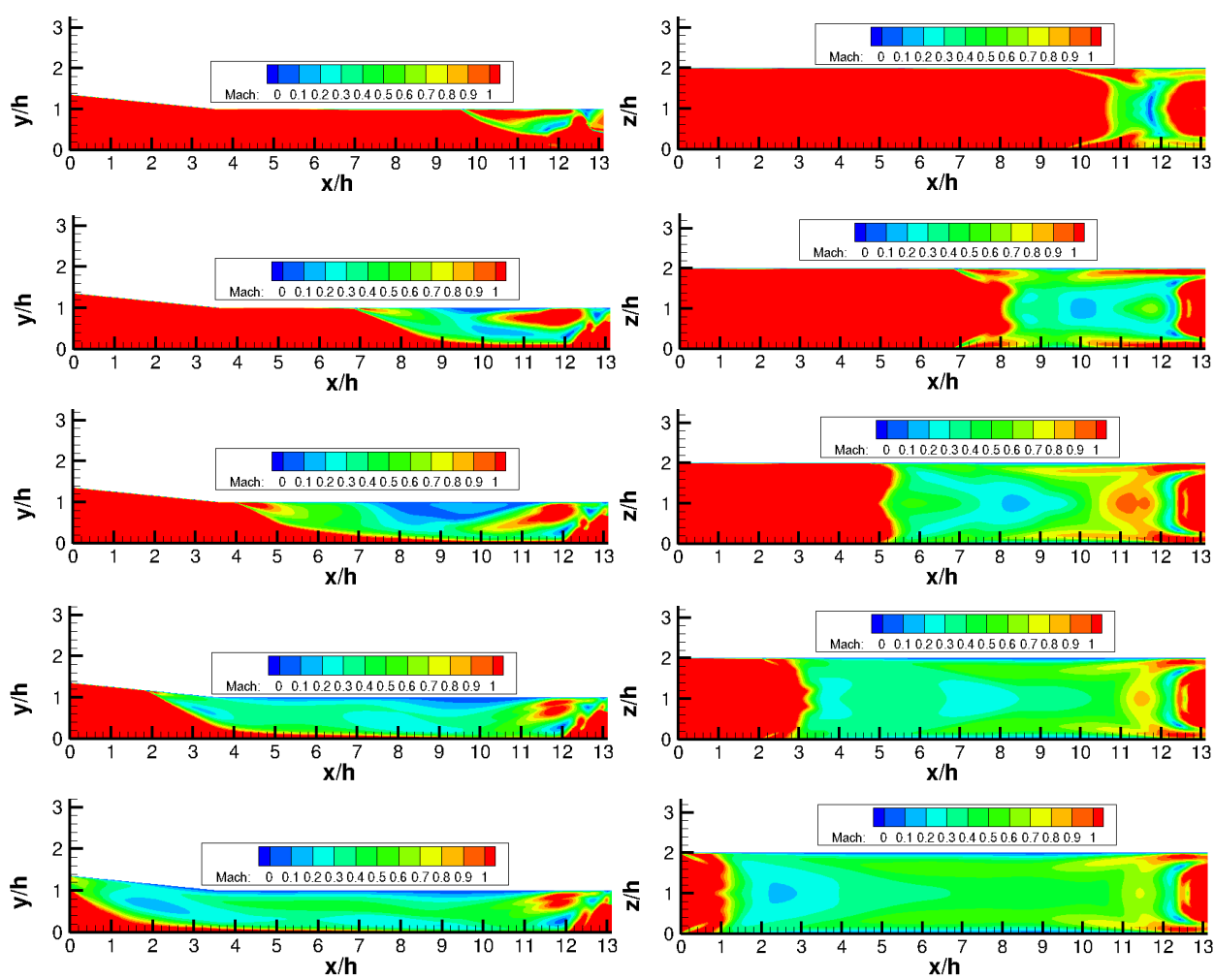


Fig. 4.11 3D Regions of Subsonic Flow during Unstart at $t = [0.1, 0.2, 0.3, \dots, 0.5]$ ms

In addition to the oblique shocks and sidewall effects, it is likely that corner vortices are playing a role in disrupting the flow. The role of corner vortices in a Mach 4.9 inlet isolator model was explored by Huang et al. [43]. They identified two types of corner vortices that may be present in hypersonic flows within rectangular channels. These two vortex types are one and two celled vortices that either start with streamlines spiraling inwards or outwards, depending on the type, when they form. These occur at different streamwise locations within the channel and have a strong influence on the flow dynamics and propensity of the system to unstart.

Similarly, Xiang and Babinsky found a significant effect of corner flows on the separation within rectangular supersonic channel flows, albeit at a lower Mach number of 2.5 and different channel cross-section [44]. In particular, the corner vortices have a strong influence on the average separation length in channels that feature oblique shocks. Fig. 4.12 shows the vorticity of the unstart flow halfway through the unstart process, at $t = 0.25$ ms. The flow field shows three streamwise slices and the normalized pressure on those slices at the walls of the channel and the channel center plane, specifically $z/h = 0, 1,$ and 2 . In addition, the channel floor is visualized and three x -plane slices in the vicinity of the unstart leading edge. Vortices can be seen spiraling in towards the channel center from the sidewalls. Perpendicular to those, vortices can be seen forming at the unstart leading edge. These vortices all combine to create a highly turbulent region in the wake of the unstart shock that progresses upstream with it.

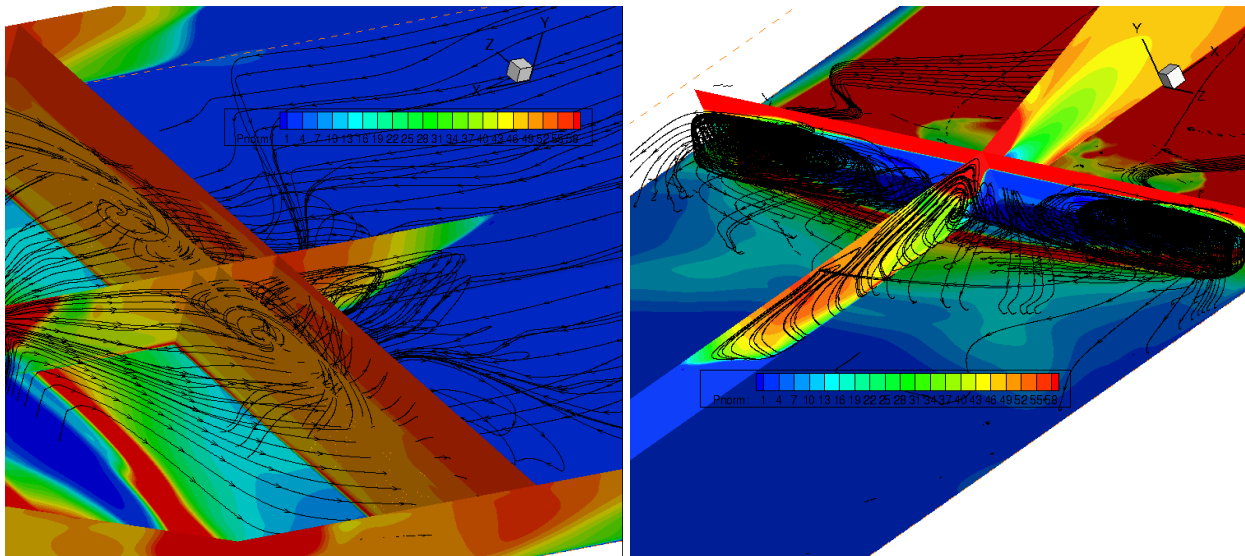


Fig. 4.12 3D Corner Vortices

4.5 Unstart Precursors

Next, the potential unstart precursor signals identified in the 2D simulations were investigated in 3D to verify their presence and determine how their strength would be affected in the 3D computations. Fig. 4.13 tracks the normalized pressure strength along the top and bottom walls of the channel as unstart progresses. As before, the wall pressure shows seemingly no change until unstart reaches it, at which point it undergoes a massive spike. The pressure along the top wall follows a similar trend as seen in 2D, but with a higher pressure. Rather than flattening out to roughly 20 times the freestream pressure, the wall pressure in 3D settles to around 60. This follows the pressure in the majority of the flow field, being approximately three times that seen in 2D. On the other hand, the wall pressure along the channel floor is quite different in 3D. It proves to be much less erratic and sees significantly lower values, around 30 in the majority of the unstart region. This is much closer to what was seen in experiment and shows that the floor of the channel sees a delayed response to unstart and is somewhat insulated from its pressure effects due to the thick boundary layer and its interactions with the shocks and vortices in the channel.

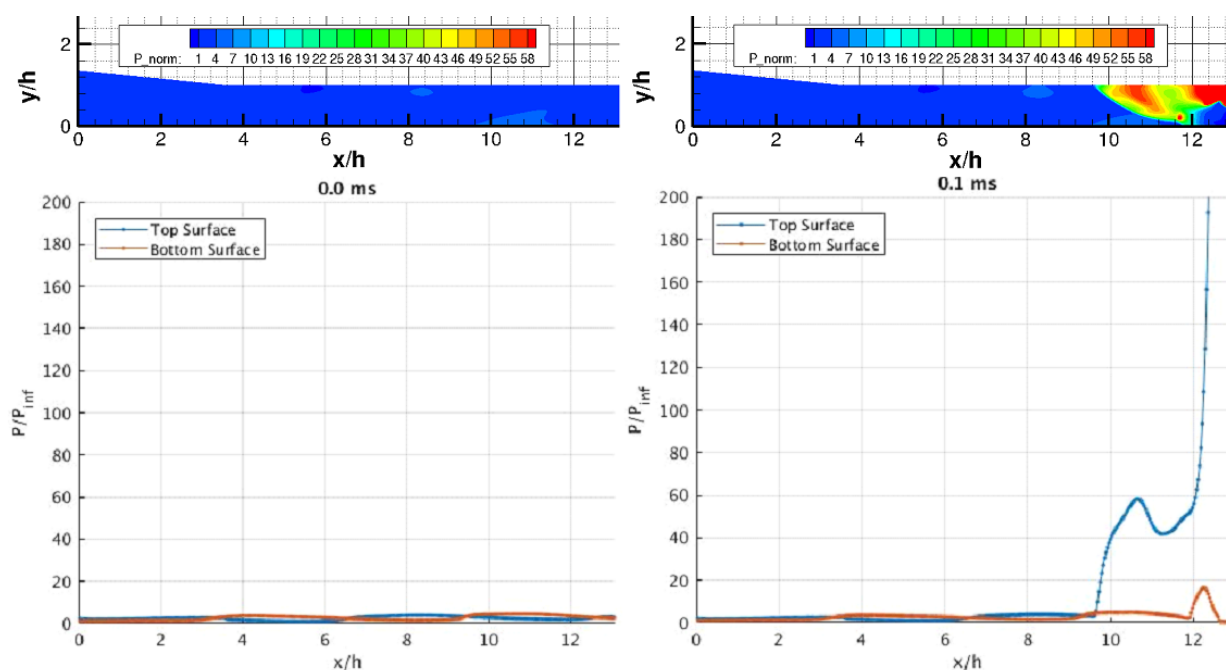
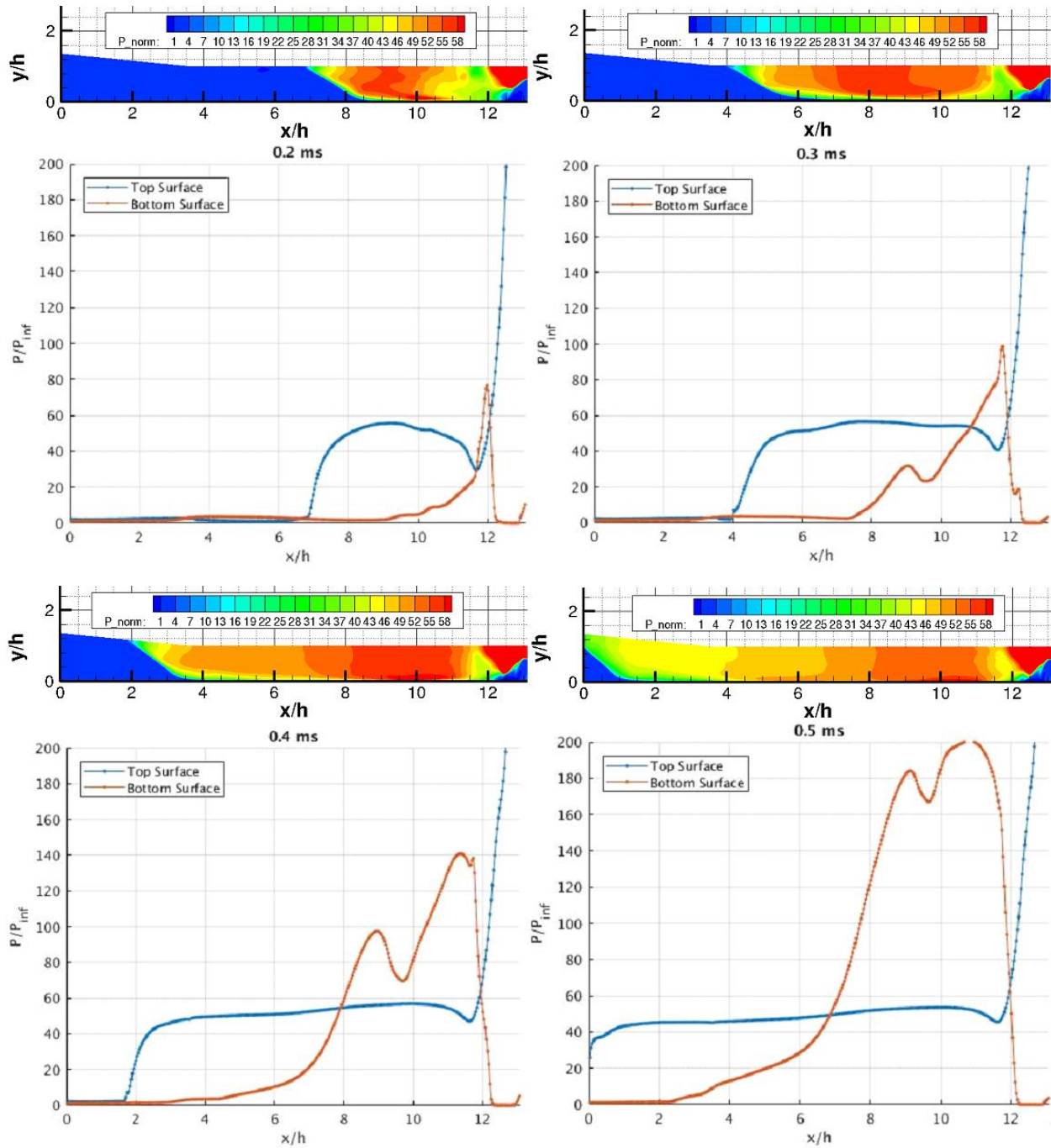


Fig. 4.13 3D Wall Pressure Traces during Unstart at $t = [0.0, 0.1, 0.2, \dots, 0.5]$ ms

Fig 4.13 continued



The peak pressure along the top and bottom walls is shown in Fig. 4.14. The top wall peak pressure grows in strength as unstart propagates upstream, but the location of this peak can be seen pulsing as before. In addition, the pulses are larger and last longer than in 2D. The bottom wall, on the other hand, sees a bimodal distribution of peak pressure through unstart. For this reason,

two lines are plotted for the bottom wall, one for each peak. This two-peaked response shape indicates that there is an initial pulse of information through the boundary layer as unstart first reaches a point, then another more sustained pressure rise as the turbulent vortices fully disrupt the boundary layer.

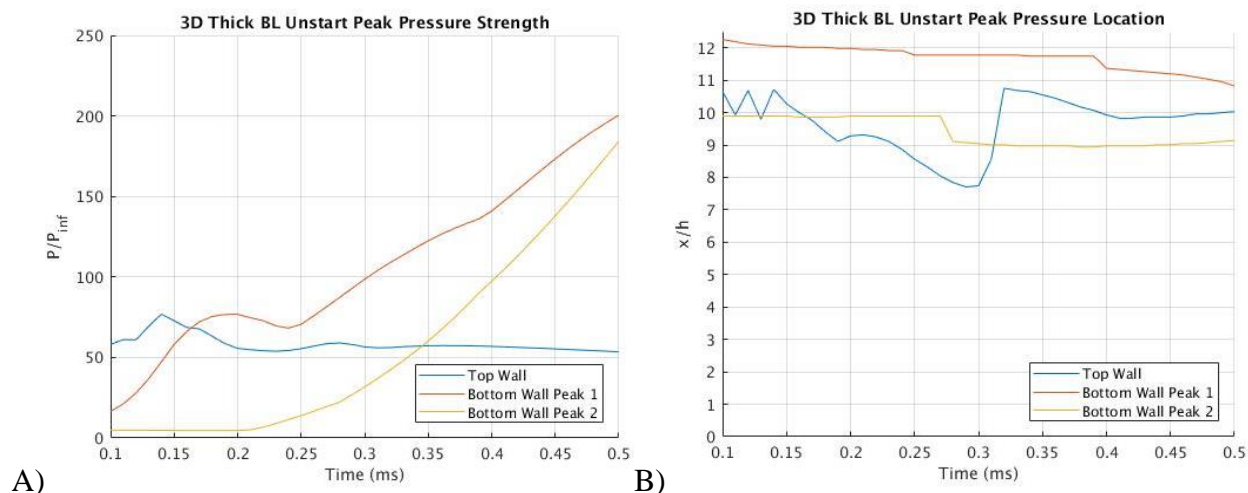


Fig. 4.14 3D Unstart Peak Pressure A) Strength, B) Location

Precursors to unstart again appear in the difference in the normalized pressure from the baseline wall pressure is examined. Fig. 4.15 shows that the wall pressure is changing in the region upstream of unstart. In fact, in 3D, the changes are significantly larger, both in strength and in the area of the affected region. Several interesting changes are seen in the precursor signal when modeled in 3D. First, the small precursor signal on the top wall around $x/h = 1.3$ entirely disappears. The other signal on the top wall stays in the same general location and has approximately the same strength, but gets about twice as wide. On the bottom surface of the channel, the first precursor signal, at around $x/h = 3.4$ flips to negative. It is in the same relative position, but instead of an increase from the baseline pressure of 5240 Pa of 20%, it sees a decrease of 20%. Finally, the bottom surface precursor signal closest to the flap becomes over ten times stronger than in 2D and is now the location of the strongest signal. In addition, the locations of all the signals shift downstream slightly, staying aligned with the location of the oblique shock impingement points of the shock train along the channel walls, as before. This indicates that their locations are determined by the shock train, as initially thought, rather than being a function of the invariant channel geometry.

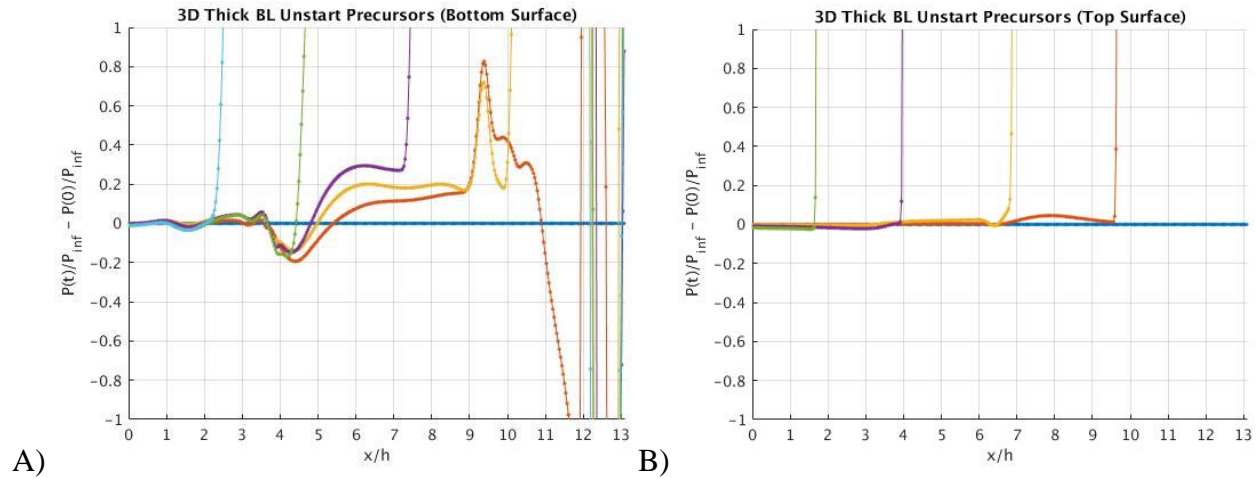


Fig. 4.15 3D Unstart Precursor Signal on Channel A) Bottom, B) Top

Finally, Fig. 4.16 tracks the precursor signal progression over the whole of unstart. Each line represents a time step in the unstart computation. The values asymptote when unstart arrives at that specific location, but also see significant change preceding that event. The signal near the isolator exit should be more easily detectable, but will be present for only a short time. The two main signals near the channel center are relatively unchanged in magnitude and location from the 2D simulations, and are still reasonably strong, so would be good candidates for experimental detection.

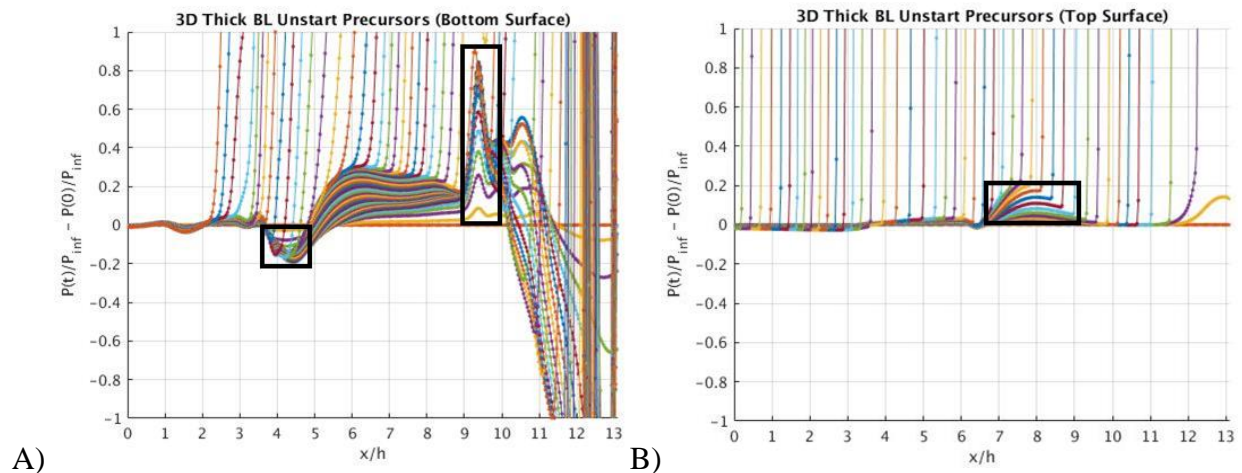


Fig. 4.16 3D Unstart Precursor Signal (all time) on Channel A) Bottom, B) Top

5. PARAMETRIC STUDY

With a firm grounding in experimental data and some hypothesized unstart precursors identified, it is important to see how well these results hold for different flow configurations, in order to draw some more generalizable conclusions. This chapter examines some variations on the flow field and channel geometry, looking specifically at the effect of boundary layer thickness and aspect ratio of the channel on the dynamics and structures in both the steady state, fully started flow and during the transient unstart response.

5.1 Thin Boundary Layer

Sato et al. [42] investigated the effect of compound choking on unstart. They found that unstart strength seemed to be dictated by boundary layer thickness and separation, with a larger boundary layer leading to stronger unstart. Although the experiments were carried out at Mach 3, their results indicate the presence of a correlation between unstart propagation and boundary layer thickness. These findings were further reinforced by Do et al. [45] [46], who also found that thicker boundary layers lead to faster unstart. Do et al. used a mass injection jet to initiate unstart in their study, and analyzed different thickness boundary layers on the different walls of the isolator channel.

Fiévet et al. [47] also discuss the effect of boundary layer thickness on shock train behavior in a channel with supersonic flow. They reached two main conclusions on flow behavior as boundary layer thickness is decreased, namely that the shock train moves downstream and the shocks become stronger. This difference should be detectable in the fully started flow and will also likely cause some differences in the unstart behavior. In order to explore the effect of the thick floor boundary layer seen in experiments on the flow within the inlet-isolator test section, the computations presented in Chapters 3 and 4 were rerun, without the imposed floor boundary layer. This section details the results of that study.

In the next two sections, the results previously presented, with the large imposed floor boundary layer will be referred to as the “Thick BL” cases. Alternatively, the computations run for this section, where the boundary layer on the channel floor was only allowed to develop starting from the leading edge of the channel inlet will be referred to as the “Thin BL” cases. Recall that

in all the computations and in the experiment, the channel ceiling and sidewalls (if 3D) have a boundary layer that develops only starting from the leading edge of the channel inlet.

5.1.1 2D Thin Boundary Layer Fully Started Flow

First, a fully started flow was created using the same mesh and freestream conditions as in the previous chapters, but no floor boundary layer was imposed at the inlet. Fig. 5.1 shows a pseudo-Schlieren image of the fully started flow with a thin boundary layer developing from the inlet on the floor as on the ceiling. The same four shocks are present in both the thick and thin boundary layer cases, but the shock impingement points have shifted downstream from approximately $x/h = [3.4, 7.1, 10.3]$ to $x/h = [4.1, 7.8, 11.2]$ when there is no thick boundary layer present. This downstream shift with thinner boundary layer matches the trend predicted by Fiévet.

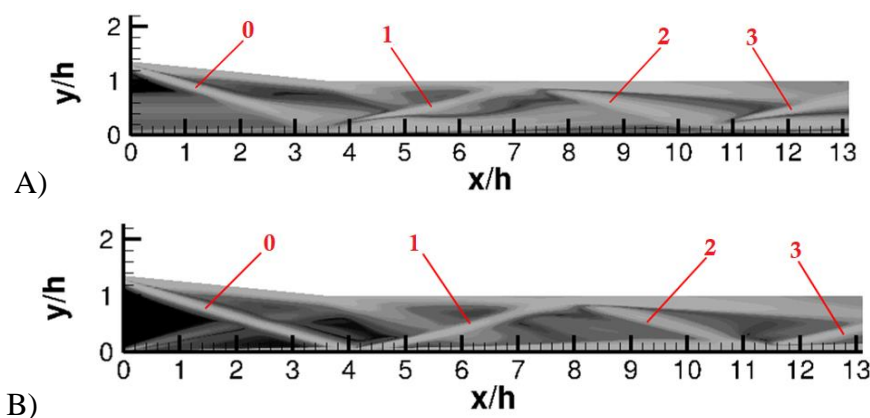


Fig. 5.1 Pseudo-Schlieren Image of 2D Fully Started Flow A) Thick BL, B) Thin BL

The shock strength can also be seen to be stronger in the thin boundary layer case, as evidenced by the thicker shock lines in Fig. 5.1. The shocks appear sharper, indicating that the thick boundary layer case acts to disperse the shock, reducing its strength. This also matches with the predictions of Fiévet et al. for increased shock strength with reduced a boundary layer. In fact, the entire flow field is much less homogeneous, with significantly less mixing present in the thin boundary layer case.

To investigate this further, the u , v , and M velocity fields of the flow can be compared between the thin and thick boundary layer cases. Fig 5.2 shows that the flow is much faster in the thin boundary layer case, with the supersonic core flow remaining above Mach 4 throughout the

channel, as opposed to the thick boundary layer case where it drops below Mach 3. Effectively, the thin boundary layer case acts as if the flow were in a bigger channel. The y-velocity, v , is relatively unchanged, presenting a slightly skewed version of the original flow when the boundary layer is reduced. The x-velocity, u , on the other hand, shows a much larger and more robust supersonic core flow, with the flow near the ceiling quite similar to the initial case and the flow near the floor substantially different. In the thin boundary layer case, the ceiling boundary layer becomes the dominant subsonic region of the flow.

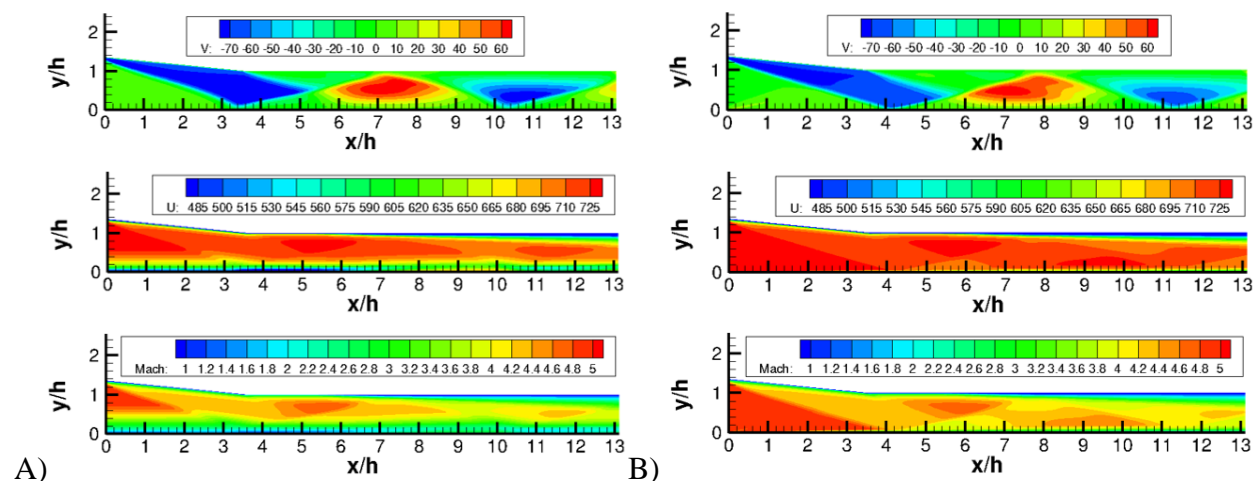


Fig. 5.2 2D Velocity Field A) Thick BL, B) Thin BL

The pressure, normalized by the freestream pressure, tells a similar story. Fig. 5.3 compares the fully started flow pressures between the thick and thin boundary layer cases. The pressure fields are quite similar, but the pressure within the flow field remains higher throughout the flow in the thin boundary layer case. In fact, while the flow structures in the pressure field are effectively the same between the two cases, the regions of high pressure are more accentuated in the thin boundary layer case. Overall, there are larger spatial regions of high and low pressure as the flow passes through the oblique shocks and expansion fans in the flow. This is likely due to the stronger shocks causing a larger pressure change at the shock impingement points.

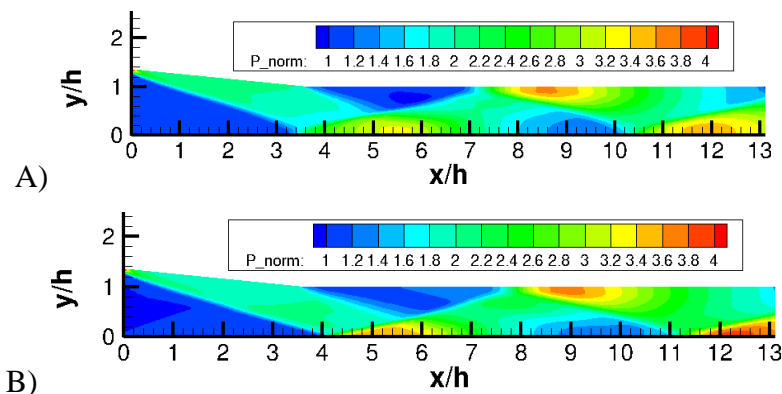


Fig. 5.3 2D Fully Started Flow Pressure A) Thick BL, B) Thin BL

The surface pressure along the top and bottom walls of the inlet-isolator test section reveals the same disparity between the thick and thin boundary layer cases. Fig. 5.4 shows that wall pressures for the thick, thin, and experimental cases. In the thin boundary layer case, the peak values of pressure increase, indicating a larger shock strength, and the peaks in pressure shift slightly downstream. The pressure peaks along the bottom floor in particular show a significant increase, with the reduced boundary layer thickness, while the peak along the channel ceiling only slightly increases in strength, as would be expected because the ceiling boundary layer thickness is the same as before. Still, the peak pressure values do not change too drastically, remaining near the experimental values. This indicates that the major change in the flow field when the boundary layer thickness is reduced occurs within the core of the flow.

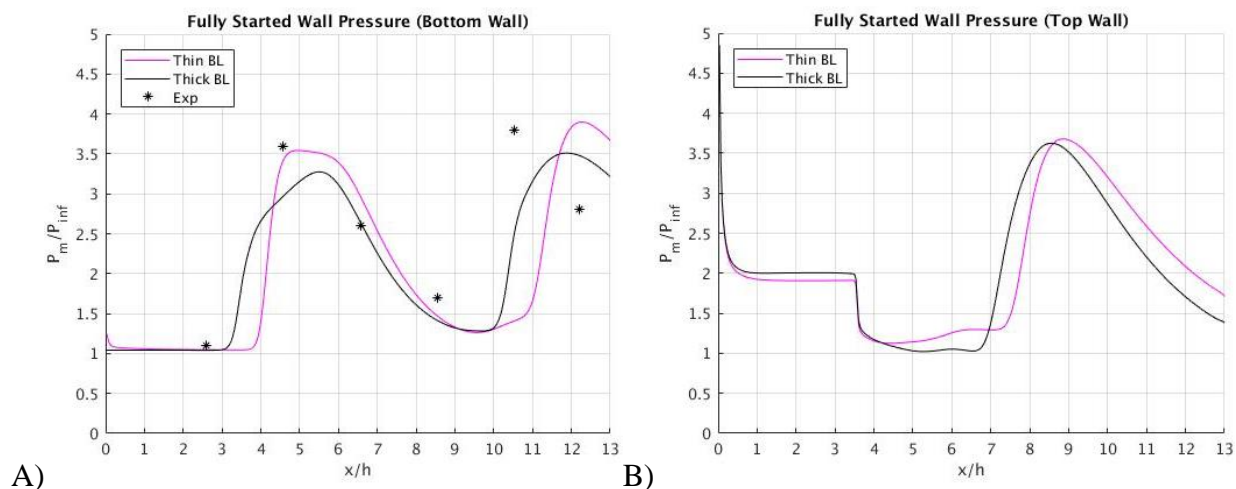


Fig. 5.4 2D Thin BL Fully Started Flow Wall Pressure on Channel A) Floor, B) Ceiling

5.1.2 2D Thin Boundary Layer Unstart

The next step is to look at unstart in the thin boundary layer configuration. The body force source term used for the previous 2D cases was used to disrupt the flow at the isolator exit and initiate unstart. Fig. 5.5 shows the normalized pressure during unstart. Unstart has similar behavior through the isolator but differs in the inlet portion of the test section. Unlike in the thick boundary layer case, it does not slow down or change shape at this point. This implies that the change in unstart behavior, specifically the shape of the shock and the speed of unstart progression, at the inlet was due to the thick boundary layer at that point rather than the increased area from the inlet ramp.

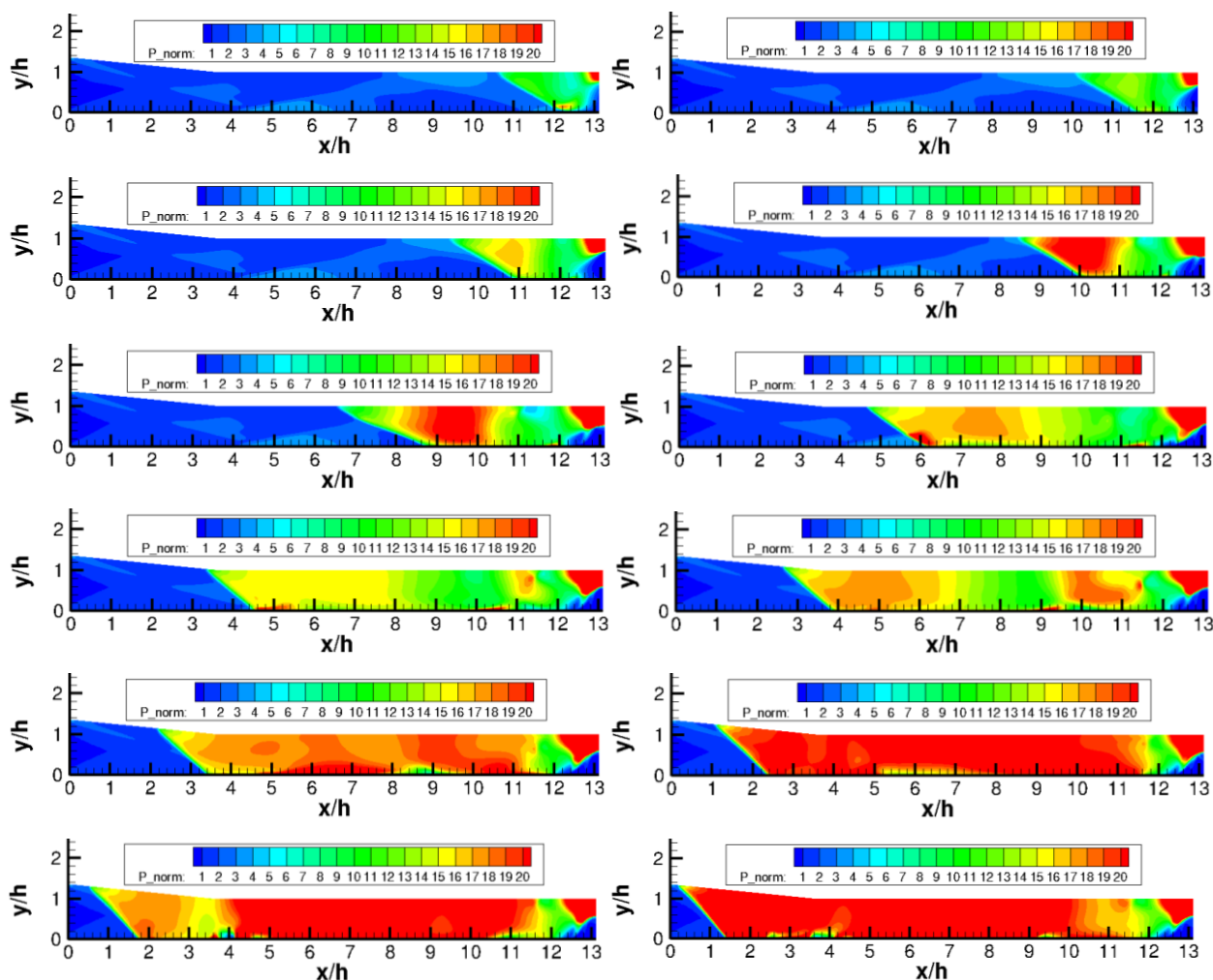


Fig. 5.5 2D Thin BL Unstart at $t = [0.25, 0.5, 0.75, \dots, 3]$ ms

The same pulsing behavior of the normalized pressure within the unstart shock system can be seen in the thin boundary layer case, above, as was seen in Chapter 3. However, the pulses of pressure are stronger, exhibiting higher peak pressures and lasting longer than in the thick boundary layer case. This follows from the stronger shocks of the oblique shock train inducing a stronger response in the unstart region when they intersect with the unstart leading edge.

The unstart speed throughout the channel is plotted in Fig. 5.6, showing another difference between the thick and thin boundary layer cases. On average, unstart moves slightly faster in the thin boundary layer case, at 0.1392 along the ceiling of the channel and at 0.1374 along the channel floor, as opposed to 0.1252 for the ceiling and 0.1292 for the floor in the thick boundary layer case. Although neither of these values are close to experiment, they can be used to predict that the thicker boundary layer and the corresponding weaker oblique shocks, act to slow the progression of unstart in the channel.

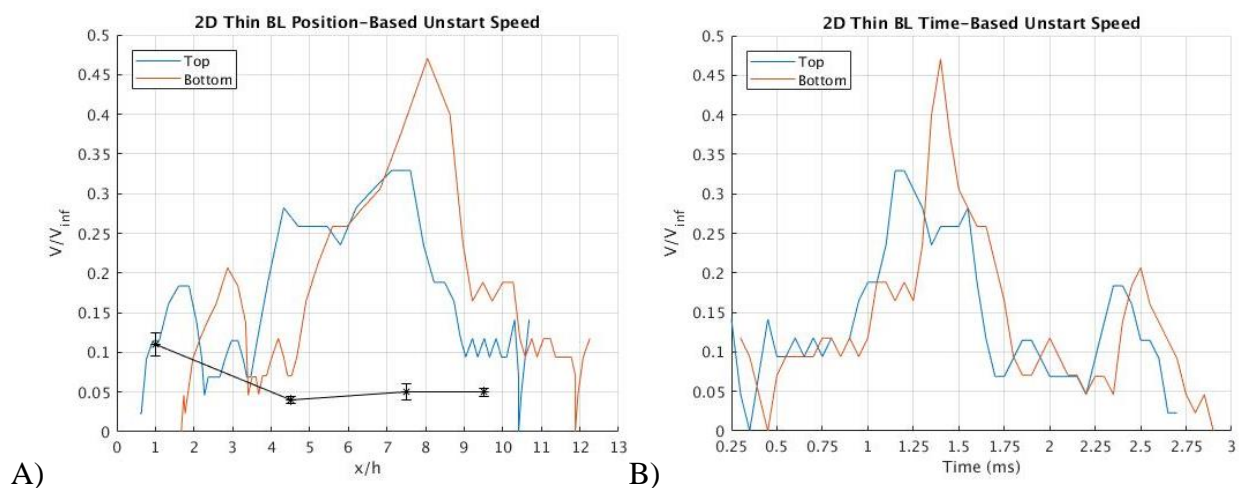


Fig. 5.6 2D Thin BL Unstart Speed vs A) Position, B) Time

Unstart shock arrival time in the 2D Thin BL case is very similar to that seen in the 2D Thick BL case. Fig. 5.7 tracks the time that the shock leading edge of unstart reaches both the top and bottom walls of the channel. Like the other 2D case, unstart is seen almost simultaneously on both the channel ceiling and floor. The shock angle is also similar, and the lines trend towards converging towards the end of unstart. This projected convergence is triggered by the entrance of the shock into the inlet section of the model.

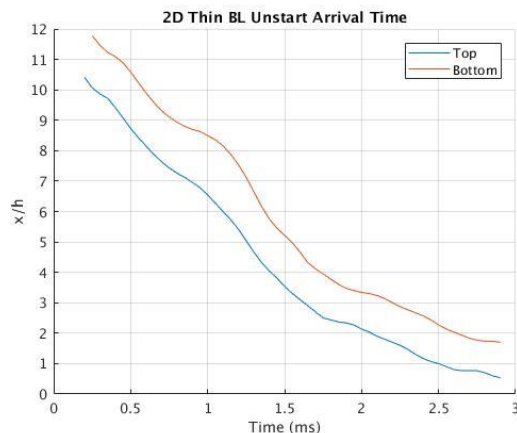


Fig. 5.7 2D Thin BL Unstart Shock Arrival Time

The Mach number within the channel during unstart also helps pinpoint the major differences and similarities between the two flows. In the thin boundary layer case, shown in Fig. 5.8, the large area of subsonic flow within the unstart region trends slower than in the thick boundary layer case. The large bubble-like structure of supersonic flow within the subsonic unstart region dissipates much more quickly in the thin boundary layer case. This discrepancy between the two cases is likely due to the higher Mach number of the core flow in the thin boundary layer case, which may serve to reduce the upstream flow speed in the unstart region. It appears to be insufficient to substantially change the shock propagation speed, but it may have an effect past the shock, within the region downstream of the unstart shock.

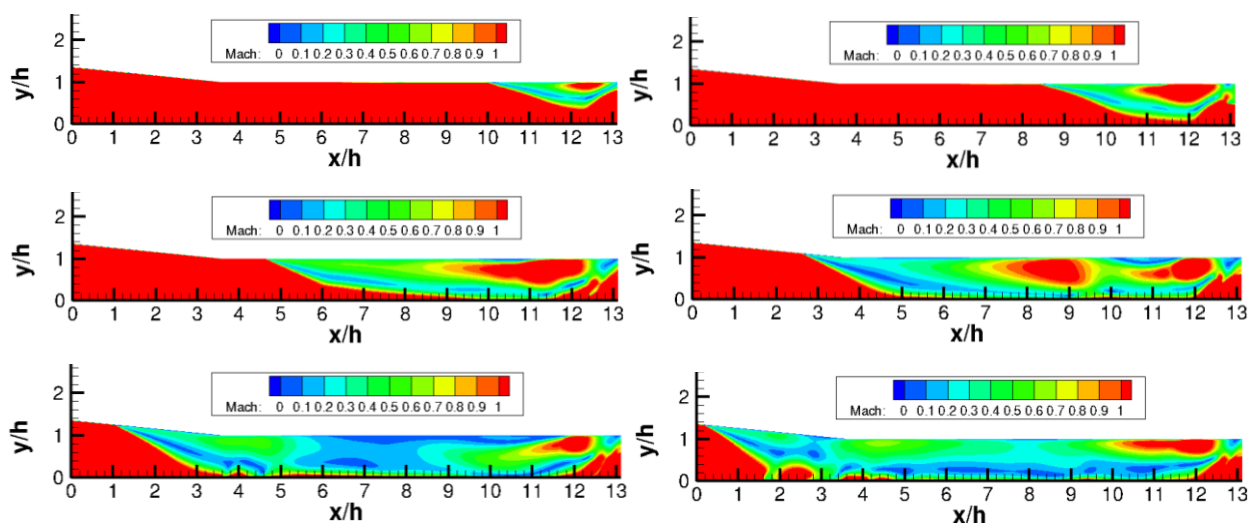


Fig. 5.8 2D Thin BL Subsonic Flow Regions during Unstart at $t = [0.5, 1.0, 1.5, \dots, 3.0]$ ms

Fig. 5.9 shows the pressure along the top and bottom walls of the channel during unstart. On the whole, the wall pressure looks roughly equivalent to that seen in the thick boundary layer case. The normalized pressure on the top surface of the channel remains around 20 throughout the unstart process and stays relatively constant, except for a spike at the outlet. Alternatively, the bottom surface pressure is highly dynamic, with a moving peak that maintains a normalized pressure of around 80. These wall pressure values are similar to what was seen in the thick boundary layer case, but with a reduction in the variations of pressure along the bottom wall.

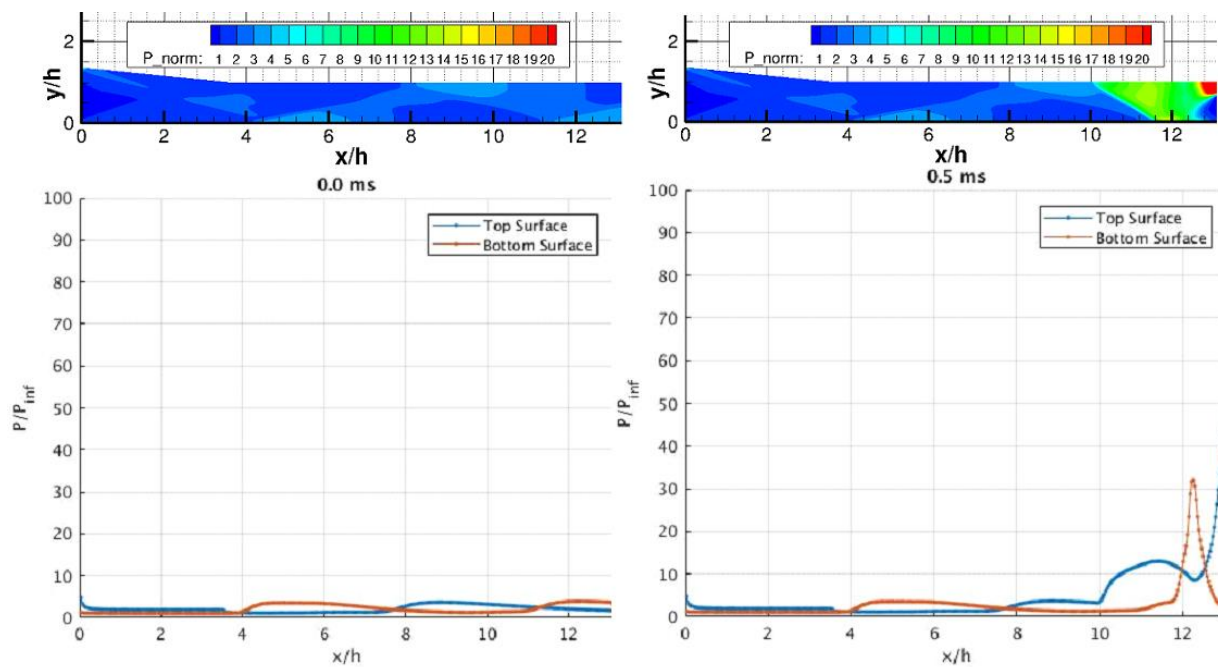
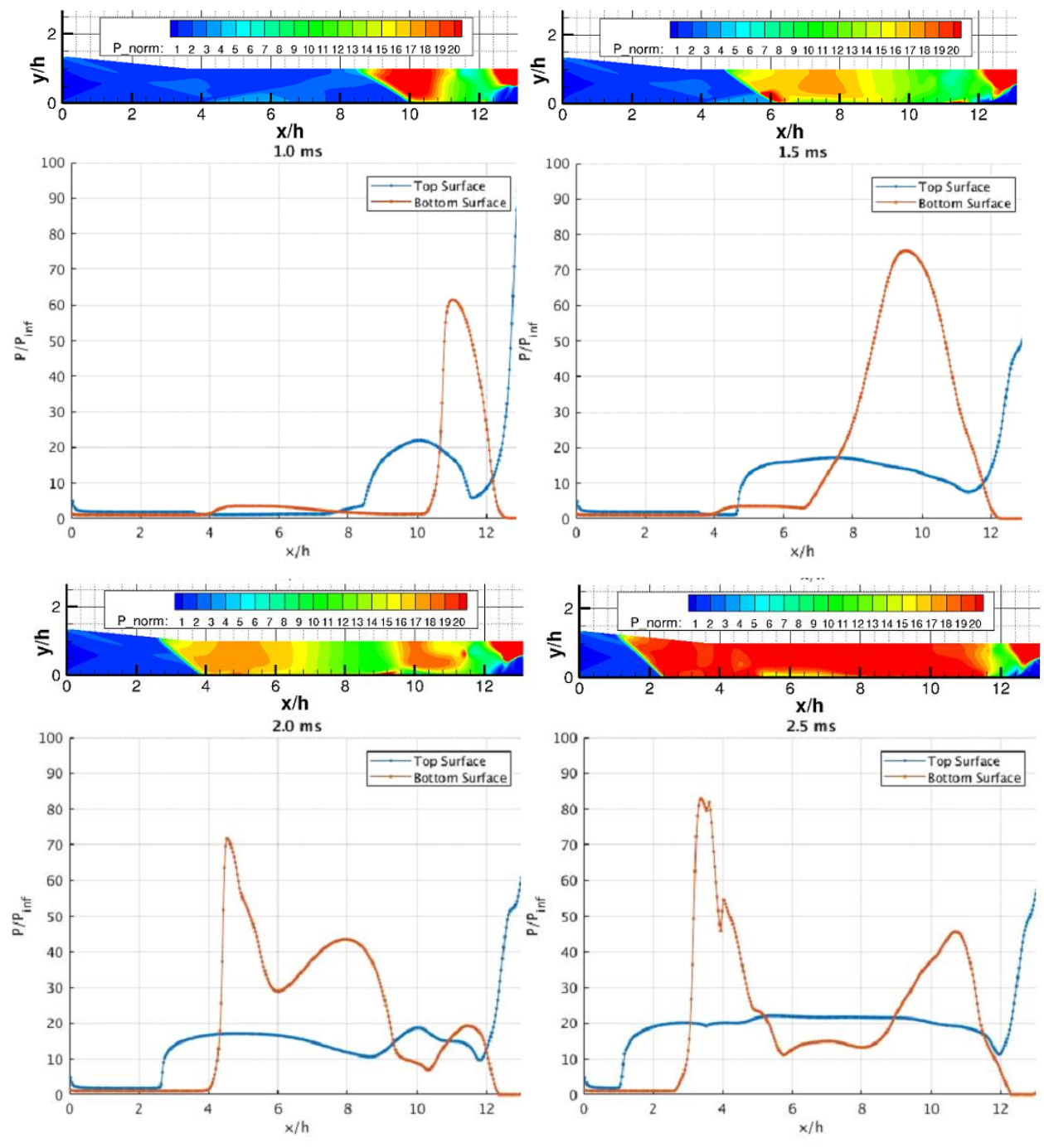


Fig. 5.9 2D Thin BL Wall Pressure during Unstart

Fig 5.9 continued



Examining the peak pressures as before, we see the same pressure pulsing noted above, albeit with smaller variances when compared to the thick boundary layer case. Fig. 5.10 shows this trend, as well as showing that the pressure is much higher overall without an ingested boundary layer. The peak pressure value grows over time, as unstart progresses upstream.

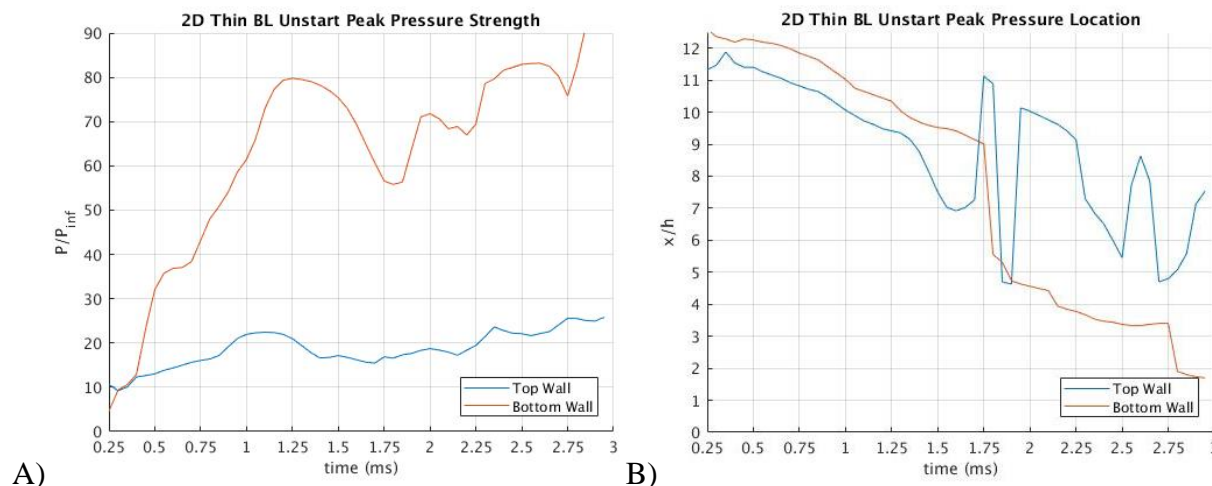


Fig. 5.10 2D Thin BL Wall Peak Pressure A) Strength, B) Location

5.1.3 2D Thin Boundary Layer Unstart Precursors

Finally, looking for unstart precursor signals, the identified signals from Chapter 3 have shifted position to remain at the oblique shock impingement points. This further indicates that their locations are indeed determined by the shock train position and are not some artifact of the geometry. Fig. 5.11 shows the normalized wall pressure difference at six different time steps during unstart for the thin boundary layer case. The precursor pressure signals now appear to have moved, relative to the thick boundary layer case, from $x/h = [4.1, 7.8, 11.2]$ to $x/h = [5.7, 8.0, 11.2]$. While this change is relatively minor, a more significant change occurs as well. The strength of the unstart precursors, in terms of normalized pressure, has dropped by an order of magnitude.

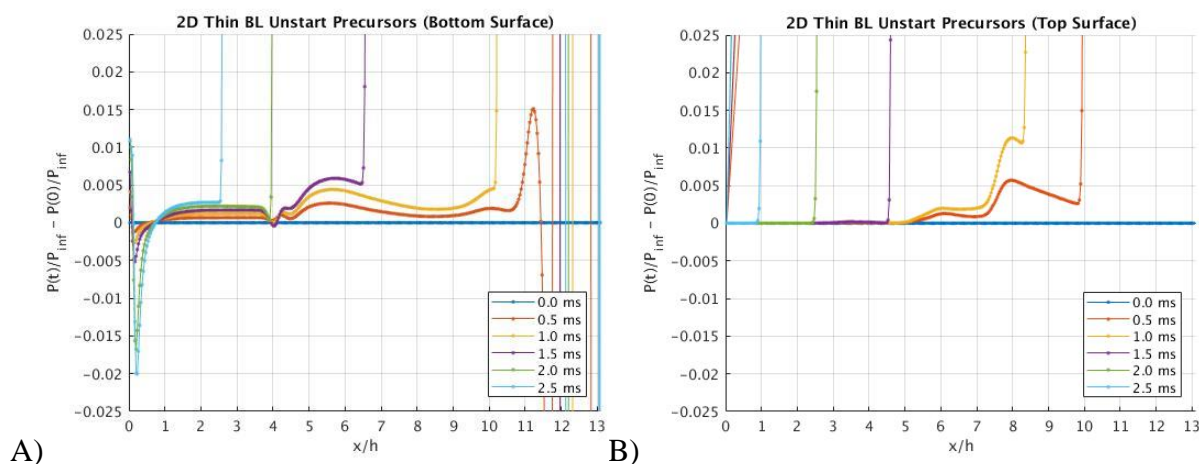


Fig. 5.11 2D Thin BL Unstart Precursor Signal on Channel A) Bottom, B) Top

The whole spread of pressure readings, at every time step during unstart, helps illuminate the precursor strength difference. Fig. 5.12 shows the precursor signals growing over time during unstart, but remaining roughly ten times weaker than in the thick boundary layer case. This implies that the signal of unstart is able to travel better and more robustly through a thick boundary layer. In addition, the strength is highly tied to the boundary layer thickness. Now, with this thinner boundary layer, the pressure difference for the unstart precursor signal reaches a maximum of 0.02 times the normalized pressure. The means that the signal strength has been reduced from roughly 1 kPa to around 100 Pa, which will be much harder to detect.

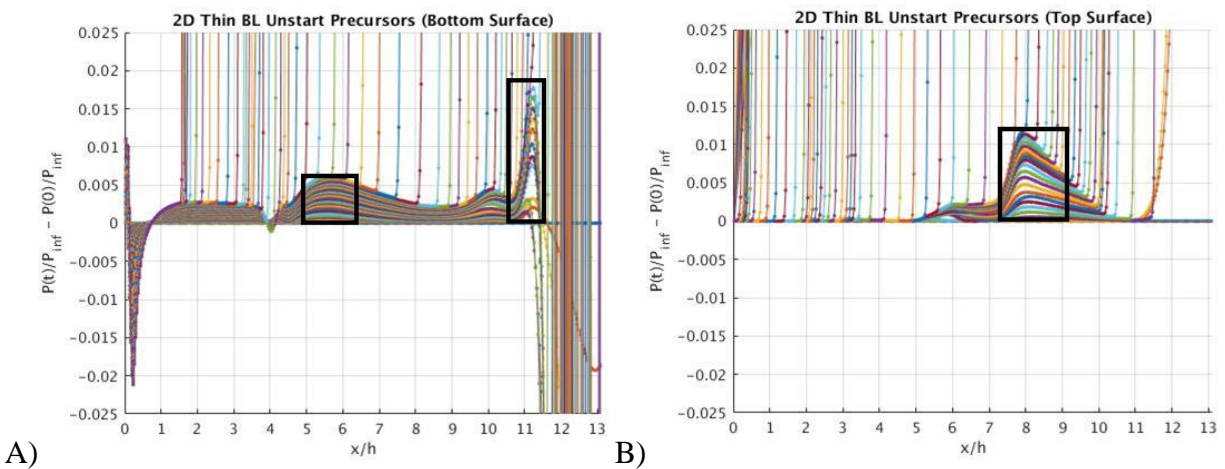


Fig. 5.12 2D Thin BL Unstart Precursor Signal (all time) on Channel A) Bottom, B) Top

Cataloguing the differences between unstart in the inlet-isolator for thick and thin boundary layers, it becomes clear that a thicker boundary layer entering the system inlet is better in terms of detecting unstart by monitoring for precursor signals. A thicker boundary layer reduces the speed of unstart, giving a system more time to respond and giving the precursor signals more time to grow. In addition, it reduces the pressure forces within the unstart system, meaning less stresses on the vehicle. Finally, unstart precursors are much weaker in the thin boundary layer situation, meaning unstart will be much more difficult to detect. Thus, unstart should be easier to detect in the presence of a thick boundary layer.

5.1.4 3D Thin Boundary Layer Fully Started Flow

The next step to verify the conclusions in the previous section is to reproduce the thin boundary layer computations in 3D. As before, the same inflow conditions were used, minus the imposed thick boundary layer, and the inlet-isolator flow field was run to steady state convergence. This will enable us to understand how the 3D effects interact with the boundary layer effects in terms of shock placement, shock strength, and unstart behavior.

First, a pseudo-Schlieren image of the inlet-isolator channel was created from the fully started flow configuration. Fig. 5.13 shows the results for a thin boundary layer flow in the 3D channel, along a slice on the z centerline. Each oblique shock is labeled using the same nomenclature as before. From these images, it is possible to determine the location of the shock impingement points and see that, like in the 2D computation, they have shifted downstream relative to the thick boundary layer case.

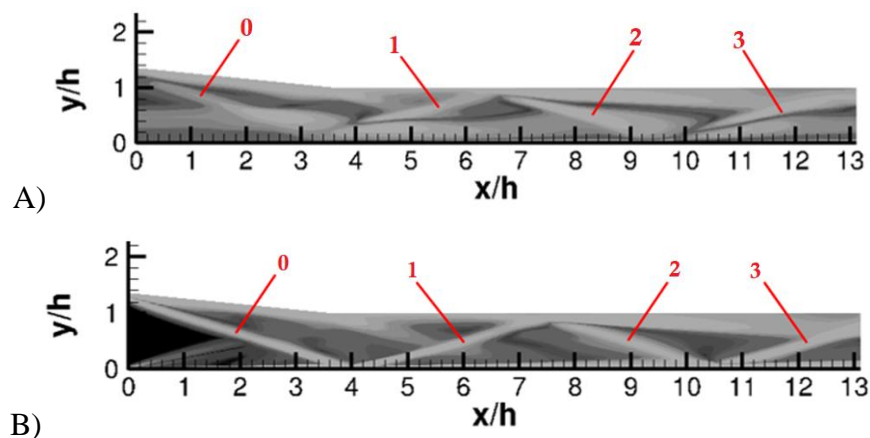


Fig. 5.13 Pseudo-Schlieren Image along Z-Centerline A) 3D Thick BL, B) 3D Thin BL

In the thin boundary layer case, the first oblique shock, 0, is effectively free to deflect at the value predicted by oblique shock relations. This value is approximately 16 degrees, which is seen here. However, for the thick boundary layer case, when the shock wave meets the boundary layer, it curves slightly moving the impingement point upstream.

Next, looking at the density gradient magnitudes along the y centerline slices from the 3D thin and thick boundary layer cases, shown in Fig. 5.14, assists in understanding the reason for this downstream shift of the shocks in the thin boundary layer case. With a thick boundary layer, the

angle of the initial oblique shocks are pushed inward towards the channel center, with a less acute angle. This causes the location that the different shocks intersect at to change.

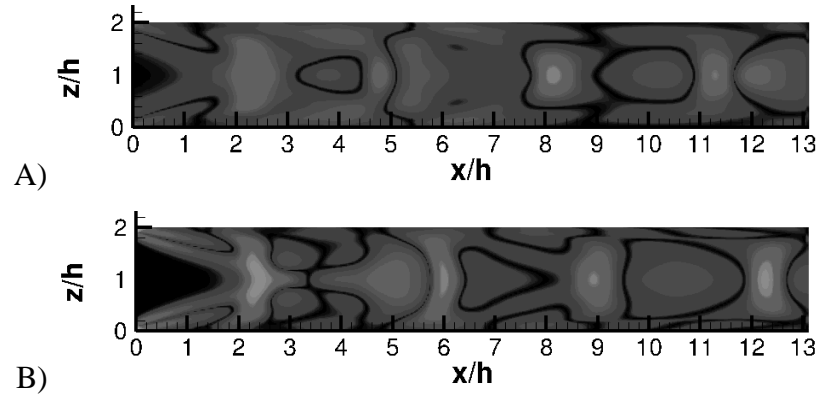


Fig. 5.14 Pseudo-Schlieren Image Y-Centerline A) 3D Thick BL, B) 3D Thin BL

Next, Fig. 5.15 compares the normalized pressure of the 3D channel with the thin thick boundary layer with both the 2D thin boundary layer flow and the 3D thick boundary layer flow. While the same general flow structures are present in all three flow fields, the differences in the magnitude of the pressure variation are quite large.

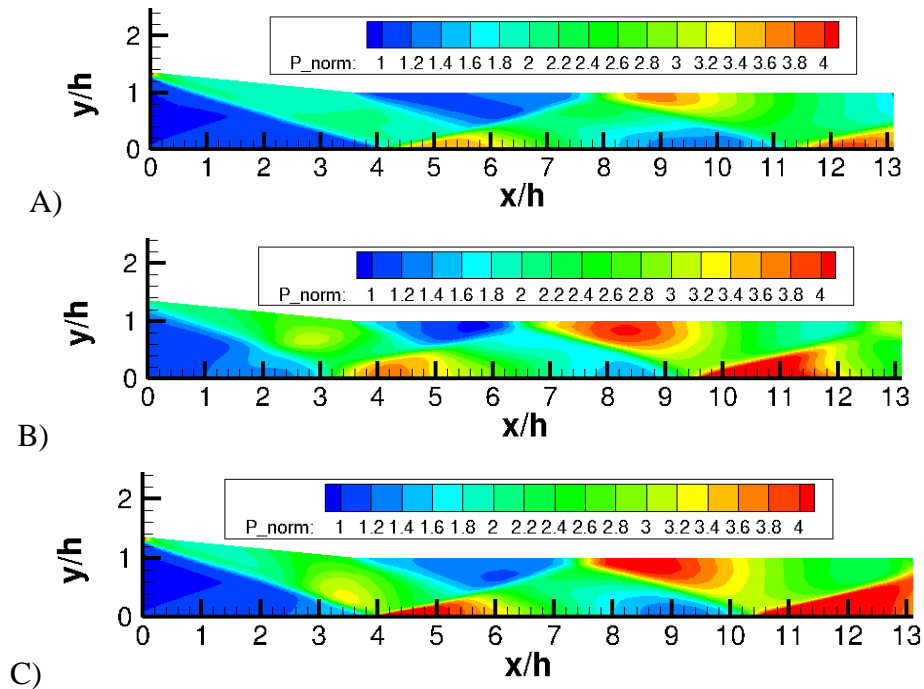


Fig. 5.15 Fully Started Flow Pressure A) 2D Thin BL, B) 3D Thick BL, C) 3D Thin BL

Similar to the 3D thick boundary layer case, the regions of high pressure that exist along the top and bottom walls of the channel, just downstream of the shock impingement points, are larger and of higher pressure than their 2D analogs when there is only a thin boundary layer. When compared to the thick 3D case, the pressures are generally higher and the gradients between low and high pressure regions are sharper and more abrupt, as was seen in the pseudo-Schlieren images.

To develop a better understanding of how the 3D effects are influencing the flow field, a centerline y slice of the channel was extracted, as shown in Fig. 5.16. From these normalized pressure plots, it becomes clear that the pressure strengths and locations of high and low pressure are significantly changed by the modified floor boundary layer thickness. In addition, there is less of the smearing effect seen previously, as the sidewall shocks intersect the core flow further downstream.

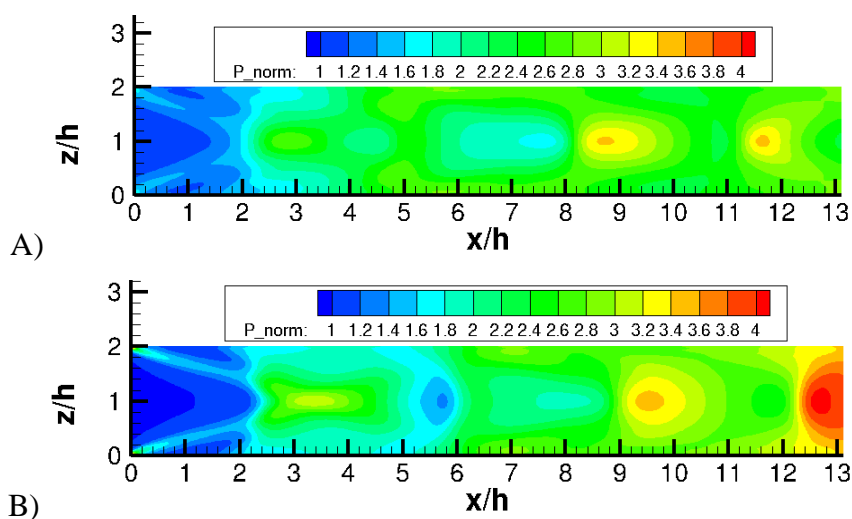


Fig. 5.16 Normalized Y-Plane Fully Started Flow Pressure A) 3D Thick BL, B) 3D Thin BL

Investigating the pressure along the top and bottom surfaces of the channel show a similar trend as was seen in the 2D calculations. Fig. 5.17 compares the two 3D cases, and two major differences can be seen. First, the normalized wall pressure is increased following each oblique shock in the thin boundary layer case. This follows what was seen before and supports the idea that the shocks are weakened by the presence of a thick boundary layer. Second, the shocks shift downstream when only a thin boundary layer is present. The downstream shift of the shock impingement points is roughly the same in the 2D and 3D cases, while the increase in pressure from the thin boundary layer is more pronounced in the 3D case.

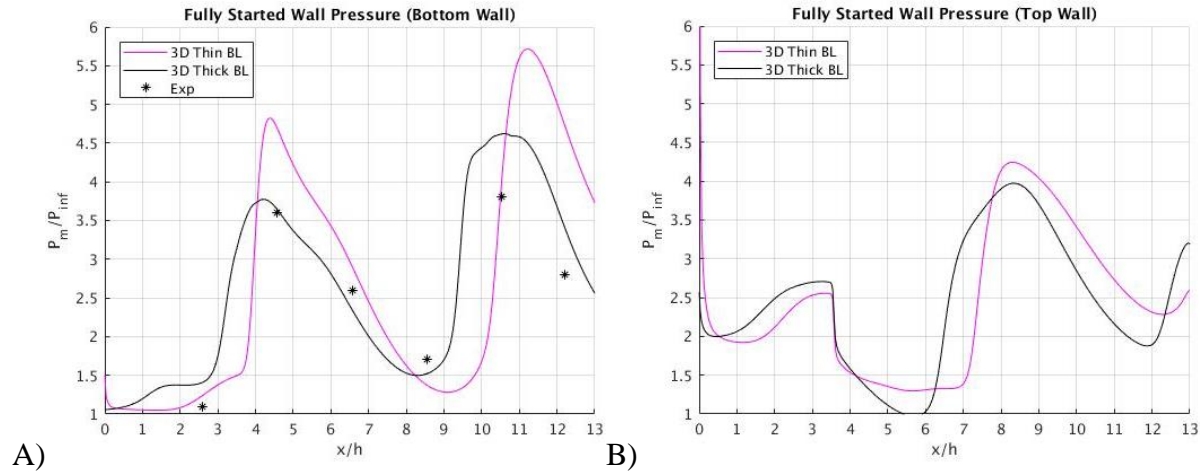


Fig. 5.17 3D Thin BL Fully Started Flow Wall Pressure on Channel A) Floor, B) Ceiling

The flow velocity and Mach number contours detail a more developed view of the flow dynamics in the fully started flow. Fig. 5.18 details u , v , and w , along with M , on the y and z center planes. The flow fields look very similar to the 2D case for the thin boundary layer, except for a few key differences. First, while the supersonic core flow is still much larger and faster than the thick BL case, the flow is actually slower than the 2D case. Moreover, regions of slower flow within the supersonic core flow are more pronounced, with larger regions of relatively slow flow. The flow structures are largely the same except for the strength, in this 3D case as in the 2D case, towards the upstream/inlet side of the channel. However, as the flow progresses downstream, it diverges more and more from the 2D case, failing to exhibit some of the high speed flow bubbles as seen in the 2D case and generally having less energy in the flow. The same trends seen in the thin and thick BL cases, whether they are 2D or 3D appear to hold.

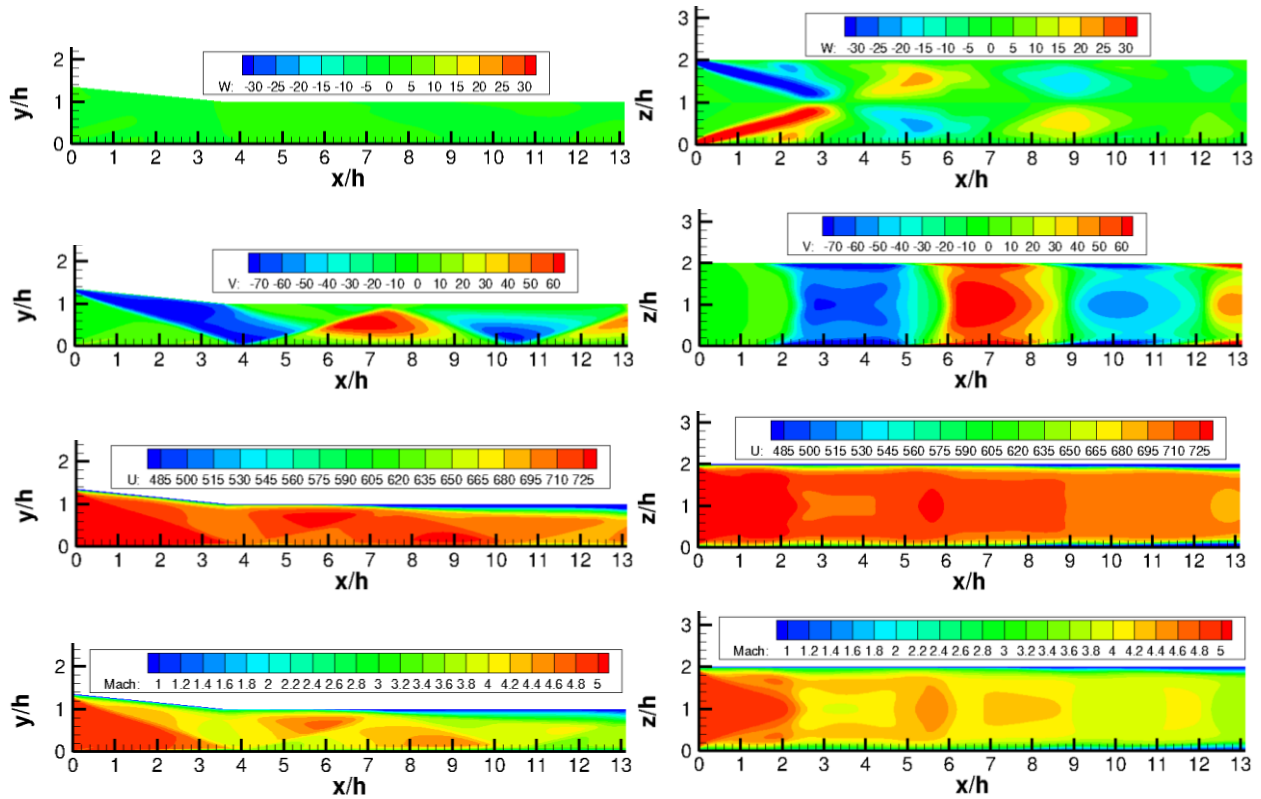


Fig. 5.18 3D Thin BL Velocity Field for Z Centerline (L) and Y Centerline (R)

5.1.5 3D Thin Boundary Layer Unstart

The differences in the 3D and 2D steady flows, with a thin boundary layer, while notable are not the most significant change that takes place. The real test of the difference comes with simulating unstart. Fig. 5.19 showcases the normalized pressure through the channel during the unstart process. It is immediately clear that the pressures exhibited in the 3D flow are significantly higher than those seen in the 2D thin BL case and in the 3D thick BL case. The pressure pulse are more sustained and unstart appears to occur much more rapidly. One major difference from the thick boundary layer case is the sidewalls shocks remain consistently ahead of the centerline shock throughout the entire unstart process.

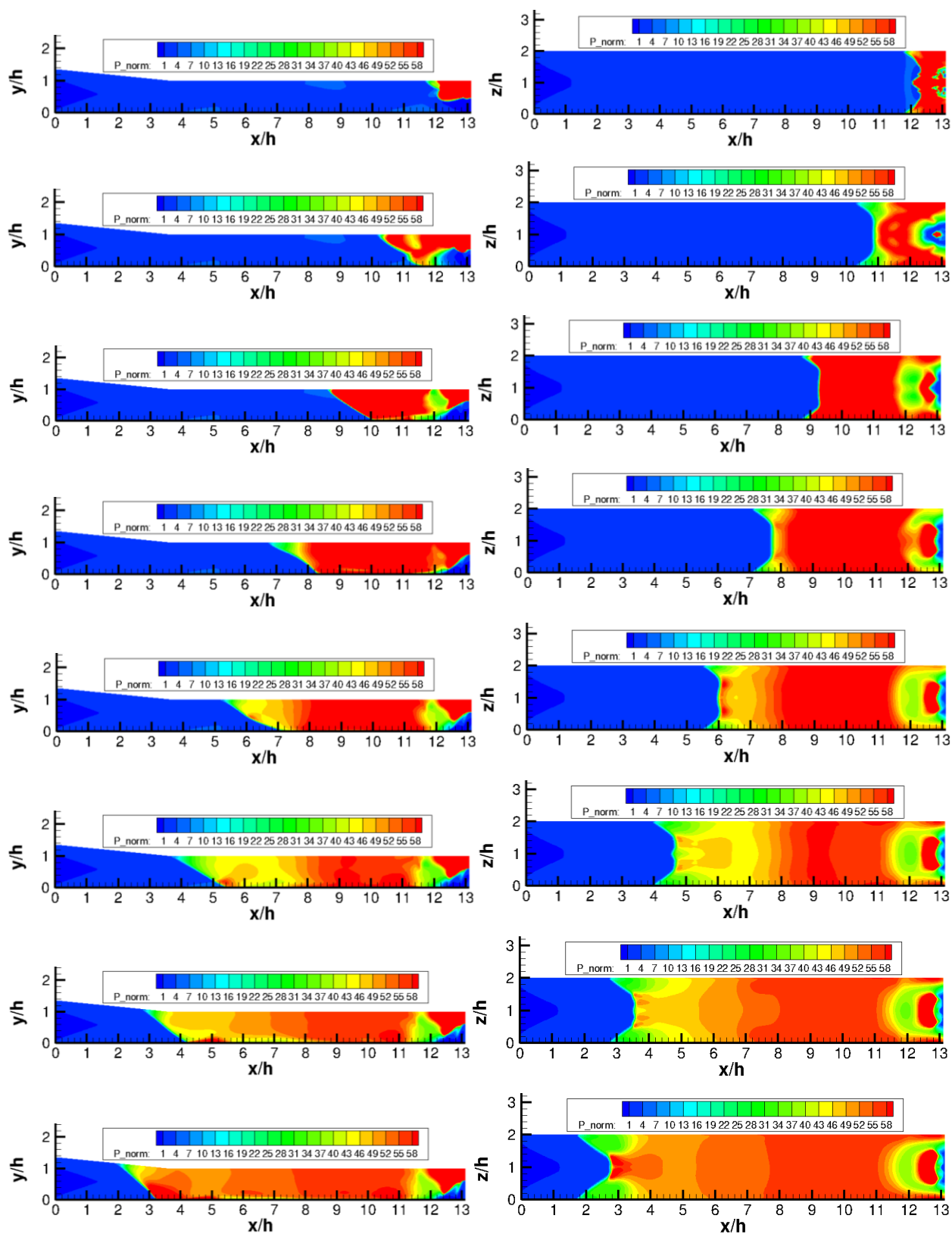
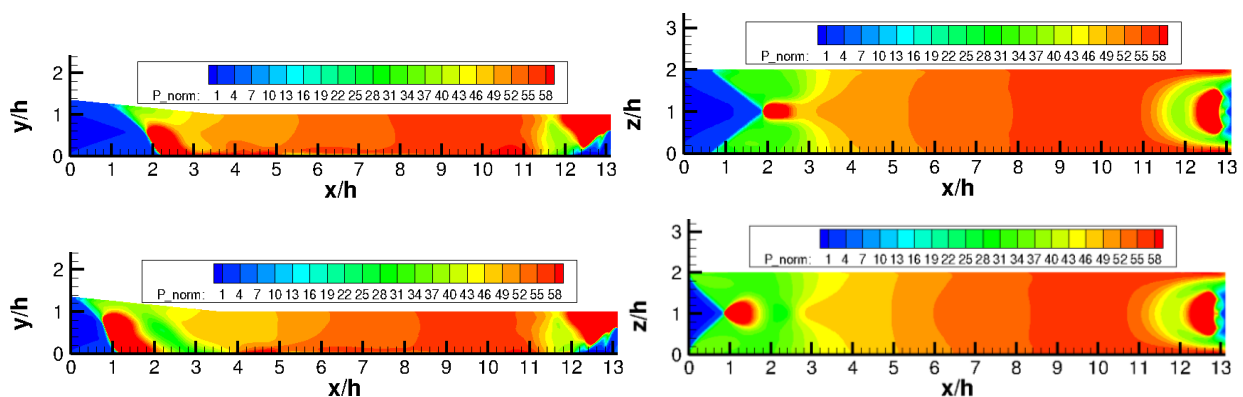


Fig. 5.19 3D Thin BL Unstart Pressure at $t = [0.05, 0.10, 0.15, \dots, 0.50]$ ms

Fig 5.19 continued



Looking at how unstart speed changes between the thick and thin 3D cases is important as well. Fig. 5.20 shows how the speed of unstart changes over the course of unstart, both through the channel and over time. The mean normalized unstart speed along the top wall of the channel is 0.9021, while it is 0.8411 along the bottom wall. This is approximately 6.5 times the speed of unstart in the 2D case with no boundary layer, and approximately 14 times the speed seen in experiment. This follows the same jump from 2D to 3D as seen before, and compares to the 3D case with a thick boundary layer in a similar way with a small increase in speed. Recalling that the 3D thick BL case saw unstart speeds of 0.9257 and 0.7798 along the top and bottom walls, it is clear that, in both 2D and 3D, the thin BL case leads to faster average unstart of the system.

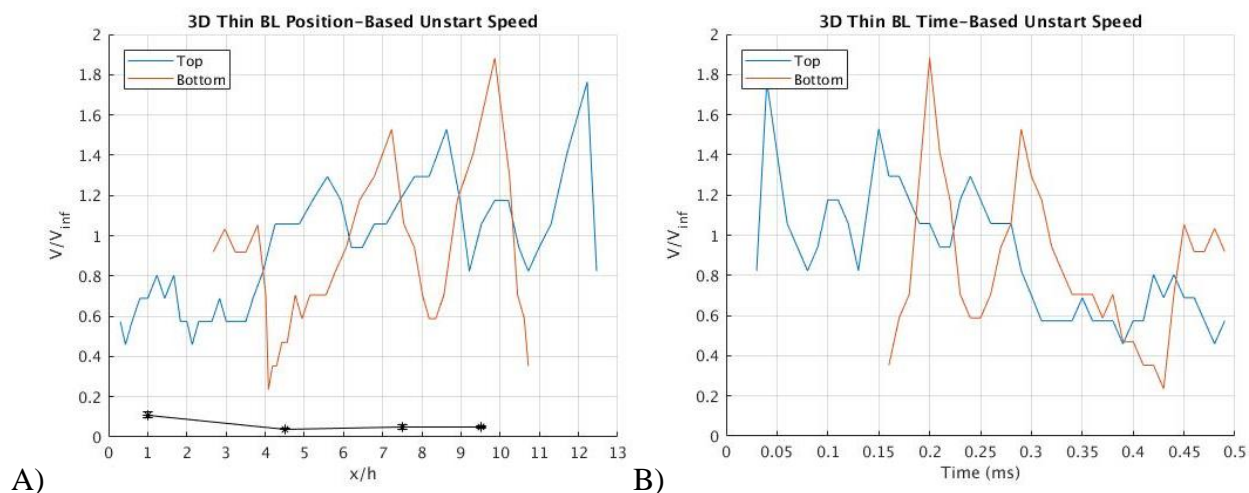


Fig. 5.20 3D Thin BL Unstart Speed vs A) Position, B) Time

The unstart shock arrival time, presented in Fig. 5.21, shows a similar trend to the 3D Thick BL case, except the two plotted lines fall closer together, indicating the shock in the channel floor lags less in the thin boundary layer case. In addition the lines diverge near the inlet, as seen in the two 2D cases, indicating a change in the leading edge shock angle.

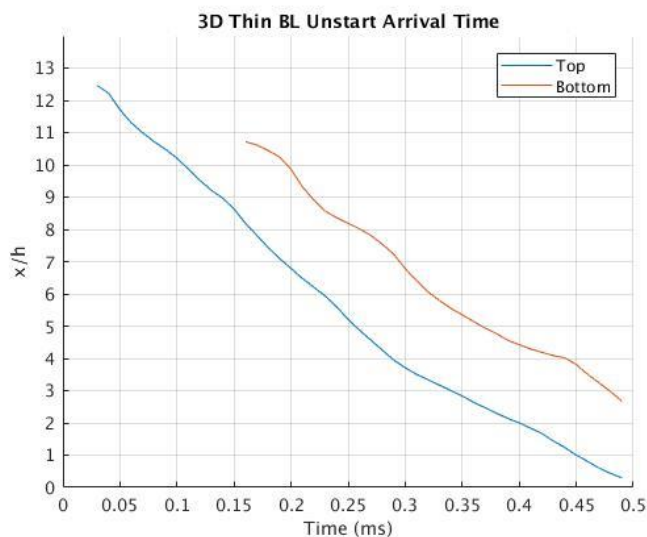


Fig. 5.21 3D Thin BL Unstart Shock Arrival Time

Fig. 5.22 examines the change in Mach number in the channel during unstart. Like in the 2D thin BL case, the regions of high Mach flow that develop within the unstart region dissipate much faster. So much so, in fact, that there exists only a small accelerated region of the flow at the leading edge of unstart that dissipates before it develops into a larger disruption of the flow. Comparing to the 3D thick BL case, the stagnation region near the top wall of the channel is much smaller in this case. In addition, the response time of the bottom wall to unstart is much shorter, leading to less of a delay between high pressures in the flow and high pressures seen along at the surface.

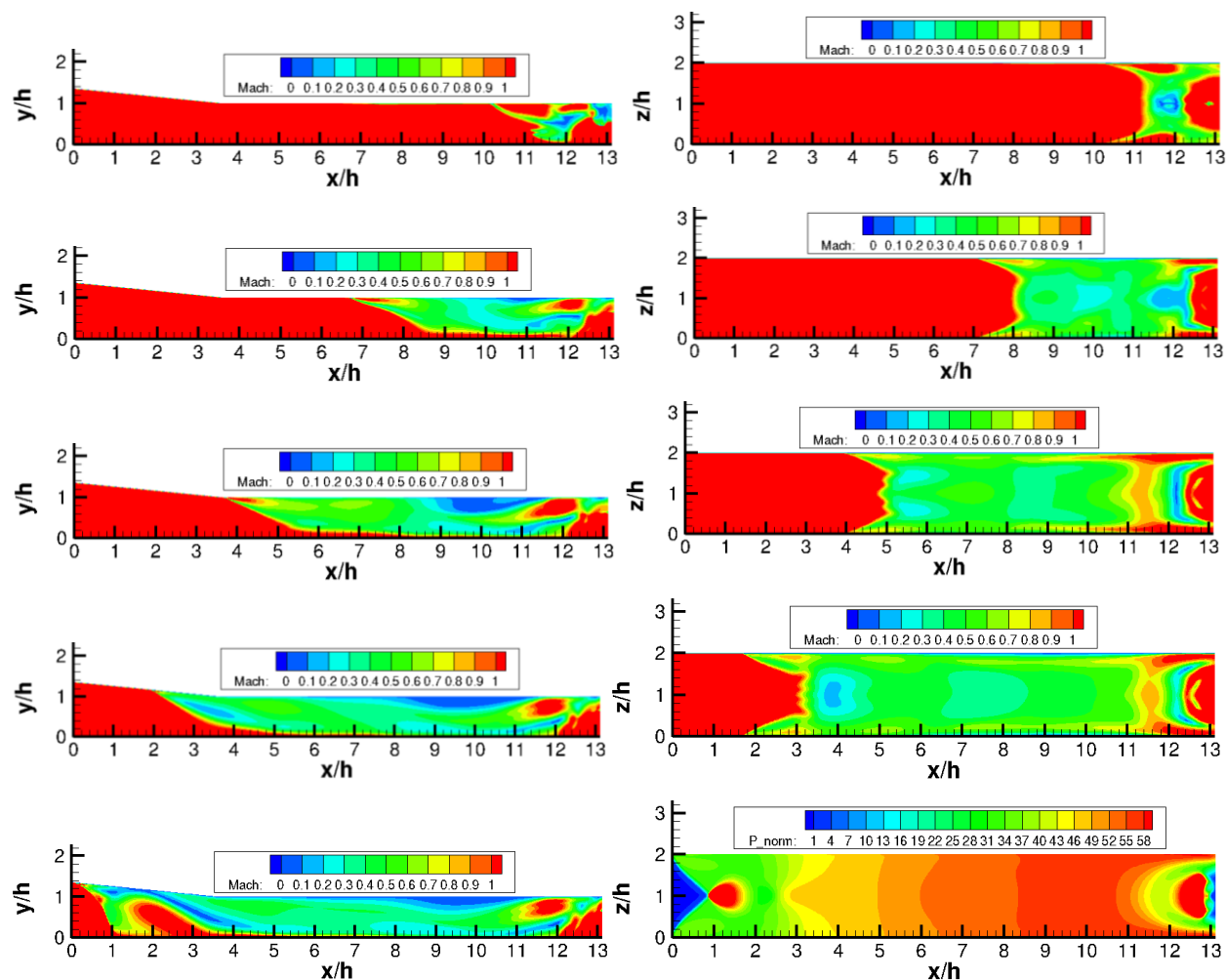


Fig. 5.22 3D Thin BL Unstart Mach Number at $t = [0.1, 0.2, 0.3, \dots, 0.5]$ ms

5.1.6 3D Thin Boundary Layer Unstart Precursors

Delving further to examine the unstart precursor signals previously identified, Fig. 5.23 displays the wall pressure at selected time steps during unstart for the 3D thin boundary layer case. As with the 2D to 3D change with the thick boundary layer case, the pressures seen are significantly higher. However, they do not grow as much in comparison to the 2D case as does the thick boundary layer solution. However, the top surface again sees relatively steady pressure values and the bottom surface sees a high degree of variability in pressure. This similar behavior to the thick boundary layer case indicates that the contrast between the pressure seen by the two walls is more of a function of the sudden disruption (source term/flap) than of the boundary layer thickness. Furthermore, due to the faster response time of the wall pressure in the floor boundary

layer, the bimodal distribution of pressure seen in the 3D thick BL case is basically eliminated and much higher pressures are seen along the wall.

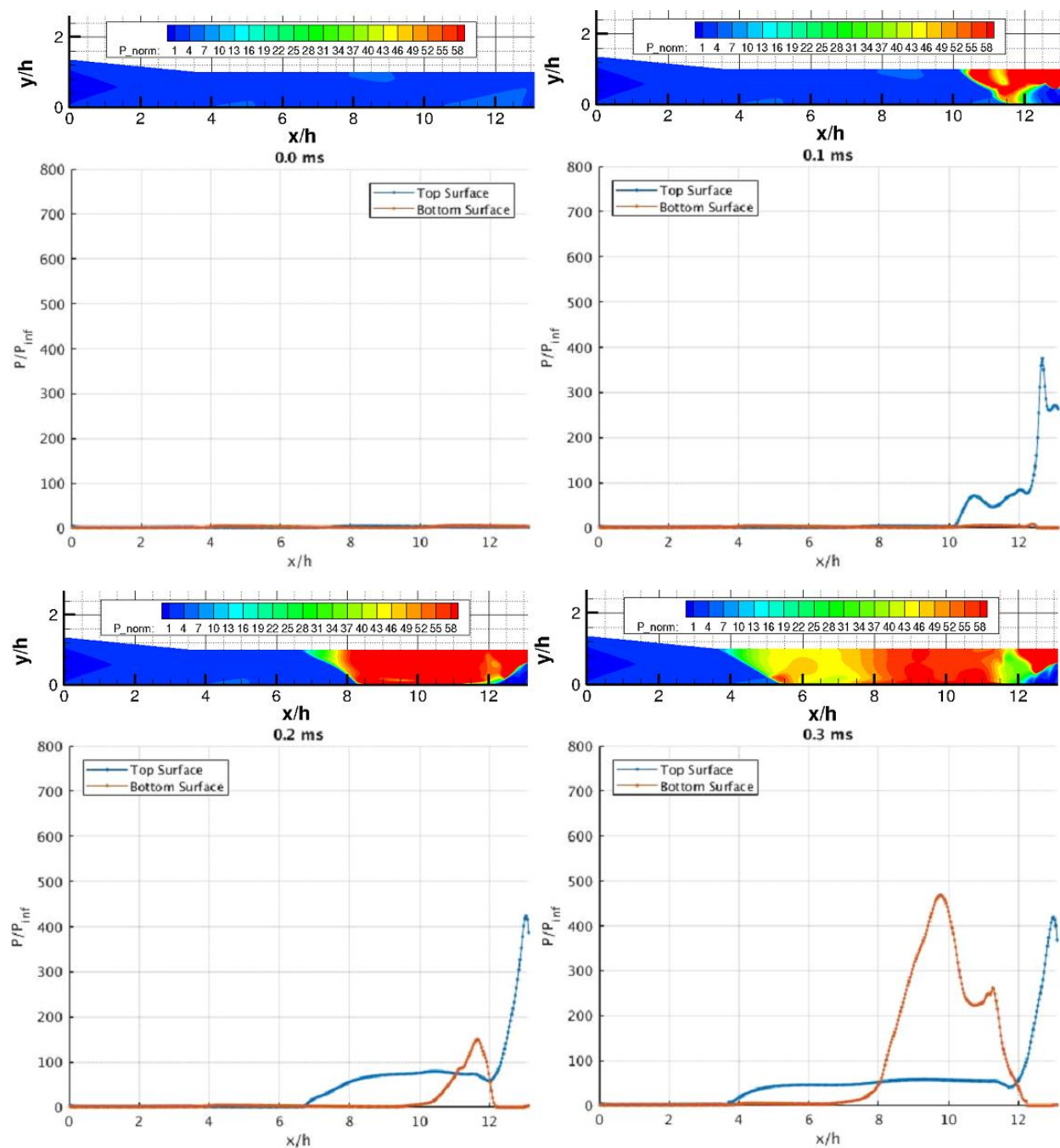


Fig. 5.23 3D Thin BL Wall Pressure Traces during Unstart at $t = [0.0, 0.1, 0.2, \dots, 0.5]$ ms

Fig 5.23 continued

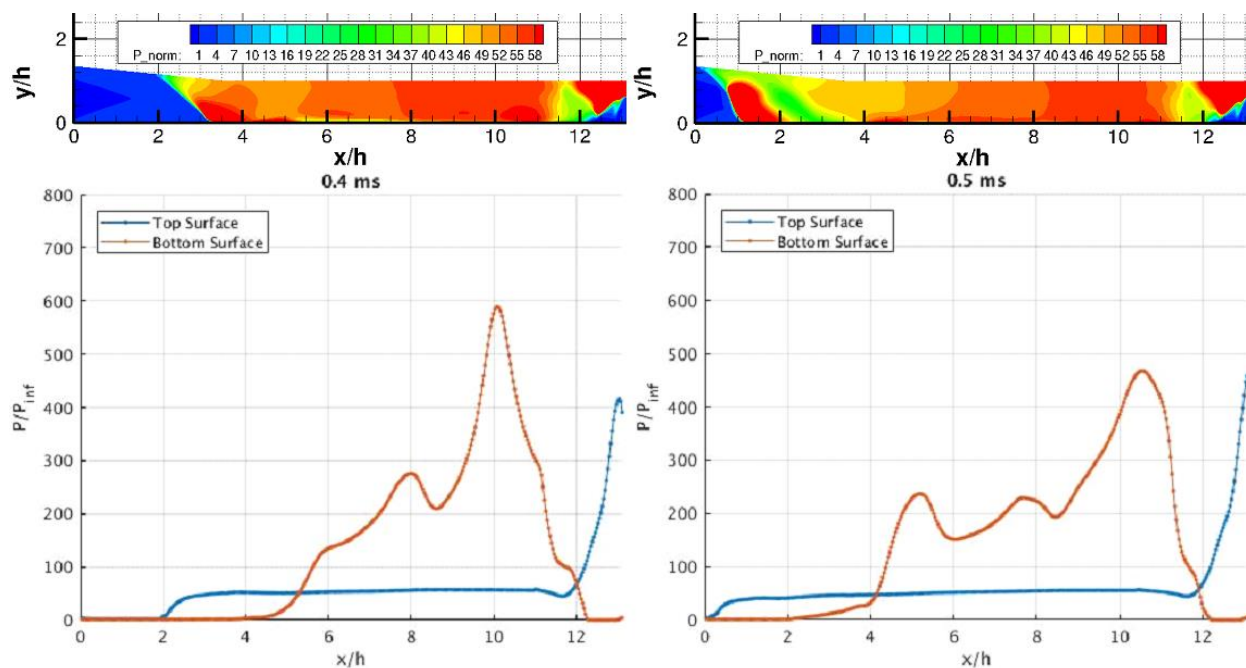


Fig. 5.24 showcases the peak pressure during unstart and a surprising trend can be observed. First, there is less pulsing of the pressure value as unstart passes through the shock train. Second, the peak pressure along the top wall decreases over the course of unstart. This is quite different from the behavior of the top wall and of the case with a thick boundary layer. Third, the pressure on the bottom wall grows much larger than in the other cases, with a large spike that tapers off in strength towards the end of the process.

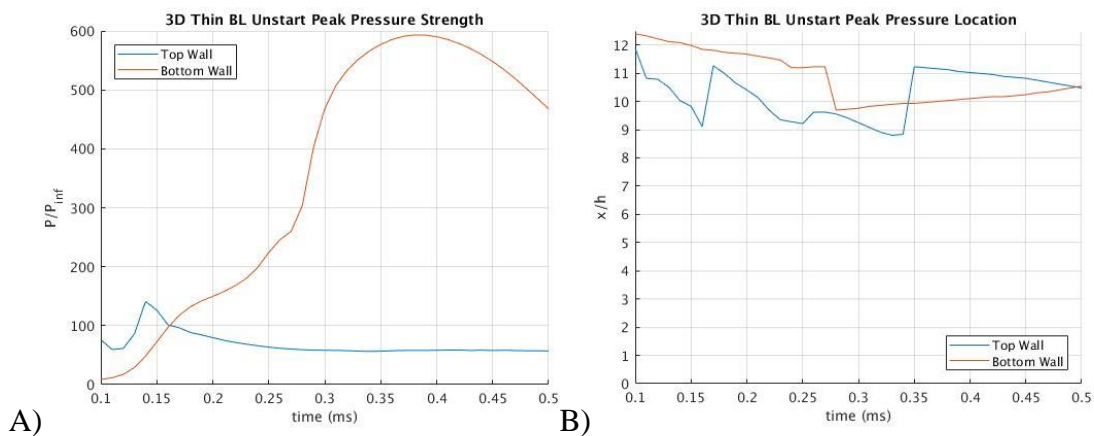


Fig. 5.24 3D Thin BL Wall Peak Pressure A) Strength, B) Location

As was seen with the thick boundary layer case, the precursor signal strength increases in the 3D case. However, the lack of a thick boundary layer counteracts this by reducing the signal strength, as was seen in the 2D thin boundary layer simulation. Thus, the same sign change in the first signal along the bottom surface is seen, as is the elimination of the first signal along the top wall, as was seen in the 3D thick BL case. And although the 3D signals are amplified compared to the 2D ones, the thin boundary layer more than makes up for this and reduces the strength below that of the 2D thick BL case. Fig. 5.25 shows the precursor across selected time steps and Fig. 5.26 shows the strength over all time.

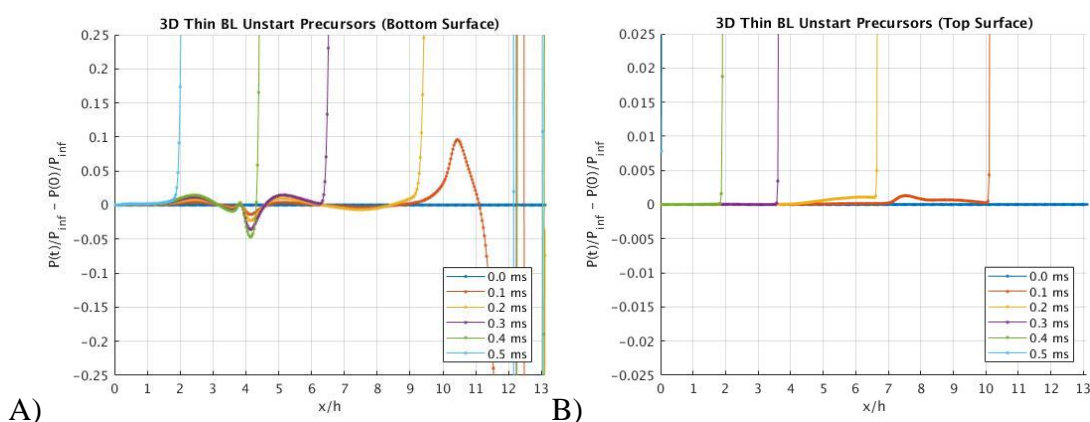


Fig. 5.25 3D Thin BL Unstart Precursor Signal on Channel A) Bottom, B) Top

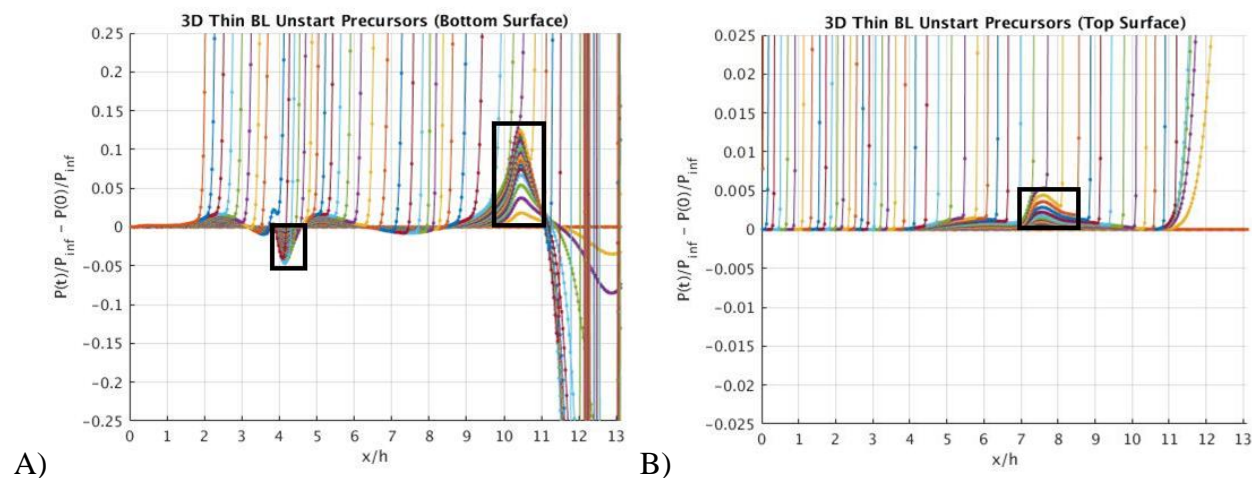


Fig. 5.26 3D Thin BL Unstart Precursor Signal (all time) on Channel A) Bottom, B) Top

5.2 Aspect Ratio Effects

Isolator geometry plays a major role in unstart dynamics and the flow properties of a fluid in the hypersonic regime. Sridhar and Thanigaiarasu [48] investigated an isolator shape transition from rectangular to circular. They found that changing the geometry in that way shifted the oblique shock train downstream and reduced its overall length. Aspect ratio can also have a large influence on the flow properties. It is assumed that corner vortices and other 3D effects will be reduced in an inlet-isolator channel that has a high width to height aspect ratio (AR). The experimental channel investigated in this paper had an aspect ratio of 2, with a channel width of 50.8 mm and a height of 25.4 mm. In order to determine the extent to which this design plays a role in unstart, it is investigated in this section. To accomplish this, an inlet-isolator channel with the same height, 25.4 mm, but a halved width (now also 25.4 mm) was created. In this section, the terms High AR and Low AR will be used to refer to the experimental design with $AR = 2$ and a modified version developed for this section with $AR = 1$, respectively. Both cases examined in this section feature the thick boundary layer as seen in experiment.

5.2.1 Narrow Channel Fully Started Flow

The first step is again to develop a fully started flow with the Low AR grid. Fig. 5.27 displays the z centerline density gradient magnitudes, or pseudo-Schlieren view, of the Low AR and High AR channels, in the fully started flow state. It is immediately clear that there are major differences in the two flows. Most prominently, the oblique shock train is much shorter in the Low AR channel, with only two shocks. The strength of the shocks is greatly reduced and the smearing of the shocks from the sidewall shocks is much more pronounced with the narrower channel.

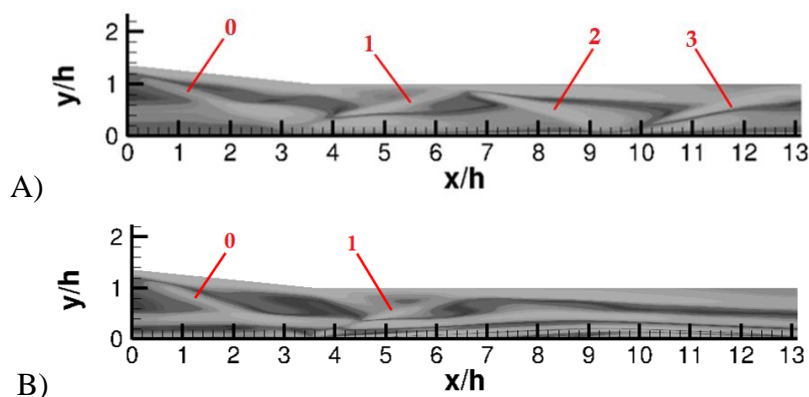


Fig. 5.27 Pseudo-Schlieren Image on Z-Centerline A) 3D High AR, B) 3D Low AR

Looking at the y centerline, in the xz plane, the pseudo-Schlieren images in Fig. 5.28 show that the shock train has compressed, with the major shock structures shifting upstream, when the aspect ratio is reduced. It is likely that the thick ingested boundary layer along the channel floor has an outsized effect within the Low AR channel geometry.

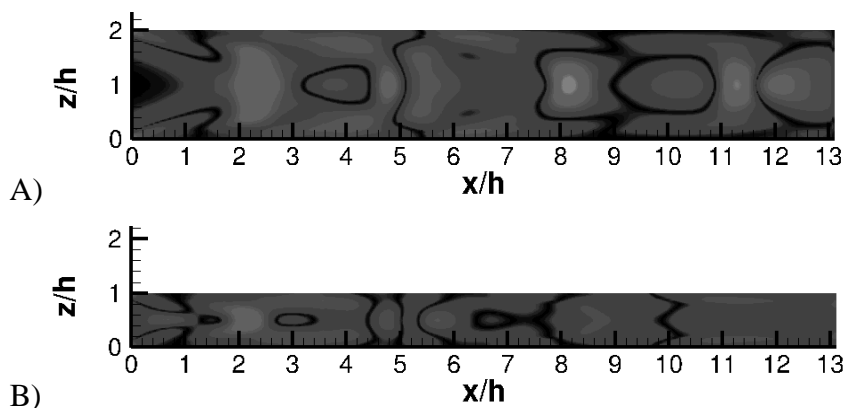


Fig. 5.28 Pseudo-Schlieren Image on Y-Centerline A) 3D Low AR, B) 3D High AR

The pressure in the channel shows the same trend of the shock train being significantly shortened and compressed upstream. Fig. 5.29 compares the normalized pressure in the Low AR and High AR channels, in both the z and y centerline planes. Here, we see that, not only has the shock train changed, but the variance in pressure induced by the shocks has been diminished as well. Both the low and high pressure regions of the channel are less pronounced, leading towards a more uniform flow. This leads to a lower pressure at the channel exit, which could be detrimental in regard to unstart because there will be less pressure in the streamwise direction to oppose a sudden backpressure.

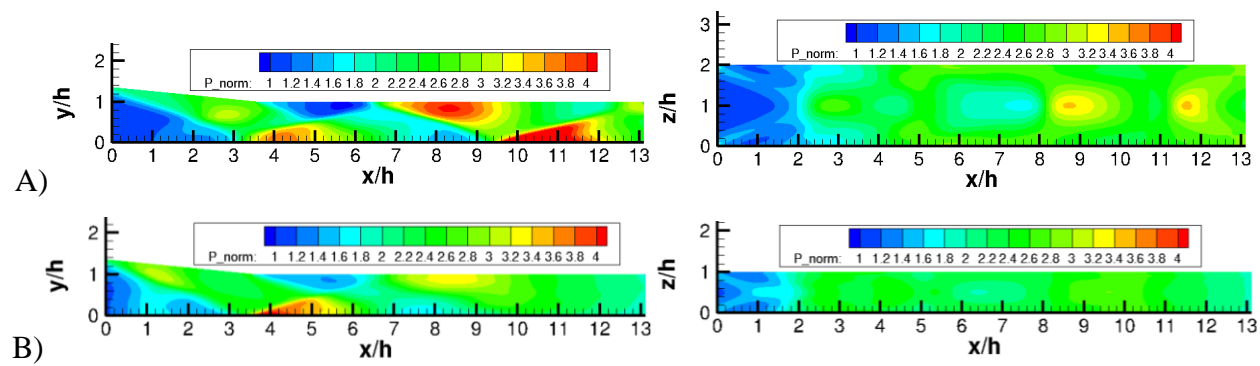


Fig. 5.29 3D Wall Pressure A) High AR, B) Low AR

The quantitative values for the wall pressures of the low and high aspect ratio channels are compared below in Fig. 5.30. As was seen in the previous plot, the low aspect ratio has much lower pressures throughout the channel and the reduced shock train length means that the pressure levels off, especially on the top wall, very quickly. Given that this inflow pressure distribution is what resists combustion instabilities that might propagate upstream, the significantly lower pressure seen is likely to make unstart occur at a lower force and happen faster than in the high aspect ratio case. Additionally, the upstream shift of the pressure peaks from the new shock train can be seen along the top and bottom walls of the channel.

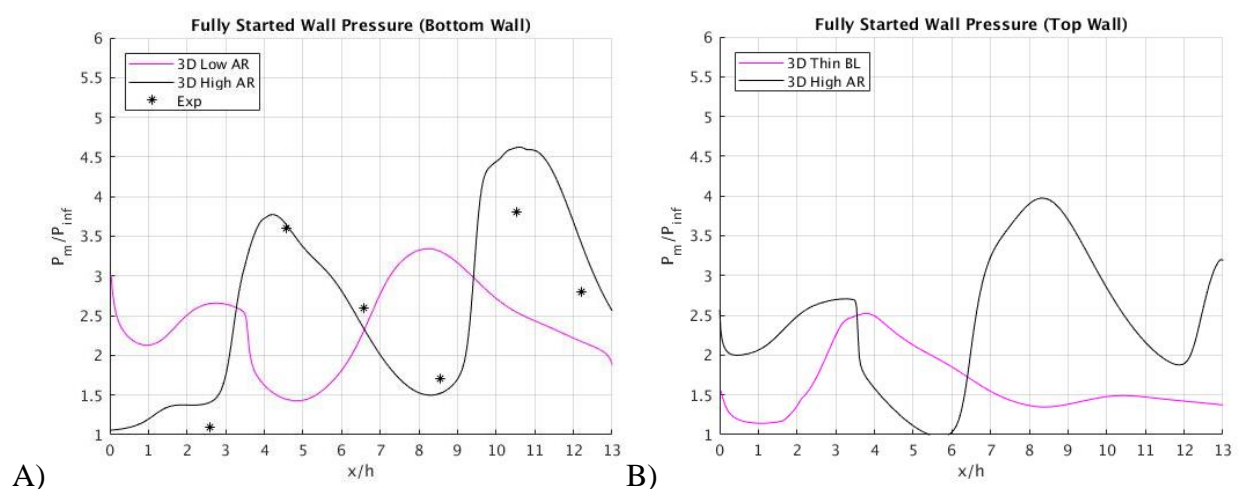


Fig. 5.30 3D Low AR Fully Started Flow Wall Pressure on Channel A) Floor, B) Ceiling

The computational flow velocity field images in Fig. 5.31 reinforce the findings above. The streamwise flow velocity is greatly diminished in the Low AR case when compared to the High AR case. Some of the high Mach structures in the flow field are gone entirely and the supersonic core flow has been reduced overall. Furthermore, the v velocity has been also reduced in strength. In addition, the size of the large negative and positive flow velocities in the vertical direction have shrunk.

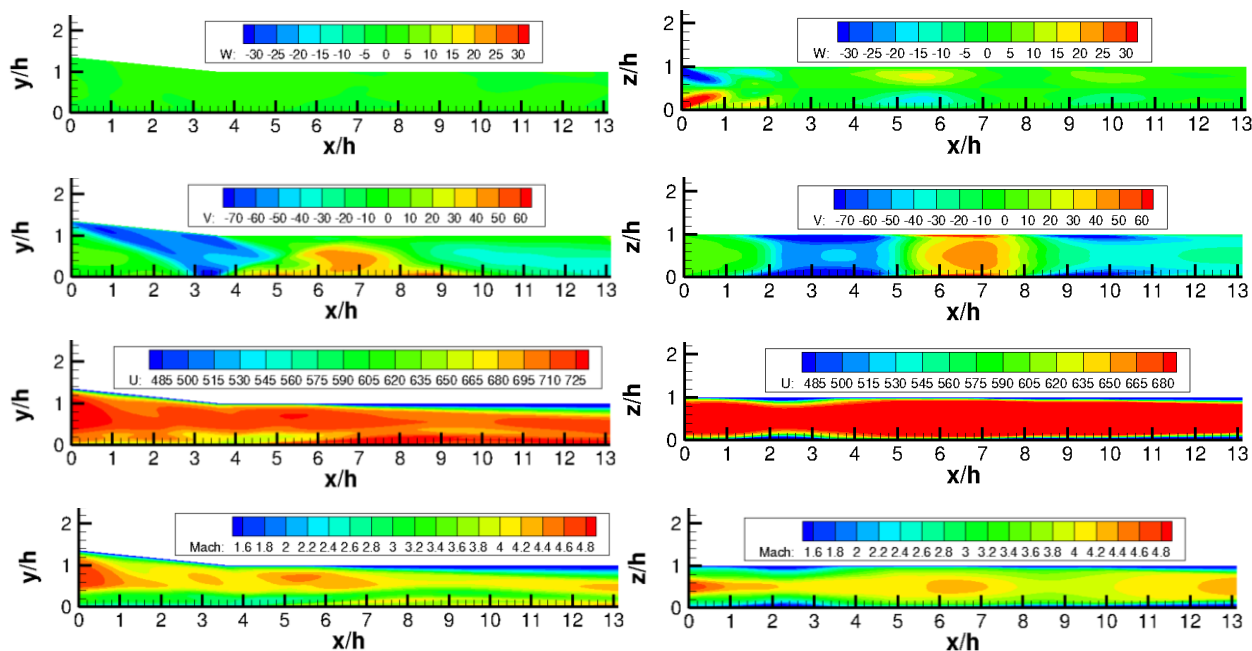


Fig. 5.31 3D Low AR Velocity Field for Z Centerline (L) and Y Centerline (R)

In this Low AR channel, the impact of the boundary layer flow entering the inlet has a much greater influence on reducing the flow energy and shrinking the core flow. It moves the flow state further from the High AR case and further reduces both the flow speed and the relative pressures present in the channel. Given the significant changes in the fully started flow state, unstart is likely to be quite different as well.

5.2.2 Narrow Channel Unstart

Unstart is quite different in the low aspect ratio channel. Fig. 5.32 shows the normalized pressure during unstart. As expected, unstart seen in the low aspect ratio channel features the same hallmarks of the unstart process described before, but with several significant differences. In the low aspect ratio channel, unstart sees lower pressures, but the pressure changes in the region downstream of unstart. In addition, because the oblique shock train is shortened to only two shocks in the low aspect ratio channel, the pressure pulses previously seen do not occur until later in the unstart process, playing a smaller role in the transient response of the system. The shape of unstart remains relatively constant throughout the process, both in the xy plane and in the xz plane.

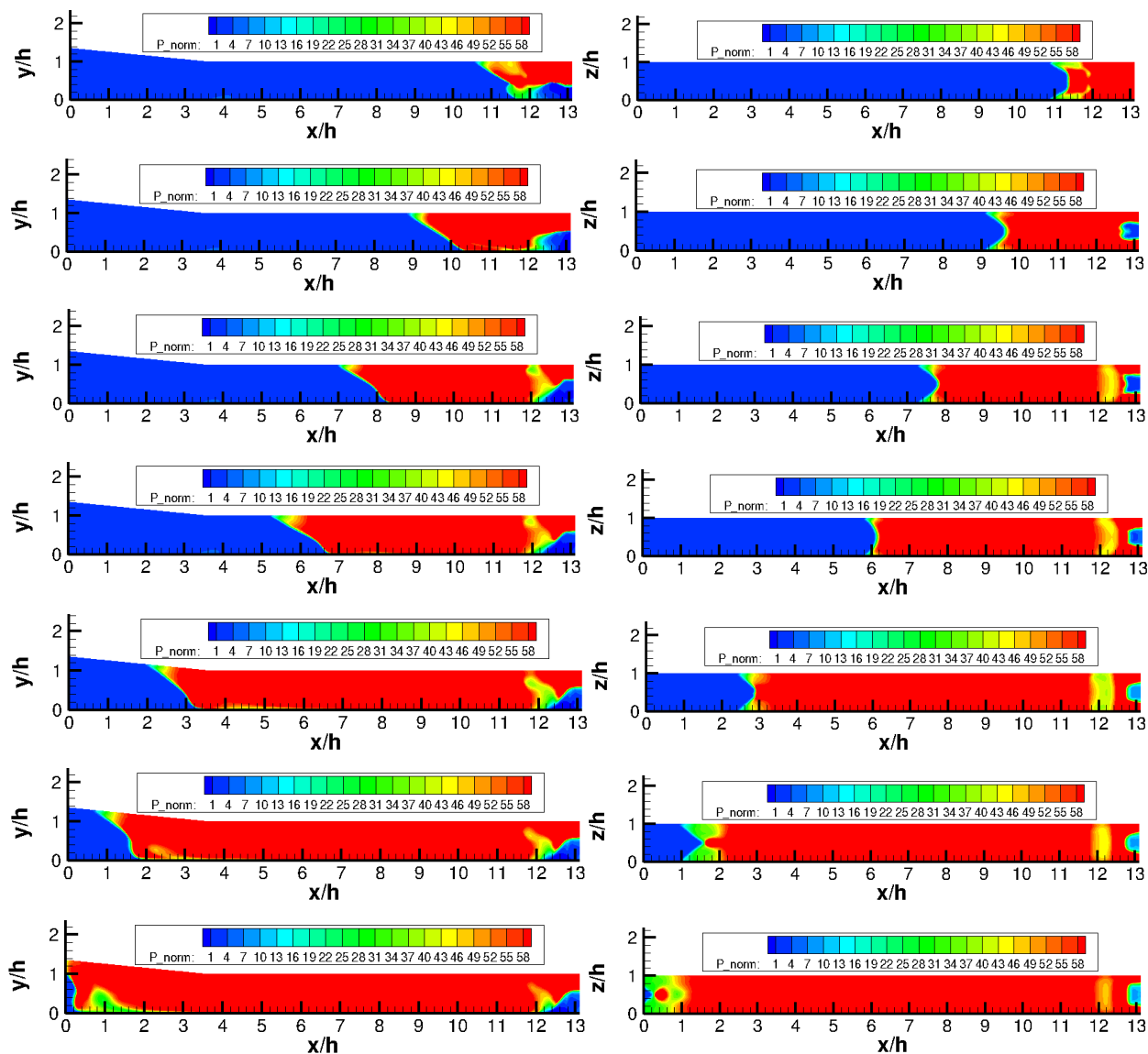


Fig. 5.32 3D Low AR Unstart Pressure at $t = [0.05, 0.10, 0.15, \dots, 0.4]$ ms

The speed of unstart also changes with the channel aspect ratio. Fig. 5.33, below, shows that unstart occurs faster in the low aspect ratio, or narrow, channel than in the baseline case. Likely due to less backpressure resistance existing upstream of unstart, the unstart shock can progress upstream less impeded than before. The mean unstart speed measures as 1.0948 along the top wall and 0.7879 along the bottom wall of the channel. Comparing to the High AR case, it becomes clear that an aspect ratio closer to one causes an amplification of the 3D effects and works to increase the speed of the unstart process.

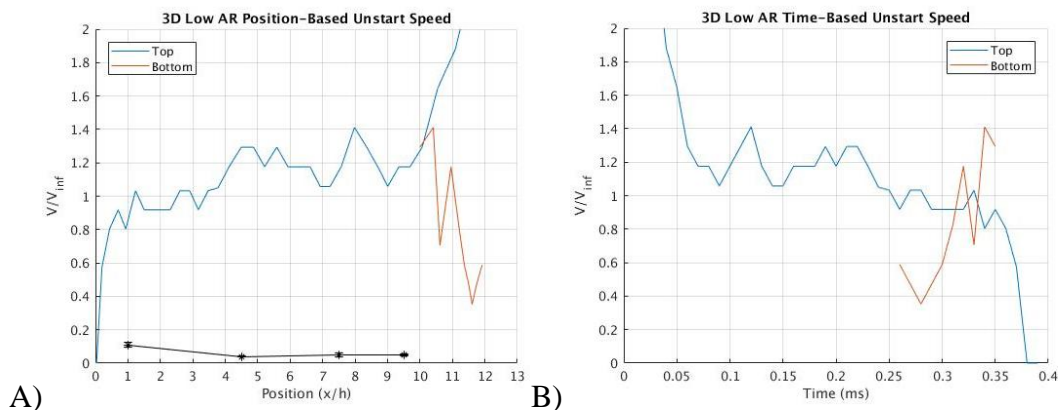


Fig. 5.33 3D Low AR Unstart Speed vs A) Position, B) Time

The unstart shock arrival time, in Fig. 5.34, shows a large departure from the other cases seen previously. First, unstart along the bottom wall is extremely delayed, with the thick boundary layer insulating the surface from the shock until very late in the process. Even then, the largest pressures are only seen in the region of the isolator exit. Unstart in this case, with an aspect ratio of one, appears as if there are two distinct sections of the channel. In fact, the thick boundary layer and lack of vertical mixing may result in the aspect ratio seen by unstart being skewed, such that the channel acts only half as high as it actually is. There is significantly less vertical mixing and dilution of the boundary layer during unstart than in the High AR case.

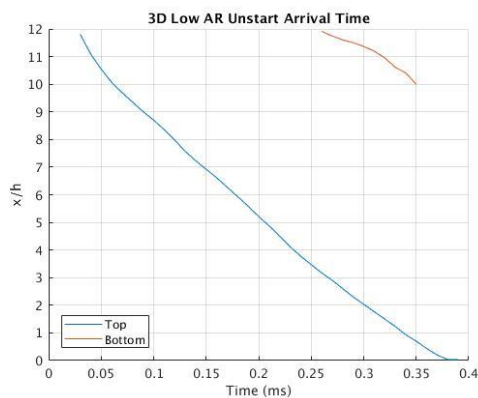


Fig. 5.34 3D Low AR Unstart Shock Arrival Time

The Mach number distribution within the inlet-isolator also sees changes as compared to the wider channel. Fig. 5.35 depicts how Mach number changes during unstart, specifically the speed of the flow in the subsonic region downstream of the unstart shock leading edge. This subsonic

region is much more homogeneous than what was previously observed. This is evidence of three-dimensional effects playing a much larger role in this channel, as mixing of the post unstart region is enhanced relative to the wider channel previously discussed. It is likely that this additional mixing, coupled with the reduction in oblique will significantly diminish, if not entirely erase, the precursor signals to unstart.

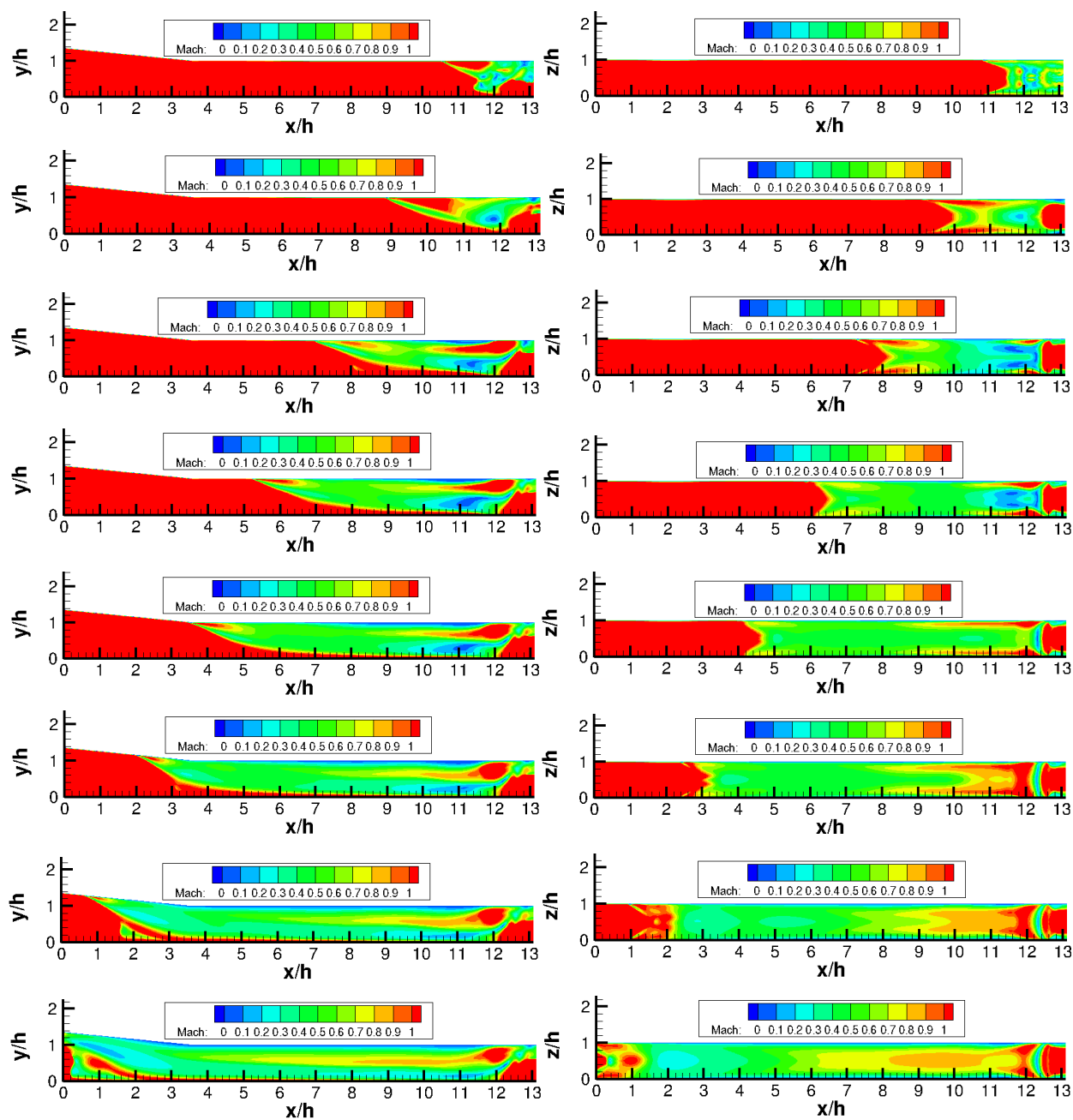


Fig. 5.35 3D Low AR Unstart Mach at $t = [0.05, 0.10, 0.15, \dots, 0.4]$ ms

5.2.3 Narrow Channel Unstart Precursors

Examining the unstart precursor signals is the final piece of this puzzle. Fig. 5.36 presents the pressure traces during unstart, along the top and bottom walls of the channel. Again, this is data taken from the channel centerline. The pressures seen are much lower than in both of the 3D cases, with and without the thick boundary layer. This suggests that the length of the oblique shock train is much more important for unstart pressure strength than boundary layer thickness.

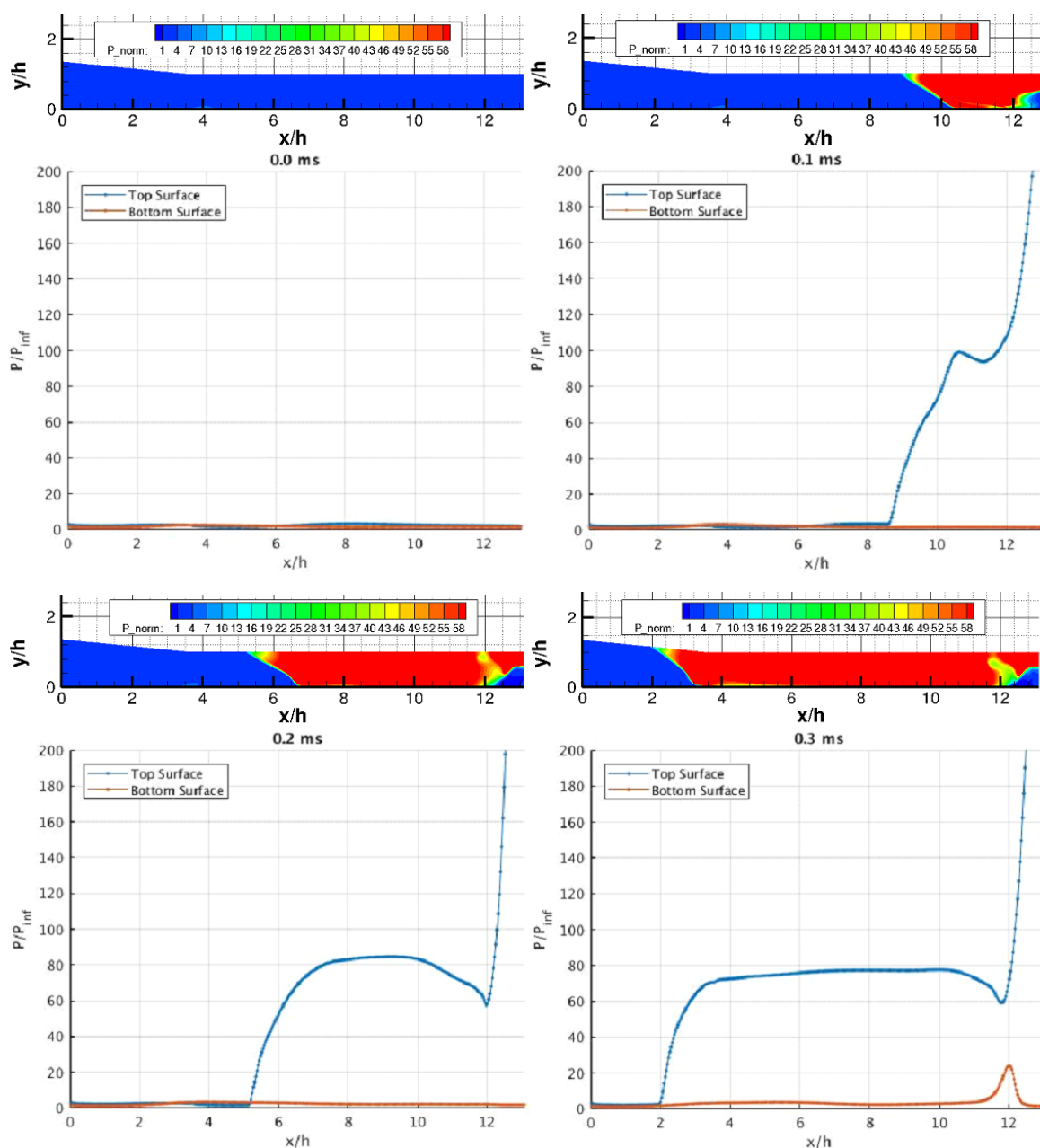


Fig. 5.36 3D Low AR Wall Pressure Traces during Unstart at $t = [0.0, 0.1, 0.2, 0.3]$ ms

The bottom surface of the channel takes significantly longer to see a pressure rise from unstart. This may be caused by a two-fold process. First, there is the thick bottom boundary layer that insulates the bottom surface from unstart. Second, the unstart shock is not running up against the oblique shock train for longer, so there are no expansion fans from crossed shock waves in most of the isolator portion of the geometry.

Plotting just the peak pressure in the channel furthers the points made above. Fig. 5.37 tracks the peak pressure along the top and bottom walls during unstart in the low aspect ratio channel. Here, the delay in unstart along the bottom wall can be seen quite clearly.

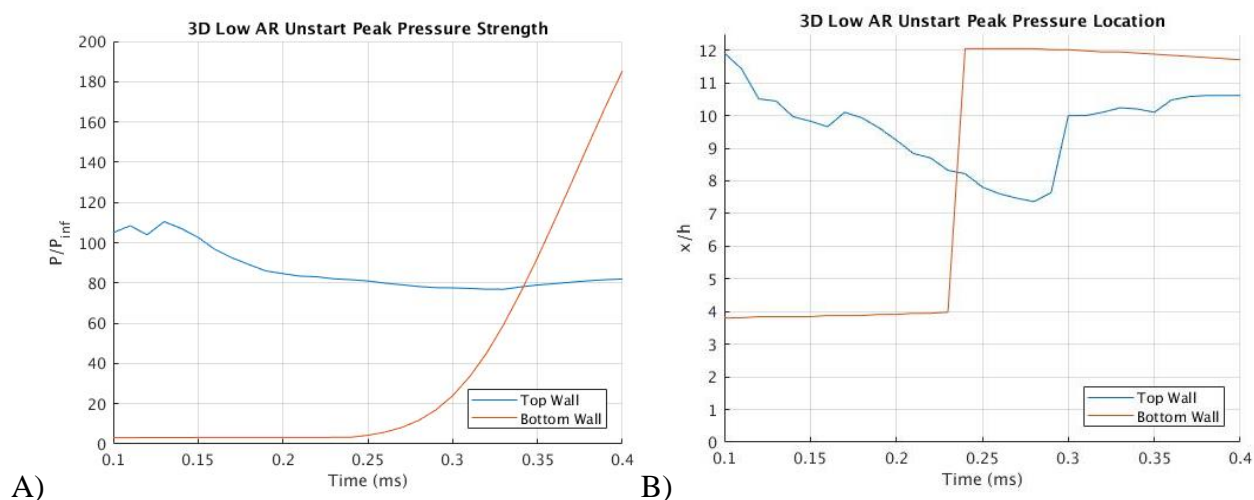


Fig. 5.37 3D Low AR Unstart Peak Pressure A) Strength, B) Location

Finally, we consider the precursor signals. Fig. 5.38 plots the difference from baseline in normalized pressure along the top and bottom surfaces of the channel at selected times during unstart. Fig. 5.39 does the same, but at all points in time. From these two figures, we can see that there are now only two major signal locations, rather than four, as the number of oblique shocks has been cut in half. The top surface sees a diminished precursor signal relative to the high aspect ratio as expected. The bottom surface, on the other hand, sees a large signal throughout the entirety of the boundary layer. Although it is strongest at the shock impingement point, it exists along the entire channel floor, is the largest departure from the other computations seen up to this point. The bottom wall can be seen to act quite different from the top wall when it comes to the precursor signal as well. There is a relatively uniform increase of pressure throughout the floor boundary layer as unstart progresses, but not the large spikes in pressure seen that indicate the unstart shock.

However, due to the delayed response of the floor wall pressure to the unstart leading edge shock, this strong and wide precursor signal may occur too late to be a useful means of detecting the presence of unstart.

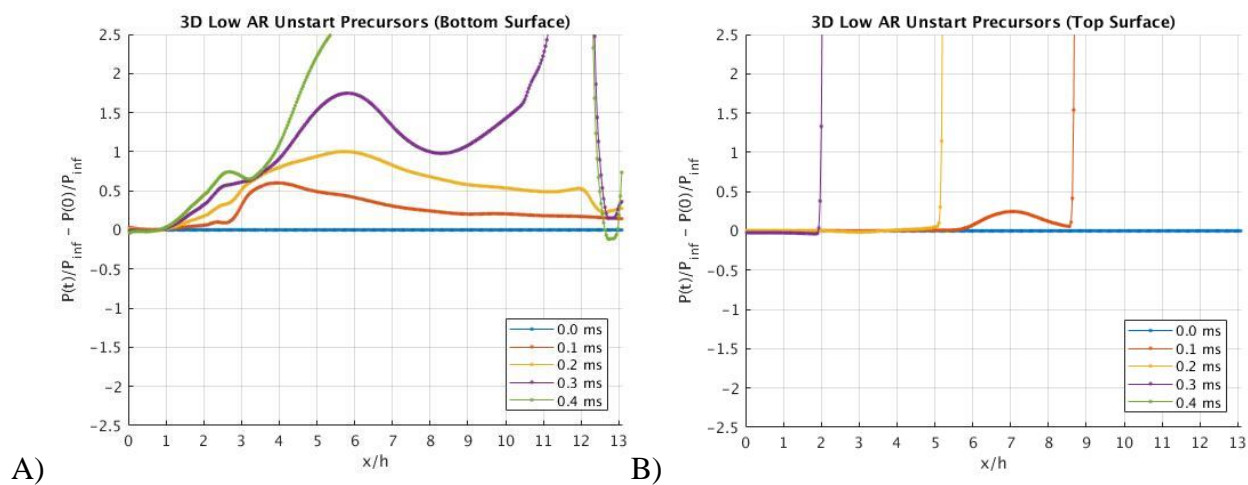


Fig. 5.38 3D Low AR Unstart Precursor Signal on Channel A) Bottom, B) Top

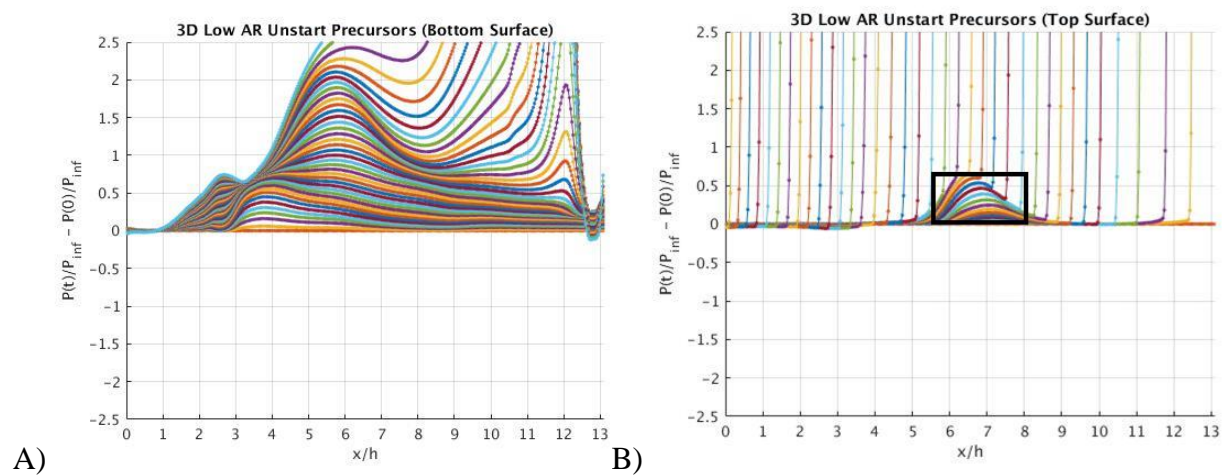


Fig. 5.39 3D Low AR Unstart Precursor Signal (all time) on Channel A) Bottom, B) Top

6. CONCLUSIONS

Over the course of this research, a variety of flow states were examined and compared to experimental data and other researcher's work, where possible. Several conclusions were made from the different models. This section will summarize the conclusions made in the different sections and suggest possible avenues of future work, both computational and experimental, to further the research put forth here.

6.1 Results Summary

In this thesis, RANS and URANS calculations were used to solve for a Mach 4.9 flow in a channel. The specific geometry used was an inlet-isolator model for a dual-mode scramjet, and the resultant data were compared to experiments conducted at the University of Texas, Austin. In both 2D and 3D, the code was validated against the available experimental data. The fully started steady state flow in both cases was shown to be an accurate recreation of the experimental data, with the 3D simulation producing results closer to the experimental data.

A source term was proven to be an effective, tunable, and repeatable method of initiating unstart in a computation, with lower computational complexity than a moving mesh. It was able to successfully mimic a physical flap both in its spatial distribution and in its forcing of the initial fully started flow. The source term was shown to be a robust forcing mechanism for unstart, with it working in both 2D and 3D, as well as with different boundary conditions and with different channel geometries.

The flow structures and wall pressures matched well with experimental data, particularly in the 3D case. The role of vortices were examine in the unstart response and were found to enhance the mixing in the post unstart region, downstream of its leading edge. In addition, they aided in the insulation of the floor boundary layer from the unstart response. The main difference seen between the computations and the experiments, was the speed at which unstart propagated upstream once initiated, which is a discrepancy seen previously in other computational studies. This effect was more pronounced in the 3D calculations. Also, the 3D solution showed that the leading edge of the unstart shock is actually along the channel sidewalls, rather than down the centerline. The distance between the leading edge of the shock on the centerline and on the sidewalls varied throughout the

unstart process, but the shock position on the sidewalls stayed consistently ahead of that in the channel center.

Precursor signals to unstart were identified and quantified in terms of strength and location. Significant variations in the pressure, relative to the fully started flow pressure, were found in the boundary layer, in discreet areas near the oblique shock impingement points along the top and bottom walls of the channel. These pressure variations preceded the arrival of the unstart shock leading edge, indicating a signal traveling upstream through the boundary layer. These signals can be used to identify the initiation of an unstart event before unstart propagation progresses too far upstream.

In addition to matching the experimental conditions, unstart was studied in an identical channel but lacking a thick incoming boundary layer. A boundary layer developing just from the sharp leading edge of the channel is a boundary condition more representative of flight of a dual-mode scramjet. It was important to examine how the boundary layer in the experiment affected the results and the potential repercussions of extrapolating those results to flight conditions. The presence of the thick boundary layer in the channel was found to shift the shock train upstream, slow unstart, and enhance the precursor signal, relative to the thin boundary layer case. The precursor signal was more robust in the thick boundary layer case, growing both stronger and occupying a wider section of the channel.

The aspect ratio of the channel was also examined to determine its effect on unstart. Many channels studied in the past for dual-mode scramjet inlet-isolator models use an aspect ratio of one, with the channel height and width being equal. In the experiment conducted at the University of Texas, Austin, the aspect ratio was two, with the channel being twice as wide as it was tall. This wider channel geometry was found to reduce unstart speed and increase the number of identifiable locations where a precursor signal is present. It also increased the length of the steady state, fully started flow, shock train.

Generalizing these conclusions, it appears that a large aspect ratio is beneficial in an inlet-isolator model as it reduces 3D effects, reducing the mixing caused by corner vortices in the channel. In addition, it allows for a longer shock train, which helps in reducing unstart speed. The results suggest that a relatively wider channel should have more easily detectable unstart precursor signals. A thicker boundary layer was found to slow unstart and allow a precursor signal to better propagate along the channel walls, ahead of unstart.

6.2 Suggestions for Future Work

There are a number of areas for future research that can further the findings of this research. On the computational side, matching the measurement speed of unstart propagation is a necessary future step. It may require an even larger mesh or direct numerical simulation to accomplish, but is important to both reinforce the findings here, and to develop a better of model moving forward. It could also require use of a different turbulence model, or a combination of models for increased accuracy.

In addition, given the ability to easily modify the location, dimensions, and strength of the source term, it should be able to simulate a wide range of disturbances and help predict the unstart response in a variety of conditions. A study examining different unstart initiation mechanisms and simulating them with the source term should be able provide a representation what sort of unstart conditions may occur in flight.

Finally, a future experimental study should look specifically for the precursor signals found here. Hopefully identifying the relative strength and predicted location of precursor signals will make them easier to detect. By placing quick response pressure transducers at the oblique shock impingement points, it should be possible to identify a precursor signal during unstart. The placement location of pressure probes along the channel floor in past experiments is a possible reason why these signals have not previously been identified in experiment. If an experiment confirmed the precursor signals' existence in unstart, it could be a huge step for unstart detection and disruption.

REFERENCES

- [1] T. A. Barber, B. A. Maicke and J. Majdalani, "Current State of High Speed Propulsion: Gaps, Obstacles and Technological Challenges in Hypersonic Applications," in *45th AIAA/ASME/SAE/ASEE Joint Propulsion Conference and Exhibit, Joint Propulsion Conferences*, Denver, CO, 2009, AIAA Paper 2009-5118.
- [2] R. S. Fry, "A Century of Ramjet Propulsion Technology Evolution," *Journal of Propulsion and Power*, vol. 20, no. 1, pp. 27-58, 2004.
- [3] P. J. Waltrup, M. E. White, F. Zarlingo and E. S. Gravlin, "History of U.S. Navy Ramjet, Scramjet, and Mixed-Cycle Propulsion Development," *Journal of Propulsion and Power*, vol. 18, no. 1, pp. 14-27, 2002.
- [4] J. D. Anderson, *Hypersonic and High Temperature Gas Dynamics Second Edition*, Reston, VA: American Institute of Aeronautics and Astronautics, Inc., 2006, pp. 456-458.
- [5] G. Y. Anderson, C. R. McClinton and J. P. Weidner, "Scramjet Performance," in *Scramjet Propulsion*, Reston, VA, AIAA Progress in Aeronautics and Astronautics, vol. 189, 2000.
- [6] E. T. Curran and F. D. Stull, "The Utilization of Supersonic Combustion Ramjet Systems at Low Mach Numbers," Technical Report RTD-TDR-63-4097, AF Aero Propulsion Laboratory, Wright-Patterson Air Force Base, Ohio, 1964.
- [7] D. Andreadis, "Scramjet Engines Enabling the Seamless Integration of Air & Space Operations," Pratt & Whitney Space Propulsion, Hypersonics, West Palm Beach, FL, 2004.
- [8] P. J. Waltrup, "Combustor/Inlet Interactions and Modeling of Hypersonic Dual Combustion Ramjet Engines," Technical Report AFOSR-TR-89-1601, Johns Hopkins University / APL, Laurel, MD, 1983.
- [9] J. C. Adams, W. R. Martindale and M. O. Varner, "One-Dimensional Unsteady Modeling of Supersonic Inlet Unstart/Restart," in *22nd Aerospace Sciences Meeting, Aerospace Sciences Meetings, Aerospace Sciences Meetings*, Reno, NV, 1984, AIAA Paper 84-0439.

- [10] M. Brocanelli, Y. Gunbatar, A. Serrani and M. A. Bolender, "Robust Control for Unstart Recovery in Hypersonic Vehicles," in *AIAA Guidance, Navigation, and Control Conference, Guidance, Navigation, and Control and Co-located Conferences*, Minneapolis, MN, 2012, AIAA Paper 2012-4698.
- [11] H. Do, A. Passaro and D. Baccarella, "Inlet Unstart of an Ethylene-Fueled Model Scramjet with a Mach 4.5 Freestream Flow," in *18th AIAA/3AF International Space Planes and Hypersonic Systems and Technologies Conference, International Space Planes and Hypersonic Systems and Technologies Conferences*, Tours, France, 2012, AIAA Paper 2012-5929.
- [12] J. L. Wagner, A. Valdivia, K. B. Yuceil, N. T. Clemens and D. S. Dolling, "An Experimental Investigation of Supersonic Inlet Unstart," in *37th AIAA Fluid Dynamics Conference and Exhibit, Fluid Dynamics and Co-located Conferences*, Miami, FL, 2007, AIAA Paper 2007-4352.
- [13] D. W. Mayer and G. C. Paynter, "Prediction of Supersonic Inlet Unstart Caused by Freestream Disturbances," *AIAA Journal*, vol. 33, no. 2, pp. 266-275, 1995.
- [14] J. A. Fike, K. Duraisamy, J. J. Alonso, H. Do, S. Im and M. A. Cappelli, "Experimental and Computational Investigation of Mass Injection Induced Unstart," in *29th AIAA Applied Aerodynamics Conference, Fluid Dynamics and Co-located Conferences*, Honolulu, HI, 2011, AIAA Paper 2011-3192.
- [15] Z. Rosenberg, "Second X-51 Hypersonic Flight Ends Prematurely," *Flight International*, 25 October 2012.
- [16] B. Qin, J. Chang, X. Jiao and W. Bao, "Unstart Margin Characterization Method of Scramjet Considering Isolator-Combustor Interactions," *AIAA Journal*, vol. 53, no. 2, pp. 493-500, 2015.
- [17] A. Valdivia, K. B. Yuceil, J. L. Wagner, N. T. Clemens and D. S. Dolling, "Control of Supersonic Inlet-Isolator Unstart Using Active and Passive Vortex Generators," *AIAA Journal*, vol. 52, no. 6, pp. 1207-1218, 2014.
- [18] J. L. Wagner, "Experimental Studies of Unstart Dynamics in Inlet/Isolator Configurations in a Mach 5 Flow," PhD Thesis, Department of Aerospace Engineering and Engineering Mechanics, University of Texas, Austin, TX, 2009.

- [19] J. L. Wagner, A. Valdivia, K. B. Yuceil, N. T. Clemens and D. S. Dolling, "Experimental Investigation of Unstart in an Inlet/Isolator Model in Mach 5 Flow," *AIAA Journal*, vol. 47, no. 6, pp. 1528-1542, 2009.
- [20] J. L. Wagner, A. Valdivia, K. B. Yuceil, N. T. Clemens and D. S. Dolling, "Velocimetry Measurements of Unstart in an Inlet-Isolator Model in Mach 5 Flow," *AIAA Journal*, vol. 48, no. 9, pp. 1875-1888, 2010.
- [21] I. Jang, R. Pecnik and P. Moin, "A Numerical Study of the Unstart Event in an Inlet/Isolator Model," Center for Turbulence Research Annual Research Briefs, Stanford, CA, 2010.
- [22] *SU2, Software Package*, Palo Alto, CA: Stanford University, 2019.
- [23] T. D. Economon, F. Palacios, S. R. Copeland, T. W. Lukaczyk and J. J. Alonso, "SU2: An Open-Source Suite for Multiphysics Simulation and Design," *AIAA Journal*, vol. 54, no. 3, pp. 828-846, 2016.
- [24] P. R. Spalart and S. R. Allmaras, "A One-Equation Turbulence Model for Aerodynamic Flows," in *30th Aerospace Sciences Meeting and Exhibit, Aerospace Sciences Meetings*, Reno, NV, 1992, AIAA Paper 92-0439.
- [25] Y. Saad, "A Flexible Inner-Outer Preconditioned GMRES Algorithm," *SIAM Journal on Scientific Computing*, vol. 14, no. 2, p. 461-469, 1993.
- [26] S. Yoon and D. Kwak, "Artificial Dissipation Models for Hypersonic External Flow," in *24th Joint Propulsion Conference, Joint Propulsion Conferences*, Boston, MA, 1988, AIAA Paper 88-3277.
- [27] S. Yoon and A. Jameson, "A High Resolution Shock Capturing Scheme for High Mach Number Internal Flow," Technical Report NASA CR-179523, 1986.
- [28] *Tecplot 360 EX, Software Package, Ver. R*, Bellevue, WA: Tecplot, Inc., 2018.
- [29] "Overview of Halstead," Purdue University Information Technology Research Computing, 2017. [Online]. Available: <https://www.rcac.purdue.edu/compute/halstead>.
- [30] "Overview of Brown," Purdue University Information Technology Research Computing, 2017. [Online]. Available: <https://www.rcac.purdue.edu/compute/brown>.

- [31] A. H. Karp and H. P. Flatt, "Measuring Parallel Processor Performance," *Communications of the ACM*, vol. 33, no. 5, pp. 539-543, 1990.
- [32] M. Atkinson, J. Poggie and J. Camberos, "Control of High-Angle-of-Attack Reentry Flow with Plasma Actuators," *Journal of Spacecraft and Rockets*, vol. 50, no. 2, pp. 337-346, 2013.
- [33] J. Poggie, "Plasma-Based Control of Shock-Wave / Boundary-Layer Interaction," in *44th AIAA Aerospace Sciences Meeting and Exhibit, Aerospace Sciences Meetings*, Reno, NV, 2006, AIAA Paper 2006-1007.
- [34] J. Poggie, "Plasma-Based Hypersonic Flow Control," in *37th AIAA Plasmadynamics and Lasers Conference, Fluid Dynamics and Co-located Conferences*, San Francisco, CA, 2006, AIAA Paper 2006-3567.
- [35] T. Von Karman, "Turbulence and Skin Friction," *Journal of the Aeronautical Sciences*, vol. 1, no. 1, pp. 1-20, 1934.
- [36] E. R. Van Driest, "Turbulent Boundary Layer in Compressible Fluids," *Journal of the Aeronautical Sciences*, vol. 18, no. 3, pp. 145-160, 1951.
- [37] P. J. Roache, "Perspective: A Method for Uniform Reporting of Grid Refinement Studies," *Journal of Fluids Engineering*, vol. 116, no. 3, pp. 405-413, 1994.
- [38] P. J. Roache, "Quantification of Uncertainty in Computational Fluid Dynamics," *Annual Review of Fluid Mechanics*, vol. 29, pp. 123-160, 1997.
- [39] J. M. Donbar, G. J. Linn, S. Srikant and M. R. Akella, "High-Frequency Pressure Measurements for Unstart Detection in Scramjet Isolators," in *46th AIAA/ASME/SAE/ASEE Joint Propulsion Conference & Exhibit, Joint Propulsion Conferences*, Nashville, TN, 2010, AIAA Paper 2010-6557.
- [40] P. A. Varadarajan and P. L. Roe, "Geometrical Shock Dynamics and Engine Unstart," in *41st AIAA Fluid Dynamics Conference and Exhibit, Fluid Dynamics and Co-located Conferences*, Honolulu, HI, 2011, AIAA Paper 2011-3909.
- [41] F. Marconi, "Internal Corner Flow Fields," in *17th Aerospace Sciences Meeting, Aerospace Sciences Meetings*, New Orleans, LA, 1979, AIAA Paper 79-0014.

- [42] T. Sato and S. Kaji, "Study on Steady and Unsteady Unstart Phenomena due to Compound Choking and/or Fluctuations in Combustor of Scramjet Engines," in *4th Symposium on Multidisciplinary Analysis and Optimization, Multidisciplinary Analysis Optimization Conferences*, Orlando, FL, 1992, AIAA Paper 92-5102.
- [43] H. Huang, H. Tan and Y. Ling, "Evolution of Supersonic Corner Vortex in a Hypersonic Inlet/Isolator Model," *Physics of Fluids*, vol. 28, no. 12, 2016.
- [44] X. Xiang and H. Babinsky, "Corner Effects for Oblique Shock Wave/Turbulent Boundary Layer Interactions in Rectangular Channels," *Journal of Fluid Mechanics*, vol. 862, p. 1060–1083, 2019.
- [45] H. Do, S. Im, M. G. Mungal and M. A. Cappelli, "Unstart of a Supersonic Model Inlet/Isolator Flow Induced by Mass Injection," in *49th AIAA Aerospace Sciences Meeting including the New Horizons Forum and Aerospace Exposition, Aerospace Sciences Meetings*, Orlando, FL, 2011, AIAA Paper 2011-68.
- [46] H. Do, S. Im, M. G. Mungal and M. A. Cappelli, "The Influence of Boundary Layers on Supersonic Inlet Unstart," in *17th AIAA International Space Planes and Hypersonic Systems and Technologies Conference, International Space Planes and Hypersonic Systems and Technologies Conferences*, San Francisco, CA, 2011, AIAA Paper 2011-2349.
- [47] R. Fiévet, H. Koo, V. Raman and A. H. Auslender, "Numerical Investigation of Shock-Train Response to Inflow Boundary-Layer Variations," *AIAA Journal*, vol. 55, no. 9, pp. 2888-2901, 2017.
- [48] T. Sridhar, G. Chandrabose and S. Thanigaiarasu, "Numerical Investigation of Geometrical Influence On Isolator Performance," *International Journal on Theoretical and Applied Research in Mechanical Engineering (IJTARME)*, vol. 2, no. 3, 2013.
- [49] A. R. Wieting, "Exploratory Study of Transient Unstart Phenomena in a Three-Dimensional Fixed-Geometry Scramjet Engine," Technical Report NASA TN D-8156, NASA Langley Research Center, Hampton, VA, 1976.